Incorporating self-assembly into robocasting for applications in hard tissue engineering

EMMANOUIL PAPASTAVROU

A thesis submitted in partial fulfilment of the requirements of
Nottingham Trent University for the degree of

DOCTOR OF PHILOSOPHY

School of Architecture, Design and the Built Environment

NOTTINGHAM
TRENT UNIVERSITY

September 2016

Abstract

ABSTRACT

High cost coupled with limited supply of hard tissue substitutes make necessary the development of synthetic biomaterials, as well as economical and reproducible manufacturing techniques that can be easily scaled up. Multiple and often conflicting requirements have so far impeded the application of polymer/ceramic composites in large load-bearing defects. Although porosity is a crucial biological requirement, it has a detrimental effect on their mechanical performance. This thesis emphasizes upon methods for structuring bioceramic materials at different orders of magnitude - termed structural hierarchy. In bones, this constitutes the main mechanism contributing to their remarkable strength and fracture resistance. This can be achieved through combining AM with physical processes that cause the material to self-assemble into various configurations during or following its deposition.

The first part of this research explores the potential of Low-Temperature Deposition Modelling (LDM) in fabricating scaffolds with tailorable bimodal porosity. More specifically, LDM is treated as a hybrid technique, in which robocasting is combined with freezing-induced self-assembly. For the purposes of this study, a highly versatile and economical print-head was fabricated that can be operated at ambient temperatures down to -20°C. In addition, a highly thixotropic β-TCP paste formulation of high water content (80% v/v) was developed that takes advantage of a synergy existing between Sodium Alginate and Xanthan Gum. The findings suggest that chamber temperature and water content have the most marked effect on pore morphology. Ordered micro-architectures comprising lamellar pores with a high degree of alignment were obtained at low freezing rates (-5°C). Most importantly, this research evidences for the first time that their direction is not only dictated by toolpath geometry, but also by the ice structure in preceding layers (epitaxy).

The second part of this thesis demonstrates the combination of robocasting with a heating process to produce planar hollow-tube lattices that can be manipulated into various configurations. This technique makes use of a novel Sodium Alginate-based β-TCP slurry reinforced with cellulose nano-fibrils. When heated rapidly, it forms hollow-shell structures, which can be cross-linked in Ca^{2+}-rich solutions to produce flexible yet strong particle-reinforced gels. Optimal results were achieved at 3 and 4% w/w alginate content, where the paste's loss tangent reaches its maximum value.

This research demonstrates that such combinational approaches to AM can successfully produce hard tissue substitutes that exhibit multiple levels of structural hierarchy. This constitutes a first step towards achieving biomimetic bone scaffolds with superior mechanical performance.

Dedicated to my beloved sister Aggeliki,

Σε ποιαν έκσταση απάνω, σε χορό μαγικό
μπορεί ένα τέτοιο πλάσμα να γεννήθηκε
Από ποιο μακρινό αστέρι είναι το φως
που μες στα δυο της μάτια πήγε κρύφτηκε
κι εγώ ο τυχερός που το 'χει δει...

ACKNOWLEDGEMENTS

TABLE OF CONTENTS

LIST OF FIGURES

LIST OF TABLES

Chapter 1
Synthetic bone substitutes:
current state of the art

1.1. Introduction

An ageing population and the increasing popularity of extreme sports have contributed to a dramatic increase in bone grafting operations: In 2010 approximately 2 million patients underwent a bone grafting procedure to repair bone defects; by 2012, that number had risen to 2.2 million patients (Kolk et al., 2012). The causes vary from bone cysts and tumours, revisions of orthopaedic implants and spinal fusion to complicated fractures and delayed unions, mal-unions or even non-unions (Bohner et al., 2012). In 2010, an annual turnover of roughly 1 billion US$ was generated by hard tissue substitutes, with a yearly market growth of 10%. The majority of substitutes are harvested from the patient (autografts) or donors (allografts, Fig. 1.1), or can even be derived from animals (xenografts). Autografts pose size limitations and they entail a risk of donor site morbidity, while the major disadvantage of allografts is the risk of transmission of infectious diseases (Nandi et al., 2010). The average cost of 1 g of bone graft is in the region of 100 US$, with synthetic bone grafts representing only 15% of the total market. A high cost coupled with a limited supply of hard tissue substitutes make necessary the

development of synthetic biomaterials, as well as economical and reproducible manufacturing techniques that can be easily scaled up. (Bohner, 2010a).

Fig. 1.1. Spinal implant milled from a cortical allograft (Source: X-spine Systems Inc.).

The field of hard tissue engineering has been active for more than 40 years and in this time it has gone through three distinct phases: starting from biocompatible ceramics that were just tolerated in a physiological environment (*substitution*), the research soon moved onto the development of bioresorbable materials (*repair*). The current trend is related to regenerative medicine and focuses on materials that induce bone formation and vascularisation (*regeneration*) (Dorozhkin, 2013; Scholz et al., 2011). The research focuses on three main subject areas, namely *cells*, *signals* (biochemical factors) and *scaffolds.* Its nature has therefore become fairly interdisciplinary, as it requires the synergy of engineering and life sciences to achieve an optimal biological interaction between a synthetic graft and the host tissue (Vallet-Regí et al., 2011). This research project draws knowledge from several disciplines, such as polymer science, chemistry, biology and engineering to extend the scope of a particular fabrication technique to the field of tissue engineering.

1.2. Research Context

A scaffold in tissue engineering is a biodegradable implant that mimics the extracellular matrix (ECM) of native tissues. An ECM is a highly complex, multifunctional and dynamic solid matrix where cells reside. It provides structural support, cues for cells to trigger specific responses and growth factors to stimulate cellular growth and proliferation (Chan and Leong, 2008). In bone tissue engineering specifically, two main methods have been employed for the generation of new tissue:

- The first method involves the initiation of the regeneration process in vitro. The scaffold is impregnated with cells and placed inside a bioreactor that provides all the necessary tissue-inducing substances, nutrients and mechanical stimuli for its maturation. Subsequently, it is implanted in the patient (Yeatts and Fisher, 2011).

- Alternatively, the in vitro maturation step can be omitted by grafting the peptides, hormones and growth factors into an acellular scaffold to be directly implanted in the patient (Vallet-Regí et al., 2011).

1.2.1. Requirements for synthetic bone substitutes

Despite the hundreds of publications and extensive research over the last 40 years, the realisation of synthetic hard tissue substitutes for clinical use remains a distant goal. The difficulty lies in the fulfilment of several requirements that sometimes are

even conflicting. Listed below are the most essential requirements for resorbable bone graft substitutes.

1.2.1.a. Bioresorption

(Bio)resorption is a term used interchangeably with words such as "(bio)degradation" or "(bio)absorption" and describes the progressive disappearance of a material from an implantation site in the course of time. It has been proposed that the ideal resorption rate be similar to the rate of new tissue formation. Therefore, the type of dissolution should preferably be cell mediated, i.e. achieved by osteoclasts. These cells, together with osteoblasts, are involved in the continuous remodelling of bone tissue. A combination of chemical and physical approaches can be used to control resorption rates. The most significant physical factor is the architecture of the material, particularly its porosity and mean grain size (Bohner, 2010a; Bohner et al., 2012).

1.2.1.b. Mechanical properties

There is large controversy over the appropriate *mechanical properties* of a bone scaffold. The mainstream view is that scaffolds should exhibit mechanical properties comparable to native trabecular (spongy) tissue. In this case, grafts must be designed to sustain loads applied to the site of implantation during daily activity. However, none of the materials that meet the biological requirements so far match the tensile, shear and fatigue properties of natural bone tissue. Any improvements made to their mechanical behaviour are often at the expense of their biological

performance (Bohner et al., 2012; Calori et al., 2011). To many researchers in the area, their weakness is of minor importance owing to the use of internal or external metal fixations, a very common practice in grafting procedures. Fixations, like the ones shown in Fig. 1.2, in the form of stainless steel or titanium plates screwed into the host bone on either side of the fracture can provide the necessary mechanical stability for healing (Bohner, 2010a).

Fig. 1.2. External forearm fixator (left) and internal midfoot fixators (right)
(Source: Acumed, Colson Associates Inc.).

An alternative and radical approach could be the mimesis of the natural process of healing, as described by B. Willie et al. in a paper published in 2010 with the title: "Why aim for a copy of mature tissue properties if nature uses a different approach?" The strongest argument against the use of stiff synthetic grafts is the absence of mechanical stimuli that they entail. Cells respond to mechanical signals by remodelling their ECM (whether native or synthetic), gradually maturing into a structure that is fully adapted to its mechanical environment. Moreover, a rigid scaffold does not experience any significant strain levels or local pressure changes,

resulting in poor fluid transport that can impact seriously the healing process of the defect. Finally, there are several other factors that determine the mechanical property requirements for a synthetic graft, such as the age, gender and habits of the patient (Willie et al., 2010).

1.2.1.c. Porosity

Porosity is crucial for tissue ingrowth and vascularisation to take place. A highly interconnected pore network allows for efficient nutrient delivery and cell migration. Ideally, a scaffold should exhibit hierarchical porosity of 60-65 %, with approximately 60% of its pores ranging from 150 to 400 µm and at least 20% smaller than 20 µm (Dorozhkin, 2013; Nandi et al., 2010). Microporosity is desirable because it offers a larger specific surface area, accelerating ion exchange and biological apatite deposition and increasing the number of adsorption sites for bone inducing proteins (Mastrogiacomo et al., 2006). It has also been demonstrated that the presence of interconnected micropores (0.5 to 10 µm diameter) promotes osseointegration at different scales, as it assists osteogenic cells in populating the internal surfaces of a scaffold (Lan Levengood et al., 2010). Pore size can also have an effect on the osteogenic path, favouring direct osteogenesis in large pores and osteochondral ossification in small pores (Hannink and Arts, 2011).

Fig. 1.3. Schematic representation of basic configurations of graded
porous biomaterials, proposed by (Miao and Sun, 2009).

Porosity gradients could also be incorporated in order to replicate bone segments that contain both cortical and trabecular regions (see Fig. 1.3). Moreover, dense sections featuring micro-pores on their surface could promote cartilage ingrowth for applications in joint reconstruction (Miao and Sun, 2009). Although this approach is still in its infancy, additive manufacturing techniques could assist in the fabrication of such complex constructs. However, although extensive porosity is beneficial to the biological performance of the scaffold, it can have a detrimental effect on its mechanical properties. This is due to the presence of voids, but also due to the increased resorption (biodegradation) rates that it entails. When the characteristic dimension of a scaffold is at the nano-scale, pore diameter and connectivity do not appear to be as influential, since cells can use alternative mechanisms of migration (Brown et al., 2009).

1.2.1.d. Osteoconductivity and Osteoinductivity

Osteoconductivity is dependent on the surface chemistry, ionic charge, degree of hydrophilicity and roughness, as well as topography at different scales (Flemming et al., 1999). It refers to the ability of a bioactive material to guide the formation

of bone tissue along its surface. A *bioactive* material is one that can form a strong bond with the host tissue and induce cell differentiation and proliferation. *Osteoinductive* materials are particularly favoured, due to their inherent ability to promote bone formation in ectopic sites (Brown et al., 2009; Hannink and Arts, 2011; Kolk et al., 2012). Osteoinductive and osteogenic properties are provided by bioactive molecules such as peptides, hormones and growth factors, which can be incorporated into a synthetic graft during its fabrication and released locally at controlled rates after its implantation (Janicki and Schmidmaier, 2011; Willie et al., 2010). Again, the architecture of a bone substitute plays an important role in entrapping circulating cells and growth factors (Hannink and Arts, 2011).

1.2.1.e. Sterilisation

Synthetic bone substitutes should be *sterilised* using standard procedures that do not alter its topography or material properties (Bartolo et al., 2012).

1.2.1.f. Customisation

The latest advancements in digital imaging and fabrication technologies, have opened the way to the production of *custom made* scaffolds to fill defects (Lichte et al., 2011).

However, there is large variation in the mechanical and architectural properties of bone tissue not only between individuals, but also between different anatomical sites or even between regions within the same bone organ (Fu et al., 2011a). The

design complexity of a scaffold appears to be enormous due to the multiple functions that it has to possess. Additionally, the architecture and mechanical properties of a scaffold change as it biodegrades and the by-products affect the biological response. This has led recently Bohner et al. (2011) to the conclusion that an ideal scaffold architecture does not exist.

Fig.1.4. Ashby plot of Fracture toughness against Young's modulus for
a range of biomaterials (Butscher et al., 2011)

1.2.2. Materials

A vast range of materials spanning across all classes have been tested for their biological and mechanical performance as potential biodegradable hard tissue substitutes. The graph in Fig. 1.4 illustrates the contrast between the mechanical behaviour of current man-made biocompatible materials and natural materials. Ceramics at the top left suffer from low fracture toughness, while polymers exhibit low stiffness. Very high resistance to deformation, as in the case of metals, is

undesirable for orthopaedic applications. Natural materials stand somewhere in the middle of this graph, as they are composite materials.

Metals	Non-biodegradable			steel
				tantalum
				titanium
				alloys of the above
	Biodegradable			Magnesium
Ceramics	Non-biodegradable			Alumina
				Zirconia
				Zirconia-Toughened Alumina
	Biodegradable	Bioglass		45S5
				S53P4
		Calcium Phosphate Ceramics		hydroxylapatite (HA)
				beta-tricalcium phosphate (β-TCP)
				alpha-tricalcium phosphate (α-TCP)
				biphasic tricalcium phosphate (BCP)
		Cements (Setting)		apatite
				brushite
				calcium sulphate dehydrate
				calcium sulphate hemihydrate
		Putties (Non-setting)		any of the above + hydrogels
Polymers	Non-biodegradable			Polyetherketone (PEEK)
				Polymethylmethacrylate (PMMA)
				Polyurethanes (PU)
				High Density Polyethylene (HDPE)
				Polyethelene Terephthalate (PET)
				Polytetrafluoroethylene (PTFE)
	Biodegradable	Synthetic		Polylactide (PLA)
				Polyethylene Glycol (PEG)
				Poly(lactic-co-glycolic acid) (PLGA)
				Polyglycolide (PGA)
				Polycaprolactone (PCL)
				Polyurethanes (PU)
				Poly(propylene fumarate)
				Polyphosphazenes
				Poly(1,4-butylene succinate)
		Natural	Proteins	Collagen
				Silk fibroin
			Polysaccharides	Chitosan
				Hyaluronic Acid
				Alginates
				Starch-based materials
				Bacterial Cellulose
				Dextrans
				Xanthan Gum
			Microbial Polyesters	Polyhydroxyalkanoates (PHA's)

Table 1.1. Overview of biocompatible materials that are commonly used as bone substitutes.

1.2.2.a. Metals

Apart from magnesium, all other metals currently used in orthopaedic procedures such as steel, tantalum, titanium and their alloys are not biodegradable and therefore will not be discussed in the present literature review. However, it is worth pointing out a complication that often arises with the use of metal implants: *Stress shielding* is a term used to describe the non-uniform stress distribution throughout a bone organ, as a result of mismatch between the mechanical properties of an implant and its host tissue. When stress shielding occurs, certain areas are not subjected to adequate levels of mechanical stimulus and are therefore resorbed, while others experience high levels of strain which leads to an increase in bone density according to Wolff's law. Wolff's law, in its general sense, is the concept that bone adapts to its mechanical environment during life, otherwise termed as "functional adaptation" (Ruff et al., 2006). This may result in fractures, especially amongst patients with osteoporosis. To prevent stress shielding, implants (including grafts) should exhibit an elastic modulus that does not exceed that of native bone tissue.

1.2.2.b. Ceramics

Several types of ceramics have been proposed as alternatives to autografts and allografts:

Bioglasses are silicate-based amorphous formulations that exhibit substantial osteoconductive and osteoinductive characteristics, due to a hydroxyapatite

surface layer that is formed after their immersion in physiological body fluids. It has also been observed that their dissolution products increase the rate of new bone formation, a certain advantage over other ceramic biomaterials. (Gerhardt and Boccaccini, 2010).

Fig. 1.5. Compressive strength of bioglass scaffolds from 20 different studies grouped by fabrication method, after (Fu et al., 2011a).

The partial substitution of silicate with borate in a bioglass formulation allows for the control of its degradation rate. It is also possible to dope the biomaterial with trace quantities of elements that favour bone growth, such as Cu, Zn and Sr. Additionally, this class of ceramics show potential for soft tissue repair or regeneration applications, owing to their angiogenetic properties. Their ionic degradation products have also demonstrated a remarkable ability to promote osteochondral tissue growth in cell seeded hydrogels (Chen et al., 2012; Rahaman

et al., 2011). Nonetheless, bioglasses lack in tensile strength and are inherently brittle, which limits their applications to non-load-bearing sites.

Calcium phosphate ceramics (CPC) are used extensively as fillers and implant coatings due to their chemical similarity to the mineral phase of native bone tissue. Besides their biocompatibility, they also exhibit bioactive and osteoconductive properties, which make them suitable for applications in regenerative medicine. The main types of calcium orthophosphates are hydroxylapatite (HA), beta-tricalcium phosphate (β-TCP), alpha-tricalcium phosphate (α-TCP) and biphasic tricalcium phosphate (BCP), which is a mixture of the above (Dorozhkin, 2013, 2010). β-TCP is the low-temperature polymorph of TCP, while α-TCP forms at temperatures above 1125°C. The latter is highly soluble and reactive and is mainly used in the preparation of calcium phosphate cements (Carrodeguas and Aza, 2011). In physiological conditions, HA is resorbed at a slower rate in comparison to α and β-TCP owing to its low solubility. The biodegradation rate of BCPs therefore can be controlled through their TCP/HA ratio. Apart from composition, grain size and level of crystallinity can also affect their performance in vivo (Kolk et al., 2012). Unfortunately, CPCs suffer from poor mechanical performance, which limits their use to non-load-bearing sites. Their strength is even further decreased by the presence of pores, an essential structural feature in bone substitutes. This could potentially be addressed by the inclusion of polymeric reinforcements, as described in the paragraphs that follow. Nonetheless, CPCs remain the only type of biomaterial whose degradation products can be used for new bone formation,

since calcium and phosphate ions are known to regulate bone metabolism and cell activity (Bohner, 2010a).

Cements and *putties* were introduced to the market at the turn of the century. They are both mixtures of hydrogels and ceramic nano- or micro-particles, the difference being that putties are non-setting formulations. One can distinguish between three types of products: pre-mixed, mixed during delivery and mixed prior to use (Bohner, 2010b). In cements, hardening can be a result of reactions between different calcium phosphate compounds, between calcium and a carboxylic acid or between calcium phosphate and an aqueous polymer solution (Chow, 2009). Based on their reaction products, calcium phosphate cements are divided in two major categories: apatite and brushite. The setting of these materials is initiated by mixing a powder with an aqueous solution. The main advantages of cements and putties is their ease of processing and their handling at physiological conditions, which permits the embodiment of drugs and bioactive molecules (Ginebra et al., 2010).

Major drawbacks of cements are the lack of permeability and the small size of the pores (8-12 μm), which hinder their biodegradation and new bone ingrowth. As can be seen in Fig. 1.6, a high proportion of the injected cement remains after a prolonged period of time. Unfortunately, cements exhibit brittle failure and are therefore limited to non-critical applications. A promising strategy for addressing their brittleness is the incorporation of long continuous fibres or polymeric additives (Krüger and Groll, 2012). Polymers are also used to create macro-porosity or control the setting rate of a cement (Perez et al., 2012). The use of medical

grade calcium sulphate hemihydrate and calcium sulphate dehydrate has also been reported, but their mechanism of resorption via chemical dissolution makes them less suitable as bone substitutes (Bohner, 2010a).

Fig. 1.6. Treatment of giant cell tumour in distal femur with bone cement and internal fixation: xray images taken 4 days (left) and 31 months (right) post-surgery (Source: Yu et al. 2013).

1.2.2.c. Polymers

Both synthetic and natural *polymeric* materials have been proposed for applications in hard tissue engineering. Synthetic polymers such as short chain saturated aliphatic polyesters (polylactic acid, polyglycolide, poly(lactic-co-glycolic acid) etc.) and polycaprolactone (PCL) (Woodruff and Hutmacher, 2010) have been approved by the FDA for use in implantable devices. Other synthetic polymers include bioresorbable poly(urethanes), poly(propylene fumarate), polyphosphazenes and poly(1,4-butylene succinate). Their main advantages are

the ability to tune their physical and chemical characteristics and ease of processing. Despite their favourable mechanical properties in comparison to natural polymers, their degradation products are often acidic, causing inflammatory response and adverse tissue reactions. On the other hand, natural polymers offer low toxicity, low manufacture and disposal costs and good cell adhesion. They can be divided into three main categories: proteins, polysaccharides and microbial polyesters. Proteins, such as collagen (Ferreira et al., 2012) and silk fibroin have been used widely in clinical applications. Chitosan (Costa-Pinto et al., 2011), hyaluronic acid, alginates, starch-based materials, bacterial cellulose and dextrans belong to the family of polysaccharides. They can be obtained from wood, plants, algae, marine crustaceans or prokaryotic cells (e.g. bacteria) and consist primarily of up to 40 different types of monosaccharides. These polymers are processed to form fibres, sponges, membranes and hydrogels that can act as ECM substitutes. Microbial polyesters, such as polyhydroxyalkanoates (PHAs), have tunable mechanical and biodegradation properties but entail high production costs. Synthetic and natural polymers have been combined to give composites with tailored wettability, strength and biodegradation rate. Depending on the processing technique that is employed, growth factors, chemical signals and drugs can also be embedded to support new tissue formation. However, the majority of biologically derived polymers are limited by their low mechanical strength and high water solubility, as well as the presence of impurities or toxic cross-linkers that may affect their in vivo behaviour (Correlo et al., 2011; Puppi et al., 2010). In general, polymeric compounds, irrespective of their origin, suffer from rapid strength degradation after

implantation (Bose et al., 2012) and exhibit low stiffness and plastic (irreversible) deformation under loading.

1.2.2.d. Polymer-ceramic composite materials

Polymer/ceramic composites: So far, numerous combinations of polymeric (synthetic or natural) and ceramic materials in various structural arrangements have been developed, inspired by the organic/inorganic composite nature of hard tissue. Such composites take advantage of the qualities of both classes of materials to deliver structures with enhanced mechanical and biological properties. Additionally, this strategy offers the possibility to control the biodegradation rate of a scaffold and maintain physiological conditions in the site of implantation (Bose et al., 2012). The latter is due to the fact that the by-products of polymer degradation can be buffered by the basic degradation of bioceramics, offering a favourable environment for cells and reducing inflammatory reactions (Chen et al., 2012). For a comprehensive list of CPC- and Bioglass-based composites the reader can refer to (Chen et al., 2012; Fu et al., 2011a; Mohamad Yunos et al., 2008; Rezwan et al., 2006). One can distinguish between four main fabrication routes:

1) The reinforcement of a polymer matrix with ceramic particles or fibres.

2) The infiltration of a sintered or partially-sintered ceramic matrix with a polymer or polymer/ceramic phase. The employment of this strategy in the production of PLA/β-TCP composites resulted in strength values similar to those of cortical bone for the same degree of density (Martínez-vázquez et

al., 2010). Coating the struts of a ceramic scaffold with a biodegradable polymer can also act as a defect healing and crack bridging mechanism while maintaining its porosity and microarchitecture (Boccaccini et al., 2009; Chevalier and Gremillard, 2009). This has been demonstrated by recent work from (Henriksen et al., 2011), where scaffolds consisting of HA and β-TCP in a 70:30 ratio were coated with Poly(D,L)-lactic acid. Destructive compression testing of the samples revealed a manyfold increase in stiffness and ultimate strength, their values being within the range of those for human trabecular bone.

3) Addition of a water-soluble polymer in a calcium phosphate powder or liquid phase cement (Perez et al., 2012).

4) The biomimetic route typically involves mimicking the biological processes of self-assembly and self-organisation to obtain organic/inorganic composites with nano-structural features similar to living bone tissue. Several bio-inspired techniques are reviewed in (Cui et al., 2007; Green et al., 2002; Holzwarth and Ma, 2011; Ma, 2008) and Tampieri et al. (2011).

1.2.3. Processing techniques

A plethora of processing techniques have been employed so far in an attempt to fabricate synthetic bone substitutes that resemble native extracellular matrix both structurally and compositionally. In this review, manufacturing techniques are divided in two main categories: conventional and digital.

1.2.3.a. Conventional fabrication techniques

Conventional techniques include casting, fibre bonding, electrospinning, sol-gel, foam replica, solvent casting with or without particulate leaching (see Fig. 1.7), thermally induced phase separation combined with freeze-drying, in situ mineralisation of HA in polymers and electrodeposition (Bergstrom, 2001; Singh et al., 2008; Sun et al., 2011).

Fig 1.7. Scanning electron micrographs of PLLA nano-fibrous scaffolds at 100x (A) and 10,000x (B) obtained from a combined sugar sphere template leaching and phase separation technique, after (Wei et al., 2007).

1.2.3.b. Digital fabrication techniques

Digital techniques can be distinguished between Subtractive and Additive. Automated subtractive manufacturing is a computer numerically controlled (CNC) process of machining a raw material to a desired shape and size.

Fig. 1.8. Conceptual 3D printed hydroxyapatite scaffold for mandibular bone reconstruction (Source: Beckman Institute, University of Illinois).

Additive manufacturing (AM) or Solid Freeform Fabrication (SFF) technology has recently gained the scientific community's attention due to the wide spectrum of its potential applications. Originally used for rapid prototyping, it did not take long to appreciate its ability of fabricating parts of great complexity that are suitable for end use. The term encompasses a number of different manufacturing techniques that share a common approach: the object is built layer by layer, which allows for the precise control of its internal structure and composition (Campbell et al., 2012). In tissue engineering, the most popular AM tools employed so far include: powder-

based 3D printing (3DP) (shown in Fig. 1.8), droplet-based inkjet printing of UV-curable polymers, Stereolithography (STL), Selective Laser Sintering (SLS) and extrusion-based techniques (Bartolo et al., 2012; Billiet et al., 2012). No technique has yet managed to deliver a solution that fulfils all the requirements for synthetic bone substitutes. Each process has both advantages and shortcomings (Melchels et al., 2012). These are discussed extensively in Chapter 2.

1.2.4. Structural hierarchy in native bone tissue

Although polymer/ceramic composites are currently the most promising candidate materials for synthetic bone substitutes, replicating the organic-inorganic composition of native tissue does not seem to suffice (see Fig. 1.9). It has become evident that research needs to look even further into biological materials for inspiration.

Fig. 1.9. Ashby plot of Compressive Strength vs Elastic Modulus for biodegradable scaffolds reviewed in (Rezwan et al., 2006) in comparison to bone tissue.

The solution may lie in the structural arrangement of a composite's components at different scales, termed structural hierarchy. R. Lakes (1993) has given the following definition of structural hierarchy: "Hierarchical materials contain structural elements which themselves have structure." Hierarchy is a common characteristic amongst biological materials. It is Nature's way of producing tough structures that serve multiple functions, while making efficient use of a limited range of materials. This strategy has also been applied to bone tissue, a collagen/apatite composite with an organic-to-inorganic ratio of approximately 1:2. A simple mixing of its components would result into a soft pasty material, with mechanical properties far inferior to the ones observed in bone.

The remarkable mechanical properties of bone are the effect of a highly complex and hierarchical structure, which has been optimised through evolution to meet several biological requirements. A good understanding of the mechanisms that contribute to its mechanical performance may reveal strategies for fabricating better bioresorbable synthetic grafts in the future:

Fig. 1.10. Illustration of the seven hierarchical levels of bone tissue (Rho, 1998).

At a microscopic level, hard tissue consists of collagen mineralised with crystals of calcium phosphate (see Fig. 1.10). The two materials are assembled into fibrils, which are bundled together to form fibres. The fibres are then arranged in a twisted plywood motif to form lamellae, the main structural element of osteons in cortical bone (Rho, 1998). It is important to mention the role of collagen fibres in bridging a developing crack and the presence of other energy dissipation mechanisms, such as crack deflection and twist and constrained micro-cracking that increase drastically the required energy to fracture (Ritchie et al., 2009). Surprisingly enough, fracture toughness is not only dependent on the degree of mineralisation, but also on the average size of apatite crystallites, which increases with increasing age (Davison et al., 2006).

Macroscopically, one can distinguish between two types of osseous tissue:

- The cortical or compact bone forms the hard shell of bones but is porous enough to host cells and a vascular network. Its biomechanical properties are strongly influenced by the porosity and the mineralisation of the organic matrix (Weiner and Traub, 1992), as well as the thickness and diameter of the cortex (Davison et al., 2006).

- The trabecular bone, otherwise termed as spongy bone, is the porous interior that acts as a shock absorber upon impact. It exhibits lower hardness, stiffness and strength in comparison to cortical bone. It also consists of trabecular struts varying in size and orientation that are

continuously remodelled to withstand dynamic mechanical loading (see Fig. 1.11). The major factors influencing the mechanical behaviour of spongy bone are the apparent density and the microstructural arrangement of the trabeculae (struts). The latter involves the number of trabeculae in a given volume, their average thickness, the average distance between adjacent trabeculae, and the degree to which trabeculae are connected to each other (Bouxsein, 2013; Davison et al., 2006). These factors differ largely, even between regions of the same bone organ (Giesen et al., 2001). It has also been noted that the majority of trabeculae are not straight, which results into a lower effective modulus of the overall structure. It is possible that a certain degree of flexibility is necessary to protect the articular cartilage from peak stresses (Miller and Fuchs, 2005). Trabeculae also display ductile buckling in the wet state that favours the compressive strength of trabecular bone, a phenomenon which is partially explained by the lower mineral content of their surface as opposed to their highly mineralised core (Van Der Linden et al., 2001).

Other examples of hierarchical materials in nature are wood, nacre (mother of pearl) and glass sponge skeletons (euplectella aspergillum). What they all share in common is their emergence through a process of self-assembly, growth and functional adaptation. In contrast, engineered materials are static, designed and fabricated according to specific requirements. In addition to hierarchy, nature's dynamic strategy offers the following advantages:

- *Adaptation*: biological materials can adapt to changing functions as they grow and get continuously modelled and remodelled. According to an anecdote, one of the first observations of this attribute in bones was in 1866, when professor Culmann (German engineer who pioneered the method of graphic statics) visited his colleague Dr. Meyer in his dissecting room. He remarked that the arrangement of the trabeculae in a section of a femur was in fact a diagram of the stress lines in the loaded structure (Fig. 1.11). Indeed, trabecular bone is continuously remodelled to accommodate for any changes in the mechanical distribution of compressive or tensile stress (Thompson 1917).

Fig. 1.11. Section of human femur with trabecular and cortical bone regions (left) and diagram of stress lines in the loaded structure (right) (after Koch, 1917).

- *Self-repair and regeneration:* biological materials employ cells that act as healing agents when subjected to damage.

- *Functional gradients:* the microstructure and composition of each region is varied depending on local requirements and constraints (Dunlop et al., 2011; Fratzl and Weinkamer, 2007).

1.3. Problem statement and Aims & Objectives

Despite the vast range of available materials for bone tissue reconstruction and substitution, not one has managed so far to fulfil the multiple biological and mechanical requirements associated with large defects. Some of the most promising candidates are polymer/ceramic composites. However, porosity has a detrimental effect on their mechanical performance. It has been proven that biological materials owe their unique mechanical properties largely to structural hierarchy. A question arises as to whether a similar design strategy could provide a solution in the field of tissue engineering. Currently, there are a plethora of available techniques for tailoring the architecture of engineered scaffolds. Amongst them, Additive Manufacturing allows for the most precise control of the composition, microstructure and overall geometry of a scaffold. Incorporating micron and submicron-scale features, however, necessitates very high resolutions, having implications on lead times and cost. Physical and chemical processes have been used extensively for structuring bulk materials. A synergy between these commonly called "conventional techniques" and additive manufacturing could in theory deliver hierarchical composites with superior fracture resistance.

This research is exploring the possibilities that arise from incorporating two different physical processes in extrusion-based additive manufacturing:

- The first involves dispensing a hydrogel-based β-tricalcium phosphate (β-TCP) paste in an ambient temperature that is below the freezing point of water. This approach makes use of ice-crystal growth as a driving force for assembling the paste's particles at the micro-scale.

- The second, employs rapid water evaporation from the surface of an extruded filament with the parallel growth of a continuous void in its centre. The formation of a rigid porous shell is facilitated by the addition of cellulose nano-fibrils in the β-TCP paste formulation.

The aim of this research is to assess the level of microstructural control that each one of these combinational methods can achieve.

Figure 1.12 provides a schematic overview of the thesis and its main objectives, structured in six chapters as follows:

The first chapter gives an overview of the state of the art in terms of materials and processing techniques for synthetic hard tissue substitutes. It particularly emphasises the challenges that prevent their use as alternatives to bio-derived bone grafts and draws on nature's design principles to suggest possible solutions.
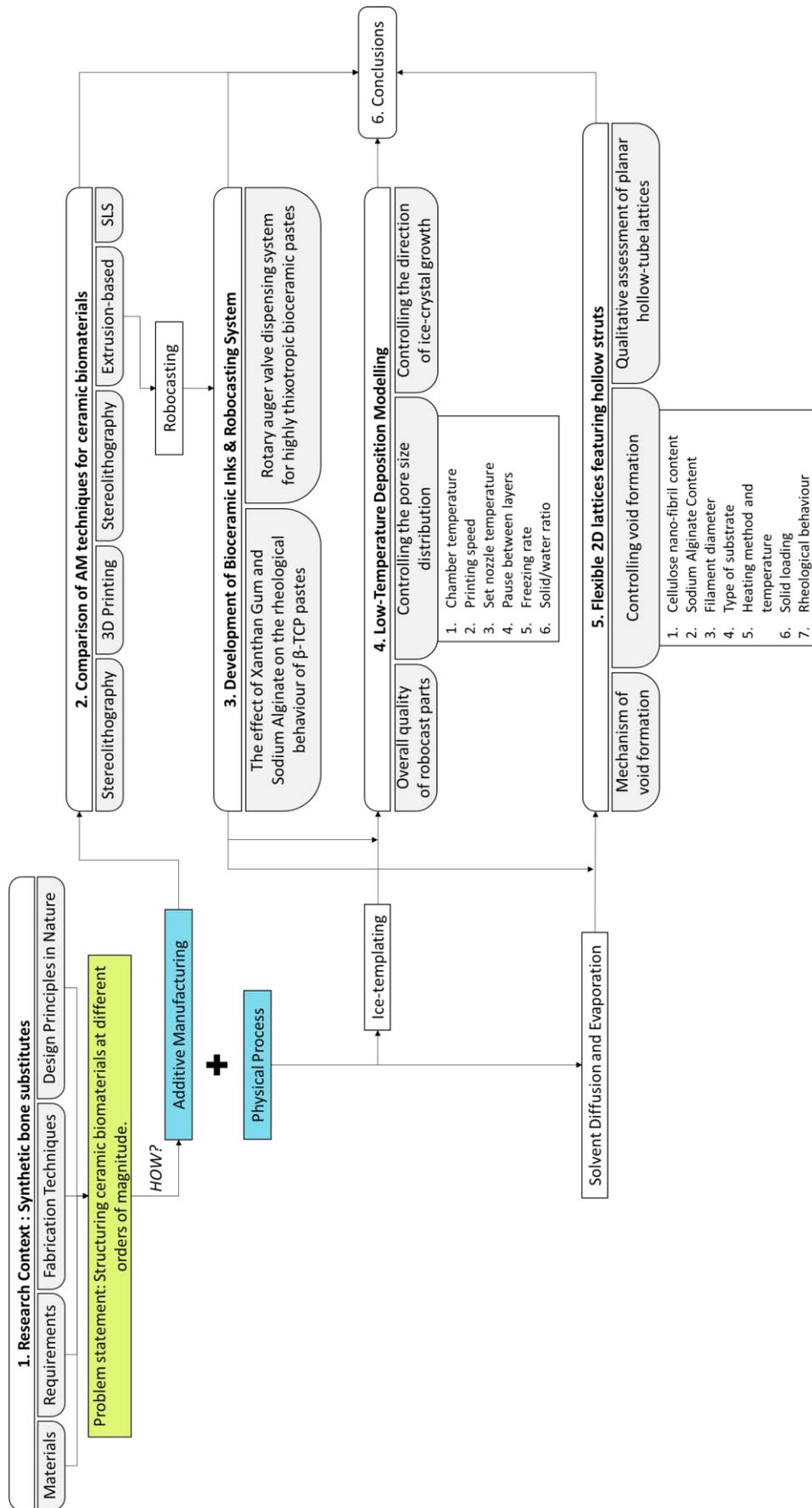
Fig. 1.12. Schematic overview of the thesis.

Chapter two provides a comparison between the available additive manufacturing techniques for ceramic bio-materials, as well as an argument for selecting an extrusion-based technique (i.e. Robocasting). Furthermore, it lists a number of examples where Robocasting has been combined successfully with other materials-processing methods to deliver hierarchically structured composites. Finally, it explains the rationale behind using ice-crystal growth as a way of micro-structuring a ceramic material as it is being printed.

Chapter three focuses on the development of thixotropic calcium phosphate pastes together with a versatile dispensing system that can handle fluids with a wide range of viscous behaviours.

Chapter four presents the experimental methods used to establish a link between the parameters of the proposed manufacturing method and the microstructure of a finished part. The main findings are discussed in an effort to understand the physical phenomena taking place during the printing process. This chapter, which constitutes the main body of research, attempts to ascertain the degree of accuracy that freezing can offer in controlling the micromorphology of robocast scaffolds.

Chapter five investigates the use of cellulose nano-fibrils in conjunction with thermal processing for Robocasting lattices that consist of hollow struts. A series of experiments assisted in gaining an insight into the mechanism of void formation within a filament and in enhancing both the formulation and the process to achieve

the optimum structural outcome. Crosslinking of the paste formulation in the presence of Ca^{2+} opens up opportunities for robocasting flexible scaffolds with submillimetre features and increased geometric complexity.

The last chapter of this thesis begins with a synopsis of the main findings, followed by a critical evaluation of the methods and materials used. It concludes with suggestions for a number of possible directions that the research project could take in the future.

Chapter 2

Robocasting as a method for structuring biomaterials at different orders of magnitude

In the field of tissue engineering, Additive Manufacturing (AM) has grown in popularity over the last decade thanks to its unparalleled precision in controlling the internal architecture of biomedical implants. Nowadays, there are a multitude of AM techniques for ceramic and composite bio-materials available, each with their advantages and drawbacks. These can be grouped into four main categories, which will be analysed in the section that follows. It has become evident that digital fabrication techniques in isolation are not capable of delivering a complete solution that fulfils all the requirements for synthetic bone substitutes. For this reason, there is currently a trend towards combining AM with well-established conventional scaffold fabrication processes, discussed in Section 2.2.

2.1. Additive Manufacturing Techniques for Ceramic and Composite Biomaterials

AM has been employed both directly and indirectly for the fabrication of bioresorbable polymeric, ceramic or composite hard tissue scaffolds. An indirect approach involves using a freeform manufactured structure as a sacrificial mould to create the final product (L. Lu et al., 2010; Taboas et al., 2003). The paragraphs that follow describe the principles of operation for the main AM techniques employed in bio-ceramic processing. Additionally, they provide a comparative review between the available methods, highlighting not only their strengths but also their inherent limitations. This will offer a rationale behind selecting an extrusion-based technique for this research project.

2.1.1. Stereolithographic Ceramic Manufacturing (SLCM)
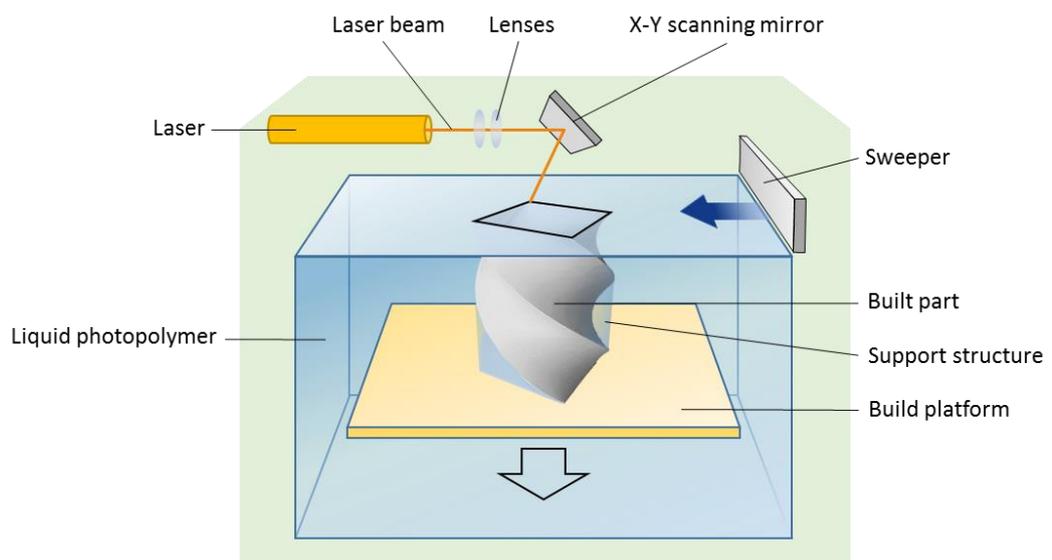
Fig.2.1. Typical Stereolithography setup and its main components.

The stereolithographic approach uses a liquid photo-reactive organic binder mixed with ceramic and glass-ceramic powders. It consists of three steps, namely printing, thermal debinding and finally sintering. Thermal debinding, otherwise termed

burnout process, involves the removal of the polymer phase from a printed part with controlled heating. A typical system comprises a tank that contains a photosensitive ceramic slurry, a moveable build platform and an ultraviolet laser, which cures areas where it is focused on the surface of the slurry (see Fig. 2.1). The latter is controlled by a dynamic mirror system. The first layer is polymerised on the platform, remaining attached throughout the entire printing process. Subsequently, the platform is vertically lowered so that a sub-millimetre layer of liquid covers the previous layer. The steps are repeated until a complete 3D part is formed. Any uncured slurry is washed off and the finished structure is heat-treated to obtain a green body (weakly bound ceramic part), followed by sintering to consolidate the ceramic particles (Travitzky et al., 2014). A variation of this process is digital light processing (DLP), which projects each time the image of a cross-section (dynamic mask) on the bottom surface of the photosensitive slurry, reducing significantly the fabrication time (Gmeiner et al., 2015). Typical resolutions for SLA are in the range of 50 µm but new techniques, such as micro-SLA (µSLA) and Two-Photon Polymerisation (TPP) can generate finer features. Micro-SLA has produced ceramic parts with a layer thickness of less than 5 µm using a single photon beam (Zhang et al., 1999). TPP has achieved resolutions down to the nanoscale (100 nm) with a short pulsed near-infrared laser beam that is focused on a particular spot within the resin volume. This technique is however limited to the use of highly transparent resins, such as organic-inorganic hybrid materials (ORMOCER®)(Narayan, 2010).

Fig 2.2. Bioglass cellular scaffold fabricated using Stereolithography (Source: Gmeiner et al. 2015).

Stereolithography (STL) can give scaffolds with well-defined architecture at high resolutions (see Fig. 2.2) but the use of ceramic suspensions can impact on its speed. Ceramic particles are opaque and therefore a relatively long exposure is required for such mixtures to photopolymerise. Additionally, the photo-initiators used are often cytotoxic and the process is limited to a single material of low viscosity (below 5 Pa.s) (Melchels et al., 2010). For this reason, only slurries with low solid content can be used (ranging between 20 and 50% by volume), which results in high shrinkage during production and post-processing (Mota et al., 2012; Thavornyutikarn et al., 2014). Moreover, there is a limited number of photo-polymerisable materials available and there is currently no simple method for producing structures that consist of multiple materials. Choi et al. (2011) have developed a multi-material system that makes use of a rotating vat carousel, but there are still several issues that remain to be addressed associated with laser shadowing, trapped volumes and differences in surface tension between the different photosensitive resins.

2.1.2. 3D Printing (3DP)

3D printing (3DP) is a powder-based technique, in which an inkjet print-head sprays a binder on loose ceramic powder to consolidate its particles. It has been extensively used in hard tissue engineering, as it allows for the direct fabrication of scaffolds with tailored architecture and porosity. A schematic of this technique is presented in Figure 2.3. The process starts with packing an amount of powder in a feeder bed. A set of rollers spread and slightly compress an even layer of powder from the feeder to the deposition bed. Its thickness is mainly determined by the object's geometry and the characteristics of the powder. The print-head sprays a pattern across the deposition bed which corresponds to a cross-section of the CAD model. There are two approaches when selecting a binder; it can either be an organic solvent/polymeric glue for binding the particles together or an aqueous solution that triggers a crystallisation reaction similar to the hydraulic setting of cements (Low Temperature Printing, LTP). An example of the second approach as stated above has been demonstrated by Suwanprateeb (2012), who 3D printed a scaffold with plaster of Paris, which was then transformed to hydroxyapatite through dipping into a di-sodium hydrogen phosphate solution. This technique offers short fabrication times, as no heat treatment is required and high compressive strengths. After the pattern is deposited, the printing bed is lowered, while the feeder is lifted in order to spread another layer of powder. The process is repeated until the part is completed, followed by drying and depowdering. The latter involves removing any loose unbound particles with a compressed air blower. Sintering in a furnace is only necessary when the resulting part is a green body (Bose et al., 2013; Castilho et al., 2013; Fielding et al., 2011).

Fig. 2.3. Schematic representation of the 3D printing (3DP) process (Source: Fielding et al. 2011).

One of the major advantages of 3DP are its low cost and ability to process a wide range of ceramic materials. It is also possible to print parts with highly complex internal structures and overhangs without the need for support structures. Low Temperature Printing in particular allows for incorporating biologically active molecules inside the scaffolds, as no heat or toxic solvents are required (Thavornyutikarn et al., 2014). In a study conducted by Inzana et al. (2014), collagen was added to the binder solution (phosphoric acid) to improve the strength and biological properties of calcium phosphate scaffolds implanted in vivo. Furthermore, its ability to deposit multiple inks simultaneously offers the potential to print structures that consist of different types of cells, materials and bioactive agents (Chia and Wu, 2015). Additionally, the surface of 3D printed scaffolds is inherently rough due to the imperfect packing of powder particles, a feature which highly favours cell adhesion (Cox et al., 2015).

Fig. 2.4. 3D Printed calcium phosphate scaffold with noticeable layers evidencing its build orientation (Source: Butscher et al. 2011).

However, 3DP has some substantial drawbacks, such as the low density of green bodies (unfired objects) and its limited resolution in the range of 100-200 μm. The former can result into parts with poor mechanical properties that can easily crack during depowdering and post-processing. Additionally, it causes significant shrinkage upon the sintering step, which can introduce distortions and cracks (Bose et al., 2013; Mota et al., 2012). Also, it is important to mention the difficulty to remove loose particles from small cavities (Butscher et al., 2011) and the anisotropic mechanical behaviour of 3D printed scaffolds. More specifically, depending on the orientation in which a scaffold is printed (see Fig. 2.4), its strength can be compromised in certain directions (Castilho et al., 2013). The technique's resolution is to a large extent limited by the drop size and the physical properties of powders, as described in detail by (Butscher et al., 2012). Fine powders tend to form agglomerates due to particle-particle interactions that

dominate gravitational forces, reducing their flowability and causing uneven spreading on the deposition bed.

2.1.3. Selective Laser Sintering (SLS)

Selective Laser Sintering is based on the same principle as 3DP. The main difference lies in the use of a high-energy laser beam source for the direct fusion of powder particles through their complete or partial melting, as opposed to spraying a binder with an inkjet head. The process is usually carried out in a controlled atmosphere or under vacuum. There are three main categories of SLS, classified according to their consolidation mechanism; these are solid state sintering, liquid phase sintering and melt-solidification. The beam's intensity and the duration of interaction can be adjusted in order to achieve the desirable mechanism. For a detailed description of those mechanisms, the reader can refer to Kruth et al. (2007).

Although SLS is a well-established polymer and metal processing technique, sintering of ceramic materials is still in its infancy. Depending on the composition of the powder, one can distinguish between a direct and an indirect approach to ceramics processing. The latter involves using an organic (thermoplastics) or inorganic (e.g. glass) phase with a low melting point as a binder. This strategy is particularly useful due to the high glass transition temperature of many ceramic materials. An additional sintering step may be required to consolidate the printed object. In the case of inorganic binders (e.g. glass), it is worth mentioning that they cannot be burnt out, remaining embedded in the ceramic matrix. A novel method

employs the laser beam to simultaneously induce high-temperature synthesis reactions while printing. In this case, the powder bed consists of reagents mixed in their dry form (Travitzky et al., 2014). According to Qian & Shen (2013), SLS can deliver structures that exhibit hierarchy through controlling the crystallization and microstructural evolution of the ceramic. Additionally, the extreme heating and cooling rates it entails, can form phases that are difficult to obtain with conventional sintering approaches. The typical resolution of an SLS system is within the 100 μm range, making it ideal for fabricating parts with fine features (see Fig. 2.5). Also, loose powder acts as a support structure, allowing for high levels of geometric complexity.

Fig. 2.5. Left: thin walls fabricated from pure zirconia to assess the precision of SLS, right: top view of open porosity in zirconia cube (Source: Bertrand et al. 2007).

However, achieving satisfactory mechanical performance and dimensional accuracy can be challenging owing to the complexity of the process. Multiple parameters need to be considered, such as the build orientation, scan spacing and

pattern, particle size, packing density and laser intensity (Mota et al. 2012). This perhaps makes SLS one of the least versatile AM techniques.

Besides the difficulty in removing loose powder trapped in small cavities, there is a great number of problems that remain to be addressed. For example, the short interaction between the laser and the particles results in bodies with low density and poor mechanical performance, as observed in Figure 2.5 (Travitzky et al. 2014). Particularly with ceramics, the melted area is slightly larger than the size of the focused beam. This is due to their poor thermal conductivity which results into the accumulation of heat energy. Another issue is the formation of cracks caused by the rapid heating and cooling. This has been partially addressed by preheating the powder bed and post-annealing the final part to remove any residual stresses (Qian and Shen, 2013). However, achieving and maintaining high temperatures with a uniform profile throughout the powder bed remains a difficult task, resulting in parts with irregular morphology (Bartolo et al., 2012). Furthermore, high temperatures pose limitations to the range of materials that can be used in SLS. For example, natural polymers, hydrogels and bioactive molecules, all used extensively in tissue engineering, dissociate at high temperatures and are therefore excluded (Billiet et al., 2012). An extensive list of examples in the field of tissue engineering can be found in Mota et al., 2012. The review particularly highlights the high cost of the process as one its major drawbacks.

2.1.4. Filament-based techniques

The filament-based family of AM techniques encompasses a great number of different approaches that share the principle of filamentary extrusion along predefined paths to create three-dimensional constructs. They all stem from Fused Deposition Modelling (FDM), in which a thermoplastic is melted and extruded through a heated nozzle. A typical configuration is illustrated in Fig 2.6. It comprises a print-head that moves in the x-y plane and a heated build platform that is lowered along the z axis each time a new layer is added. The material, in the form of filament, is fed into the print-head through two rotating rollers, actuated by a stepper motor. The extrudate bonds with the underlying layers and solidifies upon cooling to form a layer. If a part contains overhangs, the technique necessitates an additional nozzle for temporary support structures that are dissolved in a separate step.
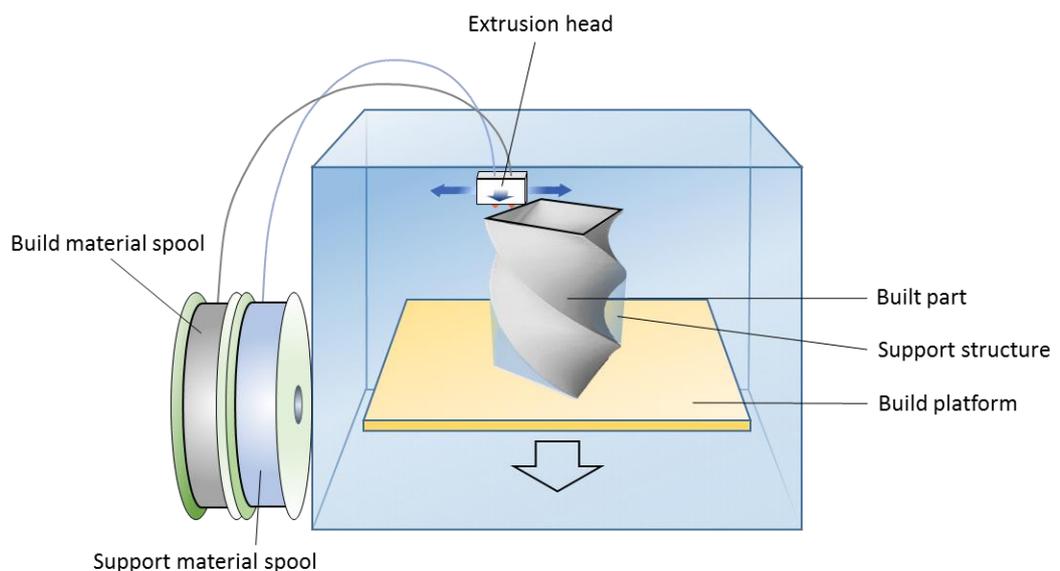
Fig. 2.6. Fused Deposition Modelling process and its main components.

FDC (Fused Deposition of Ceramics) is an FDM variant that uses ceramic-filled thermoplastics as feedstock to assemble polymer/ceramic composites or pure ceramic objects. In the latter case, the polymeric phase can be burnt away in a heating stage, followed by sintering to produce a fully dense ceramic body. Both FDM and FDC can produce parts that consist of multiple materials and possess the unique capability of introducing compositional gradients during the course of printing. FDC inks exhibit strong shear-thinning behaviour thanks to their high polymer content (50-55%), which facilitates their extrusion. Additionally, their solid filamentous form offers extended shelf-life in comparison to other extrusion-based techniques. Yet, the use of thermoplastics shaped in the form of filament limits considerably the range of biomaterials that can be processed. Green bodies obtained from FDC are exceptionally strong, which assists in handling during post-treatment. However, the debinding procedure can last several hours due to their high polymer content and can potentially cause structural defects and limited densification in the sintered part (Smay, 2006). Furthermore, it is not possible to incorporate bioactive agents or drugs, as the printing process involves high temperatures (Chia and Wu, 2015). Precision Extruding Deposition (PED) is a more versatile alternative, where raw materials are fed into a liquefying chamber in the form of pellets. PED offers a precise control of the extrusion rate through the use of a heated barrel and a reciprocating screw, very similar to an injection moulding machine (Thavornyutikarn et al., 2014). Twin screw systems have also been proposed for mixing multiple feeds before deposition (Kalyon et al., 2013).

Fig. 2.7. Fused Deposition Modelled scaffold for cranial bone defect, by Queensland University of Technology, Institute of Health and Regenerative Medicine (Source: Science Museum).

To extend the range of raw materials suitable for processing, a number of techniques have been developed that employ different mechanisms of state change other than temperature-induced liquid-to-glass transition (e.g. FDM, FDC, PED), such as crystallisation, gelation, polymerisation, dilatant transition and solvent evaporation (X. Lu et al., 2010). Several terms can be found in literature for these extrusion-based methods, many of which can be used interchangeably. It is often difficult to distinguish between them, as they share similar principles and their differences are, in most cases, minor. The extrudate is usually a colloidal suspension or paste that flows when subjected to shear and recovers its stiffness immediately after its deposition. This viscoelastic behaviour prevents the filament from collapsing under its own weight before it solidifies. A successful ink formulation should also enable the deposition of free-spanning filaments (bridges) with minimal sagging, as well as support layers that are added above it (Billiet et al., 2012).

Fig. 2.8. Left: Schematic representation of continuous filament writing (Source: Lewis & Gratson 2004, right: Robocast 45S5 bioactive glass scaffolds (Source: Eqtesadi et al. 2014).

Robocasting or Direct Ink Writing (DIW) (see Fig. 2.8) uses highly concentrated ceramic pastes to minimise shrinkage and cracking as they dry. Even the slightest evaporation of the continuous phase induces a change in the rheological behaviour from shear-thinning to shear-thickening. *Unfold*, a Belgian design studio, has demonstrated very effectively the possibilities of this approach by robocasting some intricate decorative objects from porcelain, shown in Fig. 2.9. Such degree of complexity is yet to be seen in the fabrication of hard tissue scaffolds. However, high solid content coupled with fast drying kinetics can cause clogging at the tip of the nozzle, limiting the extrusion's minimum thickness to about 500 µm (Smay, 2006). For this reason, gel-based nano-particulate inks with reduced solid loading have been developed to be used with micro-nozzles in the range of 1-100 µm (Lewis, 2006).

Fig. 2.9. Unfold studio's "ceramic 3D printing" project (source: unfoldfab.blogspot.co.uk).

3D Bioplotting is a Robocasting variant in which the suspension is kept in a heated cartridge and extruded into a temperature controlled bath. A plotting medium of specific density induces solidification via temperature change or chemical reaction. A commercial bioplotting device can be seen in Fig. 2.10. This approach eliminates to an extent the use of support structures, owing to the buoyancy that the printed structure experiences in the liquid medium (Abdelaal and Darwish, 2013). Furthermore, it constitutes, as the name suggests, the only extrusion-based technique that can handle cell-seeded inks, thanks to the well-controlled liquid environment and absence of toxic viscosity modifiers. One of its major drawbacks is the lack of mechanical strength in the final part, and the smooth surfaces it generates that hinder cell-adherence (Thavornyutikarn et al., 2014).

Fig. 2.10. Commercial 3D-bioplotting device by envisionTEC (Source: EnvisionTEC GmbH).

The cost of Robocasting machines can often be prohibitive. Moreover, as AM gets incorporated into an increasing number of processes, each with its own complexities, there is need for highly customisable systems with specialised functionalities that are difficult to find on the market. This had led many researchers to develop their own AM equipment, adopting a DIY (Do-It-Yourself) approach and sharing their designs, hacks and instructions with the wider 3D printing community. This paradigm shift has been accelerated by projects such as Fab@Home and RepRap, which made this technology accessible to the general public. The Fab@Home, illustrated in Fig. 2.11, is a low-cost open-source 3D printer developed at Cornell University's department of Mechanical & Aerospace Engineering. It was also one of the first systems used to fabricate functional multi-material parts i.e. actuators, sensors, batteries and hydrogel scaffolds of variable

stiffness (Mookerjee et al., 2009; Vilbrandt et al., 2008). The present research follows a similar methodology for the development of an inexpensive but reliable additive manufacturing tool, drawing solutions not only from academia, but also from online communities of "makers".

Fig. 2.11. Fab@Home 3D Printer with dual syringe extrusion tool (Source: solidsmack.com).

The dispensing systems employed in Robocasting techniques are either pressure- or volume-controlled. In pressure-assisted systems the extrusion rate is highly dependent on the rheological behaviour of the feedstock. As a result, they necessitate calibration even with minor changes in the extrudate's composition (Travitzky et al., 2014). On the contrary, volume-controlled dispensers, such as auger valves and progressive cavity pumps, offer a precise and consistent flow rate irrespective of the ink's flow behaviour. Chapter 3 discusses in more detail the appropriate viscoelastic properties for ceramic-filled inks, various ways of tailoring them and how these informed the design of the dispensing system.

2.2. Combinational approaches to additive manufacturing

Up to this point, research in AM has primarily focused on achieving high resolutions, which translates to long fabrication times. The scale-up of these processes is usually neglected, despite its importance in their transition from a lab setting to real clinical applications. Furthermore, although they provide precise control over the macroporosity and overall geometry of patient-specific bone substitutes, they are often unsuccessful in generating micro-features that play an essential role in their biological and mechanical behaviour. For example, additively manufactured scaffolds tend to have smooth struts that hinder cell adhesion during the seeding process. The latest research also highlights the need for mimicking toughening mechanisms that exist in bone at the micron and sub-micron scale in order to achieve strong scaffolds with high fracture toughness (Fu et al., 2013). Additive and well-established conventional manufacturing techniques can be used synergistically towards this end.

Fig. 2.12. SEM micrographs of (left) micro-structured PLA scaffolds via combination of FDM and direct laser writing ablation (Source: Malinauskas et al. 2014) and (right) PCL/TCP scaffold with fibrillar gelatin compartment fabricated with PED (screw extrusion) and conventional freeze-drying (Source: Arafat et al. 2013).

From Table 2.1. it can be concluded that filament-based techniques constitute the most versatile and economic methods for fabricating hard tissue engineering constructs. They can be easily combined with other manufacturing techniques, which could open up countless possibilities in structuring biomaterials. Using this approach, the shape and internal architecture of a scaffold can be controlled through a filament-based technique, while the desirable microstructural characteristics, such as surface roughness and porosity, can be achieved through conventional techniques. Thus far, filament-based techniques have been combined successfully with gel casting (Bian et al., 2012), solvent casting and particulate leaching (Taboas et al., 2003), freeze-drying (Peña et al., 2010) and electrospinning (Nandakumar et al., 2013). For a detailed review of this particular trend, the reader can refer to Giannitelli et al. (2015).

This study is investigating ways in which the material itself can assemble during or following its deposition into the desired configuration at the microscopic level. Robocasting lends itself to this approach because it operates at a wider temperature range than FDM, without the need for complete melting of the extrudate. For example, Schlordt et al. (2013) performed robocasting in an oil bath with nozzles that form seamless micro-tubes. The rheological characteristics of an alumina gel-based paste, its extrusion rate and oil viscosity were adjusted so that the filaments retain their tubular structure over the course of a printing process. Figure 2.13 shows a 3D lattice with hollow struts that was obtained from this hybrid method.

	Advantages	Disadvantages
Ceramic Stereolithography (SLCM)	• High resolution • Complex geometries • Wide range of ceramic materials • No heating/melting	• Low speed • Cytotoxic and limited range of photo-initiators • Slurries of low viscosity and solid content • Single material • High shrinkage of ceramic parts during production and post-processing • Support structures • High cost
3D Printing (3DP)	• No need for support structures • Can deliver functional end-use parts • Wide range of ceramic materials • Low cost • Ability to deposit multiple inks and bioactive molecules • Rough surfaces favour cell adhesion • No heating/melting	• Low green body density • Depowdering step can introduce distortions and cracks • Loose particles can be trapped in small cavities • Anisotropic mechanical behaviour • Limited resolution • Single powder material
Selective Laser Sintering (SLS)	• High resolution • Can induce high temperature synthesis reactions • Can generate hierarchical structures and form phases that cannot be obtained with conventional sintering techniques. • No need for support structures	• Extremely high temperatures • Insufficient mechanical performance due to low density • Cracks formed by extreme heating and cooling rates • Loose powder trapped in small cavities • Cannot be used with natural polymers • High cost
Filament-based Techniques (FDM and variants)	• High resolution • Multi-material structures • Can introduce compositional gradients • Can process a wide range of materials • Ability to print with cells and bioactive agents • Can handle both high and low solid content pastes • Hierarchical structures • Can be combined with existing conventional manufacturing techniques • Low cost	• Requires support structures • Debinding of green bodies with high polymer content can introduce cracks and distortions • Clogging at the tip of the extruder • Sensitive to ink rheology

Table 2.1. Advantages and disadvantages of AM techniques featured in this chapter.

Fig. 2.13. Left: μ-CT reconstruction of Robocast alumina three-dimensional lattice with hollow struts (Source: Schlordt et al. 2013), right: Hybrid PEOT /PBT scaffold consisting of alternating FDM and electrospun layers (Source: Nandakumar et al. 2013).

2.3. Parametric tool-path generation for filament-based techniques

Parametric design software is becoming increasingly popular in architecture, following a shift from a "structure-driven" to a "material-driven" approach to design. Traditionally in engineering, the selection of materials is based on constraints dictated by form. In nature, however, form emerges without a predetermined design, informed by the material itself (Oxman, 2010).

In Grasshopper for Rhinoceros®, the user can build an algorithm, in which the form of an object or building is described by a set of parameters, subjected to various environmental and functional constraints. These can be altered to examine a whole range of possible configurations or optimized to meet specific requirements. Additionally, it enables designers to define parametric relationships between different elements of a model. It provides a visual programming environment and most importantly the ability to view in real-time the resulting geometry during the

creation or modification of a script. In 3D printing, Grasshopper allows for the precise control of different processing and material parameters during the fabrication of a part. This offers the ability to generate form-finding systems, in which design computation, robot movement and material properties are integrated with feedback loops, as the latest work by Mostafavi & Bier (2016) suggests (Fig. 2.14). This particular feature could not only revolutionise architecture, but also the way we design and fabricate bio-inspired scaffolds for tissue engineering.

Fig. 2.14. Left: point cloud used for the extraction of continuous toolpaths, Right: resultant 1:1 scale prototype with employed robotic dispensing system (Source: Mostafavi & Bier 2016).

2.4. Ice segregation as a method for micro-structuring biomaterials

A truly biomimetic design approach would involve the emergence of an ordered structure through complex interactions between multiple agents subjected to mechanical and chemical stimuli. The entire process would take place in the absence of a pre-existing blueprint, in the same way as it occurs in biological and physical systems. However, the limitations imposed by the current state of

technology and the inadequate comprehension of complex biological processes deem it impossible to replicate nature's dynamic strategies. Nevertheless, before venturing into such level of biomimicry, it is worth examining alternative ways of structuring biomaterials. A *bio-inspired* route, might be able to provide solutions that are both attainable and more sophisticated than the current state-of-the-art. This has been demonstrated successfully by the works of Deville (2013), Zhang et al. (2013), Gutiérrez et al. (2008) and Wegst et al. (2010) in the field of freeze-casting, otherwise termed as ice-templating or ice segregation induced self-assembly of *colloidal suspensions*. Colloids are mixtures in which microscopic insoluble particles are suspended throughout the volume of a liquid medium (Bergstrom, 2001). This material processing method uses phase separation and ice crystal growth for controlling the microstructural features of a wide range of materials.

Although ice-templating does not mimic a biological process, the result can be very similar to some structures found in nature. It comprises the following steps: initially, a slurry is prepared that consists of a suspension of ceramic particles in a freezing medium (e.g. water, camphene, tert-butyl alcohol etc.) mixed with a dispersant and a binder. The slurry is then poured into a mould between two copper cold fingers. Its cooling rate is regulated by heating elements wrapped around each cold finger. A typical setup can be seen in Fig. 2.15. As the slurry freezes, the particles are expelled from the moving solidification (freezing) front and accumulate between the growing ice crystals. A schematic diagram of this process is illustrated in Fig. 2.16. Consecutively, the frozen sample is lyophilised

(freeze-dried) to sublimate the freezing medium, leaving behind a highly porous structure. The morphology of its pores, as can be observed in Fig. 2.15, may vary between lamellar, cellular, dendritic or even prismatic (Porter et al., 2013). Finally, the dried green body can be sintered to consolidate the particles and infiltrated with a second phase (polymeric or metal) to increase its strength. The technique's simplicity, versatility, speed and low cost, coupled with the biocompatibility of the liquid phase, make it a highly attractive solution for bio-inspired hard tissue substitutes (Deville, 2010).

Fig. 2.15. Left: Ice-templating setup with a single cold finger (Source: Wegst et al. 2010), right: Pore morphologies obtained after sublimation of the freezing vehicle (Source: Deville 2013).

Fig. 2.16. Phase diagram of water (left) and the mechanism of self-assembly in
Ice-Templating (Source: Deville 2013).

With ice-templating a large range of microstructure formations can emerge by
controlling the following parameters:

- The freezing-front velocity is perhaps the most important operational
  condition. It is determined by the cooling rate of the sample. It has been
  observed that lamellar wall spacing and average pore size increases with
  decreasing cooling rate. The presence of large temperature gradients
  hinders ice crystal growth.

- Addition of dispersants, binders, pH and viscosity of the slurry.

- Thermal conductivity of constituents.

- The presence of additives such as gelatine, glycerol and sucrose can alter
  the shape, size and roughness of micropores.

- Concentration (solid loading) and size of particles. High solid loading
  decreases the global porosity of the sample, while finer particles can
  replicate the most intricate features of ice crystals (Wegst et al., 2010).

There are several examples of the successful application of freeze-casting in the development of scaffolds for bone tissue engineering: In a study conducted by Deville et al. (2006), ice-templated hydroxyapatite scaffolds with highly anisotropic lamellar microstructure exhibited exceptionally high compressive strengths of up to 145 MPa and stiffness of 10 GPa for 47% porosity (see Fig. 2.17). So far, these are some of the highest values reported in bibliography for scaffolds of similar composition. Zhang et al. (2013) used a similar process to fabricate scaffolds with a compressive strength of 2.4 MPa for 68% porosity, which corresponds to the lower values for trabecular bone tissue. However, the most remarkable demonstration of the technique's potential can be found in the field of technical ceramics: Munch et al. (2008) employed ice-templating followed by polymer infiltration to produce a Al_2O_3/PMMA composite structure with toughness that is more than 300 times that of aluminium oxide alone.

Fig. 2.17. Left: Comparison of compressive strengths between an ice-templated HA scaffold with anisotropic microstructure and other porous HA scaffolds reviewed in Deville et al. (2013), right: Cross-section of porous alumina exhibiting lamellar microstructure (Source: Deville et al. 2007).

Ice-templated polymer/ceramic composites achieve superior mechanical performance by mimicking toughening mechanisms that exist in biological

materials. Fig. 2.18. illustrates the so-called extrinsic mechanisms observed in bone tissue, which act once a crack is formed to restrict its growth. More specifically, the hard mineral phase of these composites is structured at microscopic length scales and interfaced with a ductile polymer. Low cooling rates give highly anisotropic structures that can withstand very high loads along the axis of ice-crystal growth. A good example of this is the ice-templated alumina depicted in Fig. 2.19: the roughness of its lamellae together with the ceramic bridges connecting them can further enhance a composite's fracture resistance. The infiltrated polymer prevents crack propagation by bridging fracture surfaces and allows for controlled sliding between plates (Wegst et al., 2014). This way, the material no longer fractures in a sudden and brittle manner, but experiences plastic deformation before failing under compression (Fu et al., 2013).

Fig. 2.18. Extrinsic toughening mechanisms in bone tissue (Source: Launey et al. 2010).

Fig. 2.19. Left: Bridges in freeze-cast alumina scaffold
(highlighted with circles), scale bar: 50 µm (Source: Launey et al. 2009),
right: Toughening mechanisms in lamellar composites (Source: Wegst et al. 2014).

2.5. Low-Temperature Deposition Modelling

Despite the effectiveness of Ice-Templating in generating micro-features, it has certain limitations. The most substantial is the inability to create large structures because heat transfer diminishes as the thickness of the sample increases and it becomes difficult to maintain uniform temperature profiles (Deville, 2013). Another drawback is the inability to introduce meso-scale features, such as networks of interconnected channels, and to control the overall shape of a freeze-cast object without any post-processing. An alternative approach could involve freezing ceramic hydrocolloid suspensions in an additive manner. The concept of Robocasting in sub-zero temperatures is not new: Low-temperature Deposition Modelling (LDM), otherwise termed Freeze-form Extrusion Fabrication or Rapid Freeze Prototyping, involves extruding an aqueous based ceramic paste or polymeric hydrogel along predefined paths in an ambient temperature that is below 0°C. The solidification of the material after the deposition of each layer enables large parts to be built without the need for organic binders (Huang et al.,

2009; Leu et al., 2000). This particular feature together with the possibility of preserving bioactive substances, since no heating or melting is required, makes LDM highly suitable for tissue engineering applications. Xiong et al. (2002) have successfully demonstrated this by fabricating TCP/Poly(L-lactic) acid (PLLA) scaffolds of 89.6% average porosity. The scaffolds, besides their interconnected macroporosity, also exhibited micropores with an average size of 5 µm. Dorj et al. (2012) employed LDM to produce chitosan/nano-bioactive glass scaffolds with dual-pore structure, which displayed satisfactory cell adherence and proliferation. A team in Nanyang Technological University has used LDM to fabricate hierarchical scaffolds composed of chitosan (Pham et al., 2008). One of the latest advancements in this particular technique has been the use of multiple dispensing nozzles of various designs for building heterogeneous scaffolds (Billiet et al., 2012). Other advantages include the low cost of equipment and the ability to produce structures with compositional gradients (Guo and Leu, 2013). For example, a triple-extruder mechanism for producing parts with graded compositions between alumina and zirconia was recently developed in the Missouri University of Science and Technology (Leu et al., 2012). A disadvantage of this technique is that freeze-drying is required in order to remove the solvent. This can be time and energy-consuming depending on the volume and density of the printed parts.

Fig. 2.20. Close-up of hierarchical chitosan scaffold fabricated with Rapid Freeze Prototyping. The image on the right offers a closer view of its microstructural features (Source: Pham et al. 2008).

The full potential of LDM in the field of technical and biocompatible ceramic materials has not yet been realised. So far, research has focused on the production of dense ceramic structures (Huang et al., 2009), while neglecting one of the core strengths of the particular technique: the ability to control the microstructural features within a part. Pham et al. (2008) and Lim et al. (2008) have reported on the effect of freezing rate on the size and orientation of micropores within scaffolds made from chitosan (presented in Fig. 2.20). It was observed that low freezing rates resulted in large pores that were perpendicular to the direction of the dispensed path, orientated along temperature gradients. It is hypothesised that the same applies to aqueous calcium phosphate pastes but a series of experiments is required in order to understand how each processing parameter affects the microstructures that emerge during freezing.

2.6. LDM as a method for fabricating hierarchical scaffolds - objectives

The research presented in this thesis is the first systematic study of robocasting ice-templated bioceramic structures. A hybrid technique could open up new

possibilities for fabricating bioresorbable implants with tailorable bimodal porosity in a reproducible, quick and cost-effective way. It is important at this point to acknowledge that an extrusion-based AM technique cannot replicate the well-controlled unidirectional freezing that is achieved in Ice-templating. In LDM, the material freezes through an interplay between two main heat transfer mechanisms. Heat is conducted between a bead as it is being extruded and previously deposited layers, while convection takes place with the cooled air that surrounds it. Another major difference lies in the rheological characteristics of the suspensions that each technique is able to handle. Ice-Templating, as opposed to LDM, can handle any type of colloid, irrespective of its viscous properties. Consequently, this research explores the possibilities that may arise from a synthesis between the fields of AM and Ice-Templating, while recognising the limitations imposed by the inherently different nature of the proposed process.

To this end, the following questions will be considered:

- What is the shape, size, distribution and orientation of the pores created from ice crystal growth during the paste's solidification at different chamber temperatures?

- How does the solid loading of the paste affect the microstructures that emerge in LDM?

- What is the effect of a dispensing nozzle's temperature on the freezing rate of a calcium phosphate ceramic (CPC) paste, as it is being deposited at different speeds in sub-zero ambient temperatures?

In order to achieve the aforementioned objectives, it was necessary to develop a simple method for tailoring the viscoelastic properties of CPC pastes, as well as the appropriate dispensing system for thixotropic fluids. These are described in the chapter that follows.

Chapter 3

Development of bioceramic inks and Robocasting system

In order to investigate the potential of LDM in structuring bioceramic scaffolds at different orders of magnitude, it was necessary to develop beta-tricalcium phosphate (β-TCP) pastes of high water content with the appropriate rheological properties for robocasting. The dispensing system was designed in parallel, as the two mutually inform each other.

3.1. Material and Design Specifications

Both the material and dispensing system were designed according to certain requirements, dictated by the additive nature of the process and its operating conditions. More specifically, the print paste must be injectable through submillimetre nozzles, whilst at the same time capable of retaining its extruded shape, even as it spans over gaps (up to several millimetres) in previously deposited layers. It should also fuse upon contact with its underlying material to ensure geometrical accuracy. Injectability refers to the ability of a paste to retain its

homogeneity when subjected to pressure (Perez et al., 2012). In Ice-templating, a solid loading of 30% v/v typically results into sintered bodies with approximately 50% porosity (Deville et al., 2015). High solid content can hinder particle movement and redistribution, resulting in a dense and homogenous green body (Deville, 2008). For this reason, the ceramic paste used in this study ought to be formulated in such a way that its reduced solid to water ratio (SWR) has limited impact on its printability. Furthermore, it is essential that the particles in suspension do not sediment under gravity when the material is at rest. Additionally, the print-head should prevent the contained paste from freezing throughout the printing process, while enabling the regulation of the material's temperature as it is being deposited. Another important element is the software used for generating the overall geometry of the scaffold and the corresponding tool-path for its fabrication; a highly desirable feature for tissue engineering applications would be the ability to alter various material and processing parameters during the course of printing to introduce compositional and functional gradients.

3.2. Tailoring the viscoelastic properties of colloidal β-TCP pastes for AM.

In this study β-tricalcium phosphate (β-TCP) was selected due to the low cost of the raw material, its advantageous biological properties (see Section 1.2.2) and its cell-mediated mechanism of resorption in vivo (Perera et al., 2010). As mentioned above, the rheological characteristics of a colloid suspension in Ice-Templating are not of primary importance. The same does not apply to Robocasting techniques, where a particular viscoelastic response is required. One of the main strategies for controlling the rheological behaviour of ceramic slurries is through tuning their pH

and consequently the magnitude of attraction or repulsion between the particles. Lewis (2006) has reported on the use of polyethylenimine (PEI), a cationic dispersant, in a number of different ceramic suspensions. A fine control of the degree of coagulation in such ceramic slurries was achieved through altering their pH or adding salts or negatively charged polyelectrolytes. However, the solubility of calcium phosphates (CaP) in particular, is sensitive to changes in the pH, which necessitates a different approach. An alternative method uses polymeric additives to coat the particles and regulate the colloid's viscoelasticity by altering the average thickness of the adsorbed polymer layer, its affinity to the particle's surface and/or its solubility in the liquid medium (Bergstrom, 2001). This constitutes a versatile way of tailoring the rheological properties of a wide range of ceramic materials in a single step. A good example is the use of a non-ionic co-polymer, Pluronic F-127®, to prepare calcium phosphate (Franco et al., 2010) and bioglass (Fu et al., 2011b) slurries for robocasting. The polymeric additive can also act as a binder for producing strong green bodies in order to minimise possible shape distortions during handling. In a study conducted by Wu et al. (2011), a polyvinyl alcohol (PVA) polymer solution was mixed with mesoporous bioglass powder to produce tough bioresorbable scaffolds that do not require a sintering stage. Moreover, highly volatile solvents can also be employed so that the ceramic slurry sets almost immediately after its deposition. For instance, in the field of technical ceramics, fast setting alumina pastes have been prepared by dissolving polyvinyl butyral (PVB) and polyethylene glycol (PEG) in propan-2-ol (X. Lu et al., 2010). The above strategies are not solely limited to synthetic polymers. Carboxylmethyl cellulose (CMC) has been used both as a dispersant and an additive in 45S5 bioglass

formulations (Eqtesadi et al., 2014), while gelatin has been combined with α-TCP to form a self-setting paste that hydrolyses into hydroxyapatite. This way, not only are its rheological properties improved but also the chemical composition of bone tissue can be mimicked (Maazouz et al., 2014).

Other parameters that influence the flow behaviour of colloidal pastes are the volume fraction of the colloid, average particle size and shape, as well as the stress applied (Conrad et al., 2011). High viscosity is necessary, but it can pose a problem when a sub-millimetre wide orifice is used. For this reason, viscosity should decrease when the material is subjected to shear (i.e. when it flows through a narrow nozzle). A concentrated suspension usually exhibits shear thinning behaviour after exceeding a certain level of stress, termed yield stress (σ_y). At that point, it transitions from a "solid" to a "liquid" state, as its gelled structure gets broken down into small units that slide past each other, called flocs. This plastic behaviour is less prominent for dilute suspensions. Higher shear rates can further reduce the size of the flocs, facilitating flow (Barnes, 1997; Bergstrom, 2001).

Fig. 3.1. Schematic representation of a thixotropic structure's breakdown (Source: Barnes 1997).

In Robocasting, it is essential that this flocculation be reversible and that the material recovers its original microstructure after shearing stops. A rapid recovery of elasticity allows free-spanning filaments to bridge gaps in underlying layers with minimal sagging. The term used for this rheological behaviour is thixotropy. It is a time-dependent property, since thixotropic materials do not respond instantly to changes in shear rate. A certain amount of time is required for them to reach equilibrium viscosity that can range from seconds to several days. High thixotropy is a desirable property when Robocasting with ceramic slurries (Li et al., 2006). Also, an advantageous property of such complex fluids is the formation of a thin solvent-rich layer adjacent to the deposition nozzle's walls that facilitates the extrusion process due to slippage. Therefore, at low extrusion rates, the filament's core experiences minimal shearing stress and breakdown, which further enhances its elastic properties (Zhu and Smay, 2010). Below the development of a novel β-TCP

formulation with highly thixotropic behaviour is described, resulting from the combination of sodium alginate and xanthan gum polymeric additives.

3.2.1. Materials

Sodium alginate (SA) is the sodium salt of alginic acid, a polysaccharide extracted from the cell walls of brown algae. It has been used extensively in the food, pharmaceutical and textile industries amongst many others. One of the first injectable calcium phosphate formulations, developed in the late 1980's, consists of SA mixed with β-TCP granules (Bohner, 2010b). SA crosslinks in the presence of Ca^{2+} ions, as demonstrated in Fig. 3.2, to form a rigid polymer network with a structure resembling that of an "egg box" (Lee and Mooney, 2012).

Fig. 3.2. Guluronate blocks assemble into an egg-box-like structure with Ca^{2+} ions in its interstices (Source: Lee & Mooney 2012).

Xanthan gum (XG) is a polysaccharide secreted by the bacteria Xanthomonas Campestris that is widely used as a thickening agent and stabiliser (Garcia-Ochoa et al., 2000). A small addition of XG is known to improve the injectability and cohesion of calcium phosphate pastes (Bohner and Baroud, 2005) (Boher et al., 2006). In the field of textile printing, Wang et al. (2013) reported that xanthan-

based reactive dye pastes exhibit elastic properties, a weak-gel characteristic and a transition from elasticity to viscosity when subjected to shear. The same group also established that the addition of small amounts of XG to SA-based printing pastes results in significant shear-thinning behaviour and intensifies their solid-like features (Wang et al., 2014). Owing to its weak-gel-like properties, XG can be mixed with different types of gelling agents to form strong elastic gels. Its synergy with glucomannans, such as locust bean and guar gums has been studied extensively (Goycoolea et al., 1995). Of particular interest is the ability to control the viscoelastic properties of the resulting gel through the weight ratio of its constituent hydrocolloids in the bi-phasic mixture. This chapter evidences for the first time the synergistic use of XG and SA in the preparation of printable bio-ceramic pastes.

β-TCP powder was used unprocessed, as supplied by Sigma Aldrich. SEM images of dried samples showed particles with irregular shape and sharp edges that range between 1 and 5 μm (see Fig. 3.3). Food grade Sodium Alginate and Xanthan Gum were supplied by Special Ingredients Ltd.
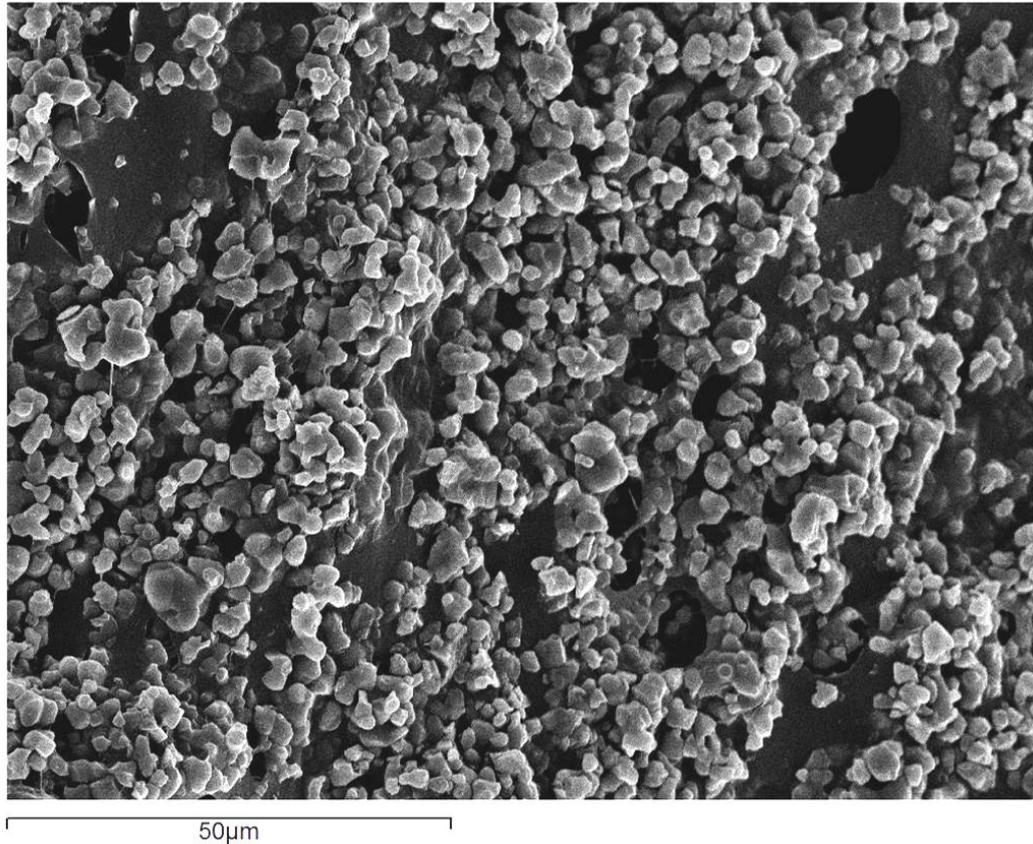
Fig. 3.3. SEM micrograph of a freeze-dried sample of β-TCP paste, showing particles of irregular shape with sharp edges and size varying between 1 and 5 μm.

3.2.2. Preparation

Initially, the effect of each polymeric additive on the rheological behaviour of aqueous β-TCP pastes was investigated in isolation. A series of samples with 50 and 40% by weight solids were prepared, containing different amounts of SA and XG that ranged between 0.4 and 2% w/w. The components were manually mixed in their dry form with a mortar and pestle, followed by the addition of distilled water. The mixture was homogenised through vigorous stirring for 2-3 minutes. Subsequently, the paste was sieved through a 62 μm mesh to break down any agglomerates present. The rheology of formulations where both polymeric species are present was studied using a mixture of 39.5% β-TCP, 4% SA, 1.2% XG and 55.3%

H$_2$O (w/w). This particular paste composition was developed empirically and demonstrated good injectability and shape retention after deposition.

3.2.3. Methods

The viscoelastic properties of the prepared paste samples were investigated with a rotational rheometer. A parallel plate rheometer consists of two plates separated by a specified clearance of height h, which is filled with the liquid to be tested. Unlike the cone and plate geometry, this distance can be varied, allowing for pastes of high viscosity that contain large particles and/or aggregates to be tested. The bottom disc remains stationary, while the other revolves around their shared axis. The device has two main modes of operation:

a) A controlled stress (σ) is applied while measuring the rate at which the fluid is sheared (γ).

b) Alternatively, the stress required in order to produce a controlled shear rate can be measured.

A disadvantage of the particular geometry is that the specimen does not experience the same shear rate throughout its volume, which impacts on measurement accuracy. More specifically, shear rate is virtually zero at the centre and attains a maximum value at the edge of the disc. To compensate for errors, appropriate corrections can be applied (e.g. Weissenberg and Rabinowitsch analysis) (Schramm, 1994). However, useful conclusions can be drawn, from a qualitative point of view, without such high degree of accuracy. A full list of equations for calculating the rheological quantities in parallel plate rheometry can be found in Schramm (1994). The reader can refer to J. Mewis & Wagner (2011)

and Coussot (2005) for information regarding some of the most characteristic tests employed in paste rheometry, as well as phenomena that can impact on instrument readings.

The first series of tests was performed with a CSL^{2}100 Carri-Med rheometer (TA Instruments) and a 40 mm diameter plate geometry. The clearance h between the plates was set at 500 μm and the temperature was maintained at 20°C. Each specimen was subjected to an increasing-decreasing stress ramp test, conducted as follows: initially, the stress applied to the paste was increased incrementally to a maximum value. Immediately after, it was gradually reduced back to its original value. Strain measurements were acquired throughout this process, from which viscosity (η) values were deduced. This constitutes a practical method not only for characterising the flow behaviour of a fluid but also determining time-dependent properties, such as thixotropy.

The rheological properties of the CaP formulation that contains both SA and XG were examined with a Discovery Hybrid Rheometer (DHR-1/TA instruments). A 20 mm diameter disc geometry was positioned 1500 μm above the device's Peltier plate, the temperature of which was set at 20°C. In this case, dynamic (oscillatory) tests were preferable over steady-state shear flow tests due to significant shear banding, observed even at low shear rates. Olmsted (2008) has given the following definition for this phenomenon:

"When an imposed shear rate exceeds a characteristic structural relaxation time, the fluid can attain a non-equilibrium state in which "shear bands" of fluids with

different apparent viscosities coexist, separated along the flow and having the same

shear stress".
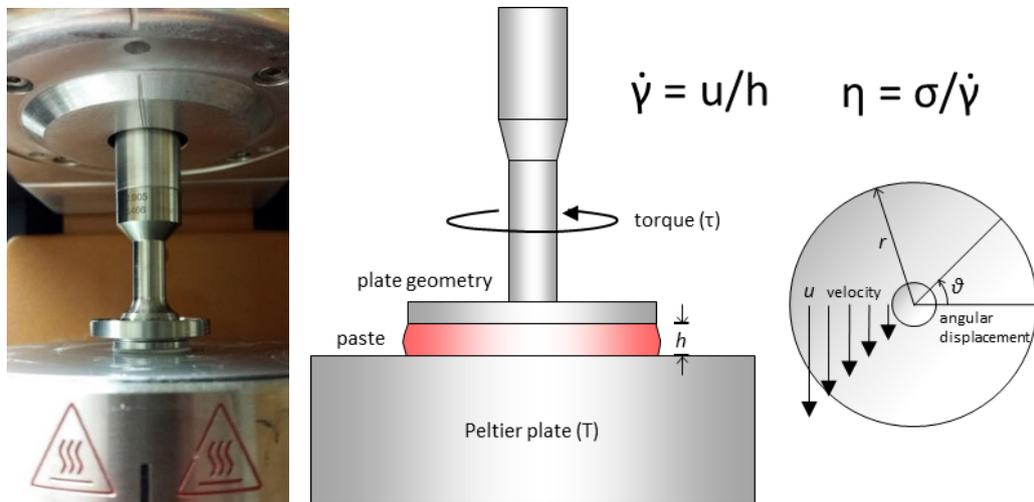
Fig 3.4. Left: Parallel plate rheometer, right: Schematic diagram and operation of a rotational rheometer. Note the non-uniform shear rate resulting from the constant thickness of the fluid sample.

Oscillatory tests provide information on viscosity and elasticity without disturbing mechanically or rupturing the specimen's structure. This is due to the fact that the rotor instead of turning continuously in one direction, deflects with a sinusoidal time-function of specific frequency clockwise and anti-clockwise. The material develops internal forces that resist deformation, experiencing strain or stress that follows a similar wave pattern. The amplitude and phase shift angle of this response is characteristic of the material (Schramm, 1994). If stress (strain) is in phase with the applied sinusoidal strain (stress), the material is considered an ideal elastic solid. On the contrary, if the two curves are out of phase (phase angle of $\delta=\pi/2$), the material behaves like a purely viscous fluid (see figure below).

Fig. 3.5. Stress–time curve for a pasty material under oscillating strain:
(a) solid regime; (b) liquid regime (Source: Coussot 2005).

The following three procedures were performed:

- The paste sample was subjected to increasing levels of oscillating stress (amplitude sweep) ranging from 500 to 8000 µN·m with an angular frequency (or speed) of 10 rad/s. This test assisted in determining the material's linear viscoelastic region (LVR), where stiffness remains practically constant irrespective of the magnitude of applied stress.

- The recovery rate of viscosity after shearing was assessed with an oscillatory three-step thixotropy test. More specifically, the applied torque was stepped from low (1000 µN·m) to high (4000 µN·m) and back to low at a constant angular velocity of 10 rad/s. The duration of each step was 60 s and measurements of storage and loss modulus were acquired at 5 s intervals. This test simulated, to a certain degree, the shear stress that the paste experiences at the onset of extrusion as it travels through a nozzle's outlet. The last step of the sequence corresponds to the filament's relaxation after it has been deposited.

3.2.4. Results

Stress ramp tests of SA-based TCP pastes revealed a shear thinning behaviour that was more pronounced at high solid loading and SA content, as can be seen in Fig. 3.6. Specimens with 2% (w/w) SA displayed viscosity that was two orders of magnitude higher than those containing 0.4% SA.
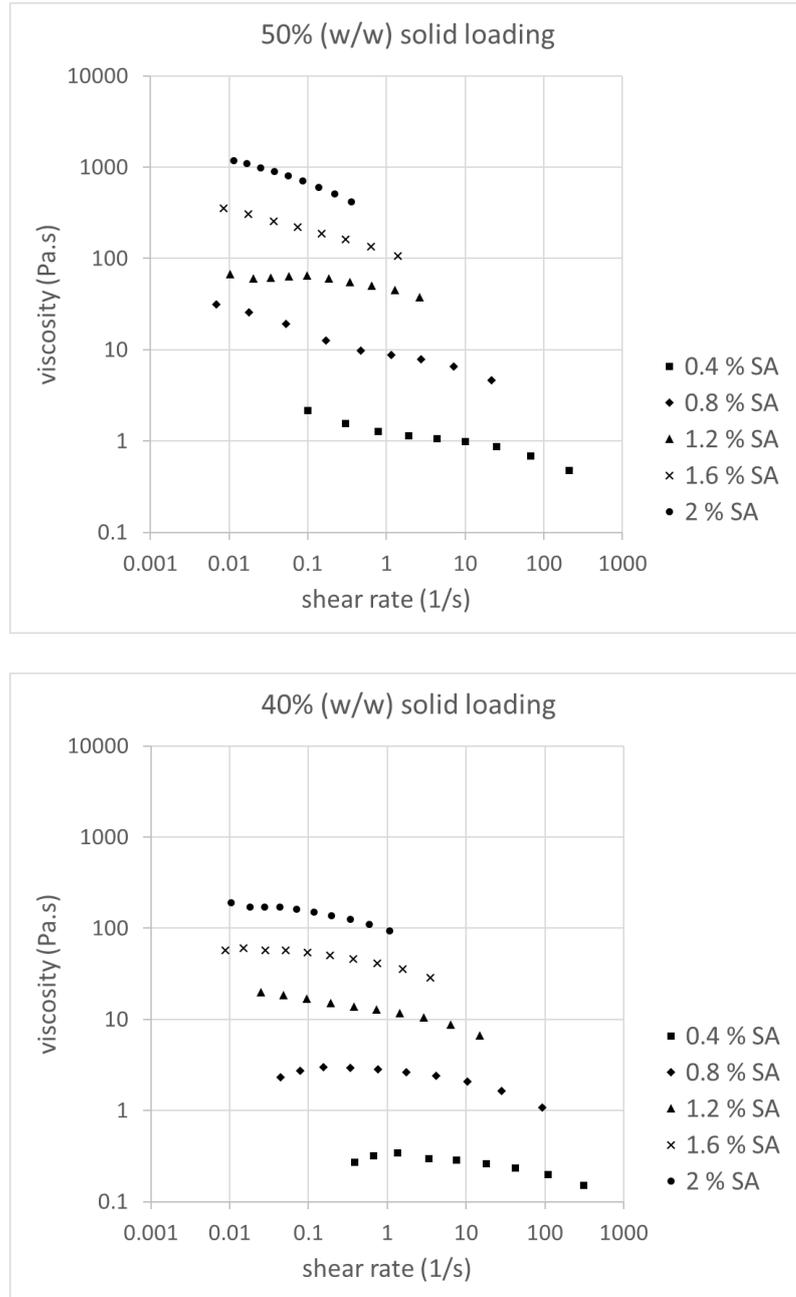
Fig. 3.6. Graphs of viscosity vs shear rate for paste specimens containing 50 (top) and 40% (w/w) solids (bottom) and varying amounts of SA (data obtained from increasing stress ramp tests).

However, the addition of SA did not impart thixotropy, which is a major requirement for filament-based additive manufacturing. This was deduced from stress-strain graphs, similar to the one shown in Fig. 3.7. The curves that correspond to the ascending (blue) and descending (red) stress ramp appear to coincide, which suggests a time-independent flow behaviour.
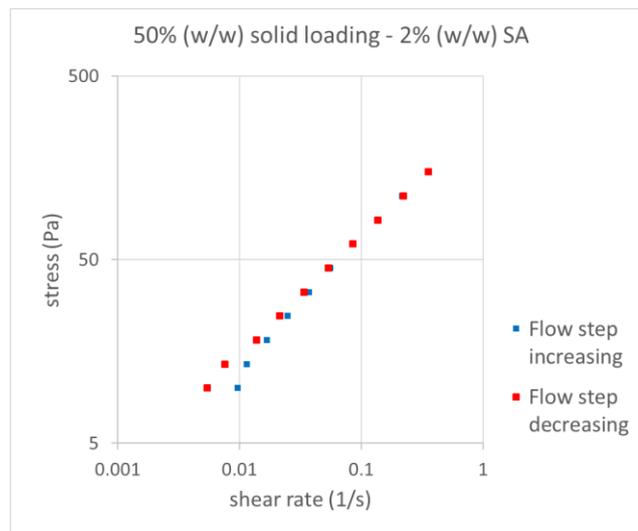
Fig. 3.7. Plot of stress vs shear rate for a sample consisting of 50% (w/w) solids and 2% (w/w) SA.

In contrast, β-TCP slurries containing XG demonstrated a thixotropic behaviour. This observation is confirmed by the characteristic hysteresis loop of the graph in Fig. 3.8 (Jan Mewis and Wagner, 2011). Thixotropy was also responsible for the significant impact of shear history on viscosity measurements. Fig 3.9 shows that the shape of a stress-shear rate curve for a pre-sheared specimen can be very different from its non-agitated counterpart. This is more evident in the ascending portion of the curve. At a given stress value, the former flows more easily due to the partial breakdown of its microstructure. At higher levels of shear stress, the two curves gradually converge as viscosity reached steady state.
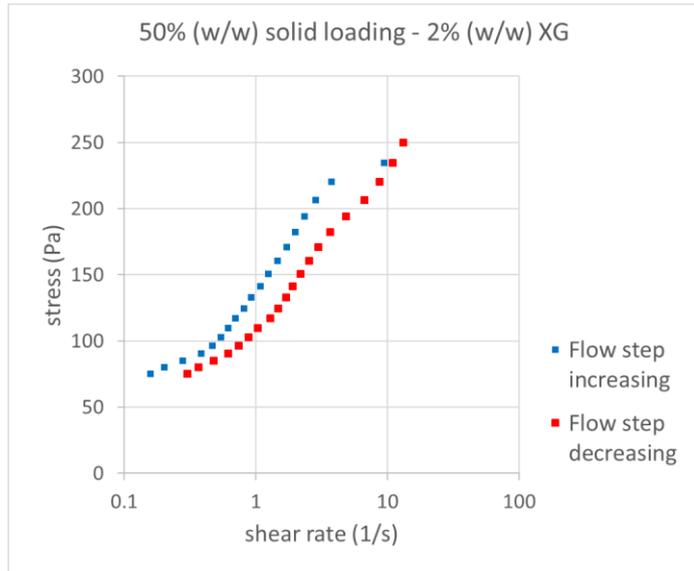
Fig 3.8. Plot of stress vs shear rate for a sample consisting of 50% (w/w) solids and 2% (w/w) XG demonstrating a hysteresis loop.
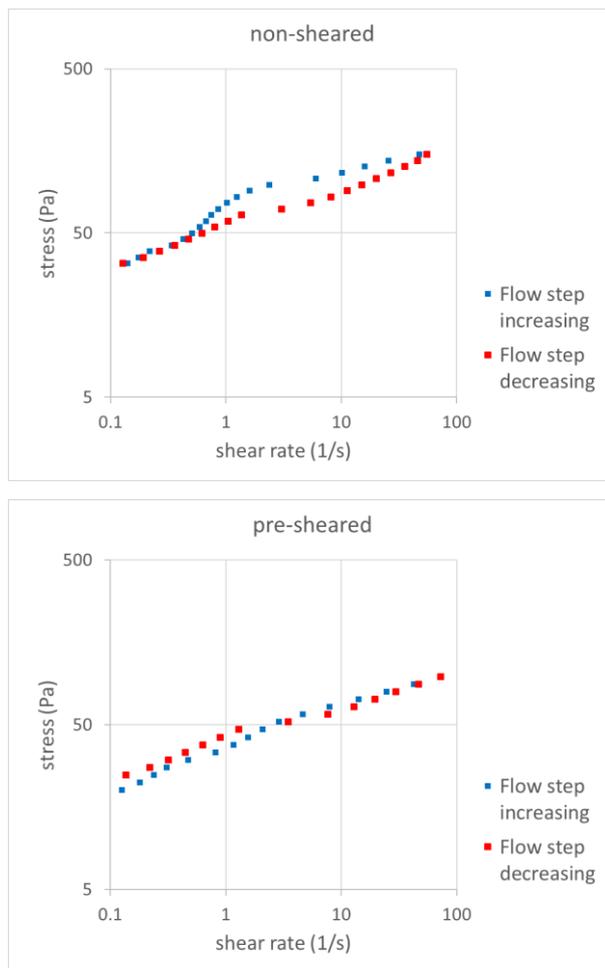
Fig. 3.9. Stress-shear rate diagrams for non-sheared (top) vs pre-sheared (bottom) paste samples of identical composition (1.2% XG, 50% solids).

In comparison to SA, the addition of XG to TCP slurries imparted significant shear thinning behaviour; for example, viscosity dropped by four orders of magnitude when a sample with 40% solid loading and 0.4% XG was sheared at a rate of 10^3 s^{-1} (see Fig. 3.10). Also, a tighter distribution of points along the dashed red lines can be noticed in both graphs. This suggests that variations in the mass fraction of TCP and polymeric additive result in smaller changes in paste rheology when substituting SA with XG. At a given shear rate, viscosity values spanned two orders of magnitude as opposed to three in SA-based pastes.
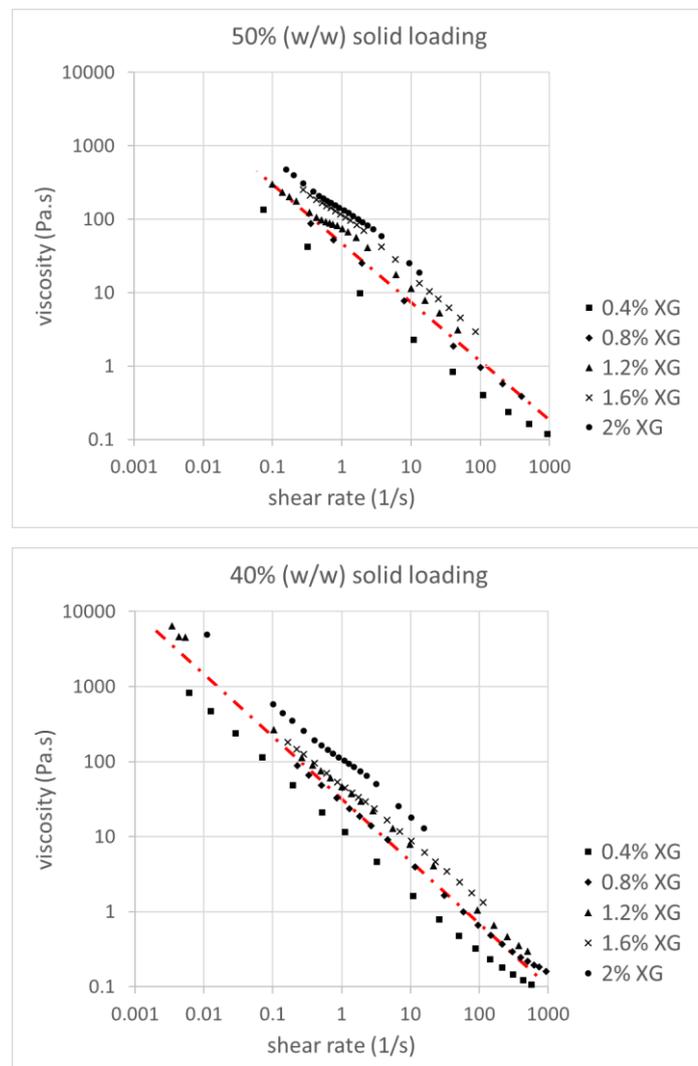
Fig. 3.10. Viscosity-shear rate diagrams of paste samples containing 50 (top) and 40 % solids (w/w) (bottom) and varying amounts of XG (data obtained from increasing stress ramp tests).

From a practical point of view, XG-based pastes exhibited a "stringy" consistency owing to their high elasticity, which was evident even in dilute suspensions. This ability to flow without fracture can be seen in Figure 3.11, where a lump of material is being lifted off a mortar. At high concentrations, the formulation became "sticky", while maintaining the rheological behaviour of a weak gel. Despite its favourable shear-thinning properties and excellent particle suspension stability, xanthan gum is characterised by a slow recovery of viscosity after agitation (long relaxation times) (Song et al., 2006). As a result, when a filament of such composition gets deposited, it experiences initially significant deformation under gravity until its microstructure is rebuilt. For this reason, it was concluded that β-TCP pastes prepared with XG alone do not display the desirable rheological features for deposition modelling.

Fig. 3.11. Consistency of XG-based TCP paste (2% w/w and 50% solids).

The formulation containing both types of polymeric additives behaved in a radically different way when sheared. Early observations, by means of physical manipulation and extrusion tests (see Fig. 3.12), suggested a soft elastic putty with good workability, injectability and cohesion. Dynamic tests revealed a shear thinning behaviour with a rapid recovery of viscosity after shear. More specifically, at an angular frequency of 10 rad/s the yield stress of the mixture was estimated at approximately 500 µN·m, as evidenced in Fig 3.13. This value marks the end of the material's linear viscoelastic region (LVR), beyond which its viscoelastic structure begins to break down. Within the LVR, viscosity is practically independent of the applied torque (horizontal portion of the G' curve). The diagram also illustrates the steep reduction in storage modulus (G') by two orders of magnitude, as the applied torque increases from 500 to 8000 µN·m. A viscous, more fluid-like response (G") becomes dominant above 3000 µN·m.

Fig. 3.12. Extrusion of XG-SA-TCP paste through a 1.6 mm nozzle.
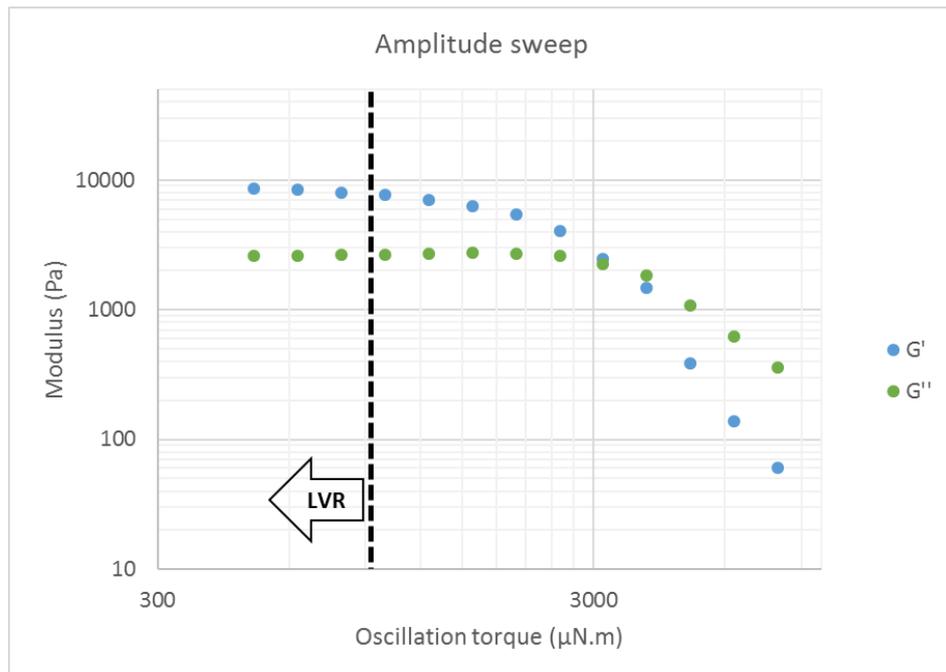
Fig. 3.13. Storage (G') and loss (G'') modulus plotted against oscillation torque as obtained by amplitude sweep test and determination of LVR.

The oscillatory three-step thixotropy test, presented in Fig 3.14, shows that a sudden increase in oscillation torque can impart an almost instant transition from an elasticity to a viscosity-dominated regime. After reducing the shear stress back to 1000 µN.m at an elapsed time of 120s, the structure of the paste rebuilds very rapidly. It was observed that it takes less than 20 s for viscosity to reach approximately 90% of its original value. This feature is particularly advantageous in robocasting (see Section 3.2). This bi-phasic polymer blend can also be used with other types of bio-ceramic materials. For example, TCP could be partially or entirely replaced with Hydroxyapatite or Bioglass^{TM}. It has the disadvantage, however, of high water solubility due to the presence of XG, which contains anionic side chains. A sintering stage is required to densify the ceramic matrix and obtain a scaffold that can retain sufficient mechanical strength after its implantation or immersion in a bioreactor for cell culture.
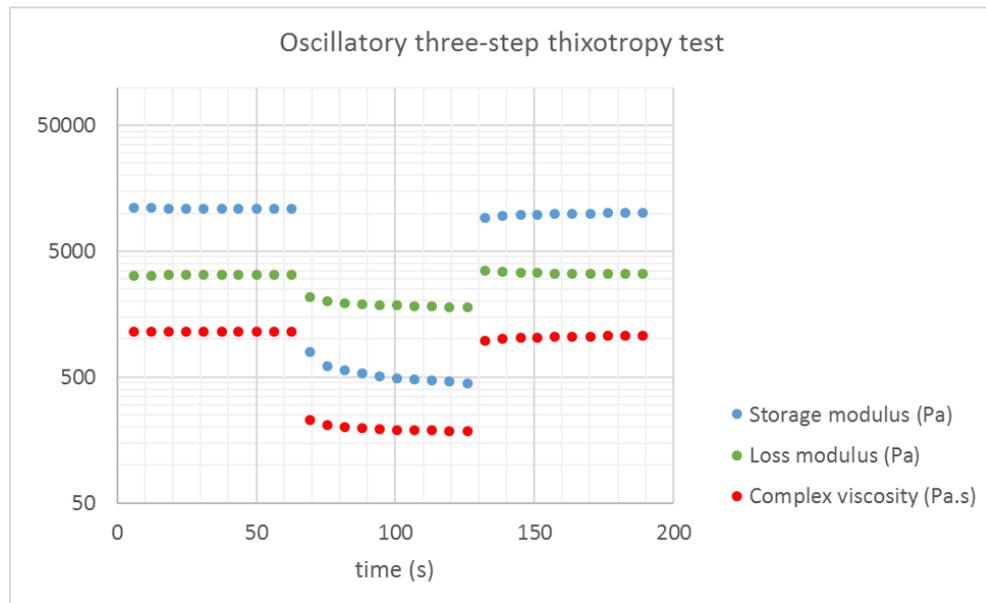
Fig. 3.14. Oscillatory three-step thixotropy test (oscillation torque: 1000 → 4000 → 1000 µN·m).

3.3. Development of additive manufacturing tool

A commercial Fused Deposition Modelling (FDM) 3D printer (BFB-3000) was modified to accommodate the extrusion of colloidal β-TCP pastes. The modification involved replacing the polymer extruder with a pressure-driven dispensing system. Several iterations were performed in order to produce a simple and economical design that offers high precision and repeatability. These were informed by well-established dispensing techniques for highly viscous materials. The paragraphs that follow discuss the advantages and drawbacks of each system:

3.3.1. Time-pressure system

Initially, a time-pressure dispensing system was used, in which a plunger was actuated by pressurised air to drive material out of a syringe barrel. A solenoid valve was employed for starting and stopping the extrusion process. This design, despite its simplicity and ease of maintaining, suffered from serious drawbacks. A

significant delay of several seconds was observed at the end of dispensing cycles due to the thixotropy of the paste and compressibility of air. As the volume of paste inside the syringe barrel was reduced, the extrusion rate gradually increased due to smaller resistance to flow. Also, the time required for pressure to reach the set value would become longer, as more air was required to fill the empty space above the material. Decompressing the barrel at the end of a cycle, with the help of a release valve, improved to some extent the system's responsiveness. It did not address, however, the issue of inconsistent volumetric flow rate.

3.3.2. Syringe-pump system

In the second iteration, a syringe-pump mechanism was employed to control the extrusion through a 500µm diameter heated nozzle. The design was inspired by Fab@Home's syringe extrusion tool (refer to Chapter 2). The print-head consisted of a motor-driven lead screw which acted as a ram for pre-filled syringe barrels. The lead screw was actuated indirectly through a 500:1 planetary gear-box to allow for accurate control of the plunger's position and speed (see Fig. 3.15). Its performance was initially evaluated by dispensing water droplets at different ram velocities along straight paths. As can be seen in Fig. 3.16, the unit successfully deposited equidistant droplets of identical volume.
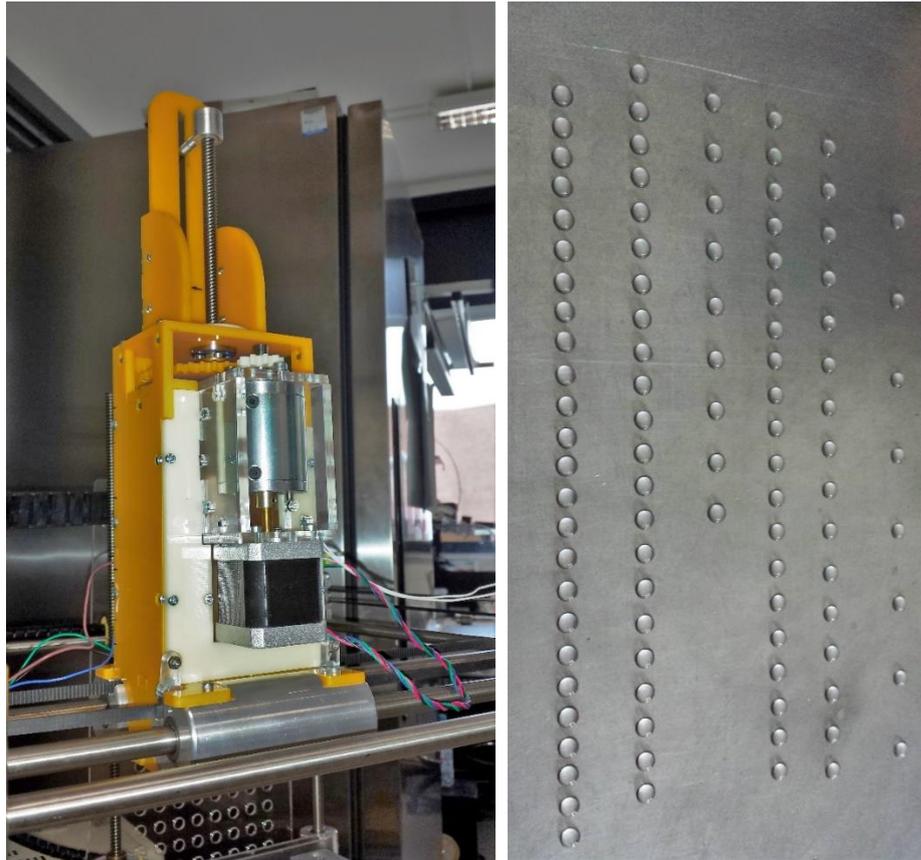
Fig. 3.15. Syringe-pump system (left) and water droplet dispensing test (right).

When extruding paste at a constant ram velocity, however, an inconsistency of flow rate was observed. The print-head would initiate flow with considerable delay (of several seconds) and fail to stop at the end of a dispensing cycle. The reason for this behaviour predominantly lies in the thixotropic nature of the extrudate. A variation in ram velocity would therefore be required to regulate the shear forces that the paste is subjected to. More specifically, the ram should accelerate at the onset of extrusion until the paste exceeds its stress yield point and attains steady-state flow. A low and constant velocity can be maintained thereafter, until deposition is complete. It would also be necessary that the plunger retracts before the tool reaches the end of the deposition path, so as to minimise the tail effect (Li et al., 2015). This has been addressed in Freeze-form Extrusion Fabrication with a

force sensor (load cell) that measures in real time the pressure that is applied on the reservoir (Huang et al., 2006). Subsequently, it feeds back into the tool's controller, which regulates ram velocity to maintain a consistent flow. An alternative design uses linear DC servos, instead of stepper motors, to actuate the extrusion ram (Leu et al., 2011). The idea of implementing a real-time feedback control system was not pursued, as it entailed significant mechanical and electrical modifications that were unfeasible within the given time frame.

An additional factor affecting flow rate may also have been the presence of entrapped air within the paste, causing it to behave similarly to a compressible fluid. Degassing of the paste was not possible due to its high viscosity and a small volume of air is therefore always expected in the mixture.

3.3.3. Rotary auger valve dispensing system

In the latest configuration, the material is fed from a pressurized syringe into a disposable auger valve (see Fig 3.16). The valve (Techcon Systems DMP16-10) consists of a rotating helical screw (rotor), fitted inside a cylindrical housing (stator). The screw is 16 mm long with 16 threads-per-inch (TPI) and is made from high density Delrin®. A similar dispensing system has been used by *Unfold* studio (see Section 2.1.4), offering a high level of control over the extrusion process.
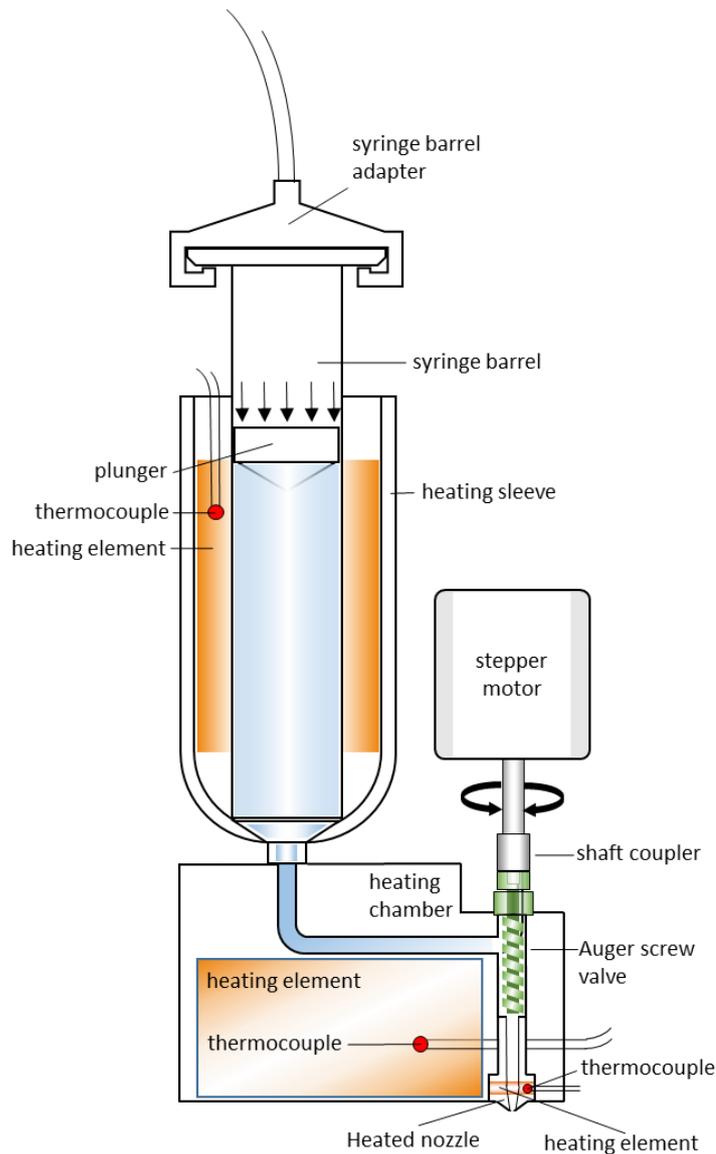
Fig. 3.16. Schematic diagram of dispensing system with motor-driven auger valve.

A constant air pressure of 5 bar was maintained in a 55 cm^3 syringe barrel to ensure a continuous supply of material into the valve. The barrel was placed inside a polypropylene tube (40 mm internal diameter) wrapped in 6 mm of Nitrile Rubber Foam (NRF) thermal insulation. A 100×75 mm silicone heater mat (RS components, 12V, 7.5W) was positioned inside the tube to prevent the ceramic slurry from freezing during the system's operation. Its temperature was regulated by a digital temperature controller via a K-type thermocouple. The tube was sealed with pipe

lagging, which is fitted over the barrel after it has been filled, as shown in Fig. 3.17. To minimise the presence of air bubbles, it is recommended that the syringe be filled carefully from the bottom end.
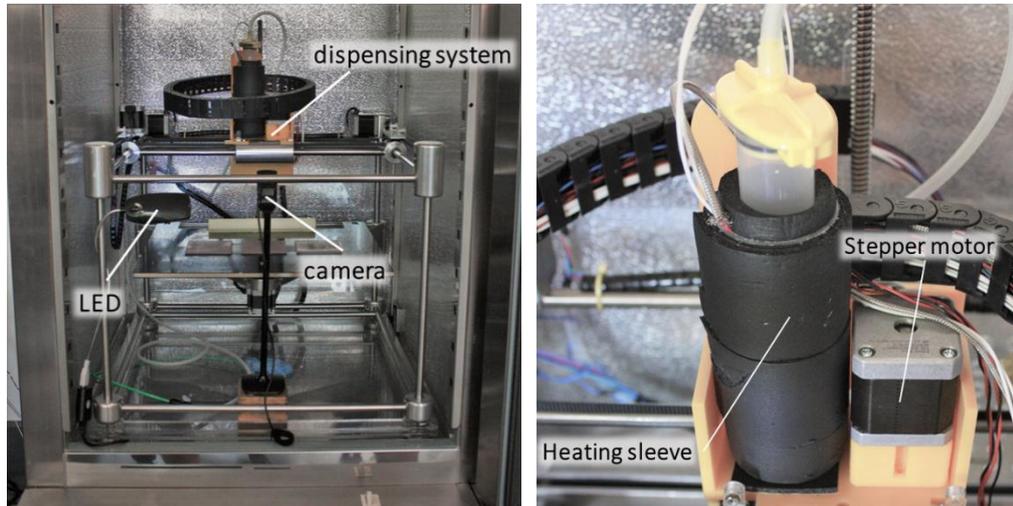
Fig. 3.17. Left: LDM setup, Right: material feeding section of the dispensing unit.

The screw was coupled with a stepper motor, driven by the 3D printer's control unit. A major advantage of auger valves is that their volumetric output is nearly proportional to the number of rotations. More precisely, it is determined by the pressure that builds up with every rotation, as more fluid accumulates inside the nozzle. The magnitude of shear stress that it experiences as it travels through the valve is dependent upon the geometry of the screw (i.e. pitch, thread depth and form) and its speed of rotation. This is particularly useful for thixotropic fluids, as it offers the ability to regulate the viscosity of a small volume each time, immediately before it reaches the outlet. Furthermore, it allows for reversing the direction of rotation in order to prevent the paste from dripping or tailing between dispensing cycles (*suck-back*). A disadvantage of the particular system was the extrusion's

pulsation; however, this was minimised by correcting the air pressure and/or the motor's RPM for a given printing speed.
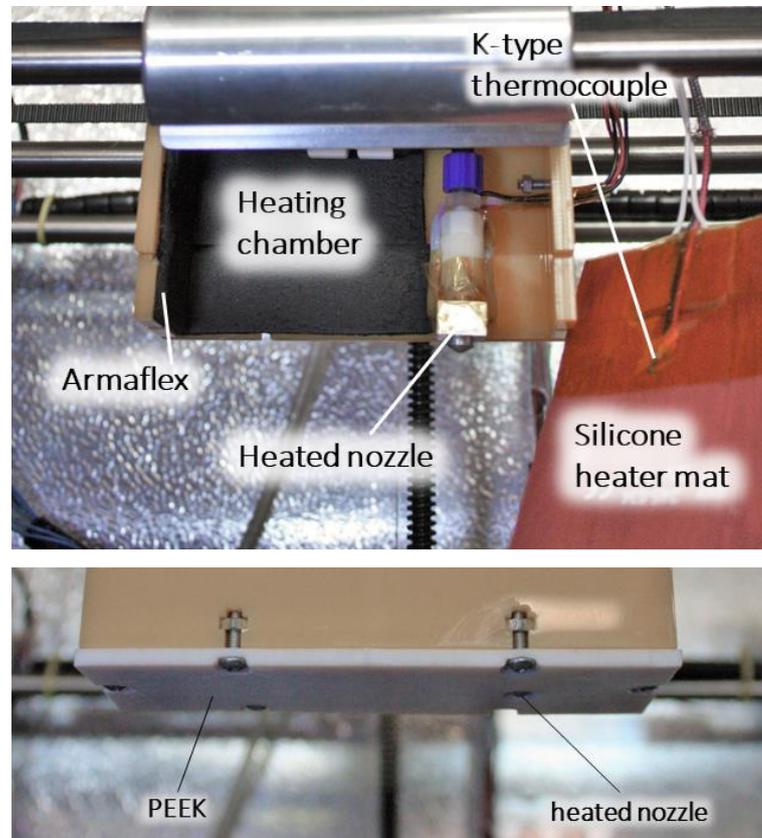
Fig. 3.18. Print-head configuration – lower section.

The valve, including the feed passage and heated nozzle, were encased within an acrylic box lined with 3 mm of NRF thermal insulation (Armaflex®) as demonstrated in Fig. 3.18. The box was assembled from laser-cut parts 5 mm in thickness (technical drawings can be found in Appendix A). An additional silicone heater mat was placed inside the casing. Standard luer-lock fittings were used for attaching the heated nozzle to the valve's outlet. The heated nozzle is a standard 0.5mm Rep Rap "J-Head" hot end, used extensively amongst the hobbyist 3D printing community for its simple and compact design (see Fig. 3.19). This component allowed to

control the temperature of the paste as it is being extruded. The bottom face of the casing was sealed with a 3 mm sheet of PEEK, which features a 7 mm diameter bore for the nozzle to pass through (see Fig. 3.18).
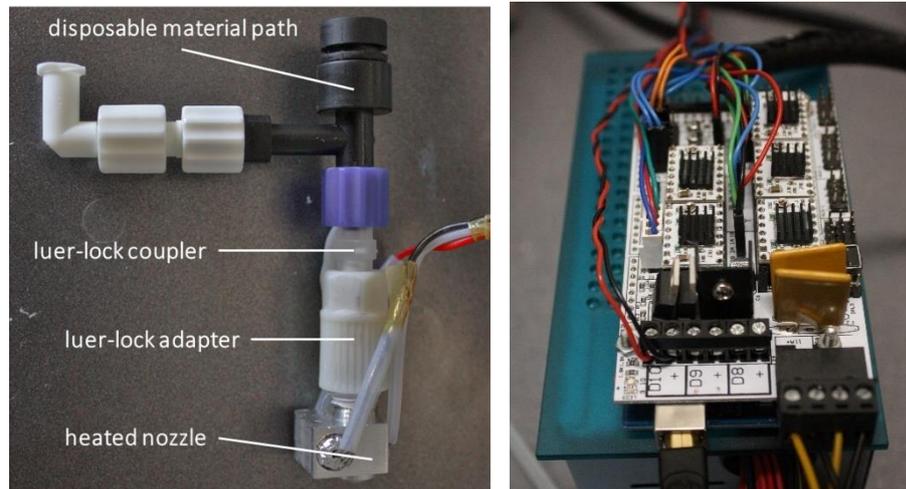
Fig. 3.19. Left: DMP and J-Head hot end assembly, Right: RAMPS 1.4 control unit.

The printer was controlled by a RAMPS 1.4 shield (ooznest.co.uk) mounted on an Arduino Mega 2560 programmable circuit board, shown in Fig. 3.19. Tool paths in G-code format were generated with the Grasshopper plugin for Rhinoceros (see Chapter 2).

The performance of the dispensing unit was assessed by weighing beads of three different nominal lengths (50, 100 and 200 mm), extruded at different nominal speeds ranging between 50 and 800 mm/min. The graph in Fig. 3.20 suggests that the mass corresponding to each nominal length is dependent on the set extrusion rate. For example, extruding 100 mm over of a period of 120 s increased the total

amount of material dispensed by 60% in comparison to extruding in $1/16^{th}$ of the time.
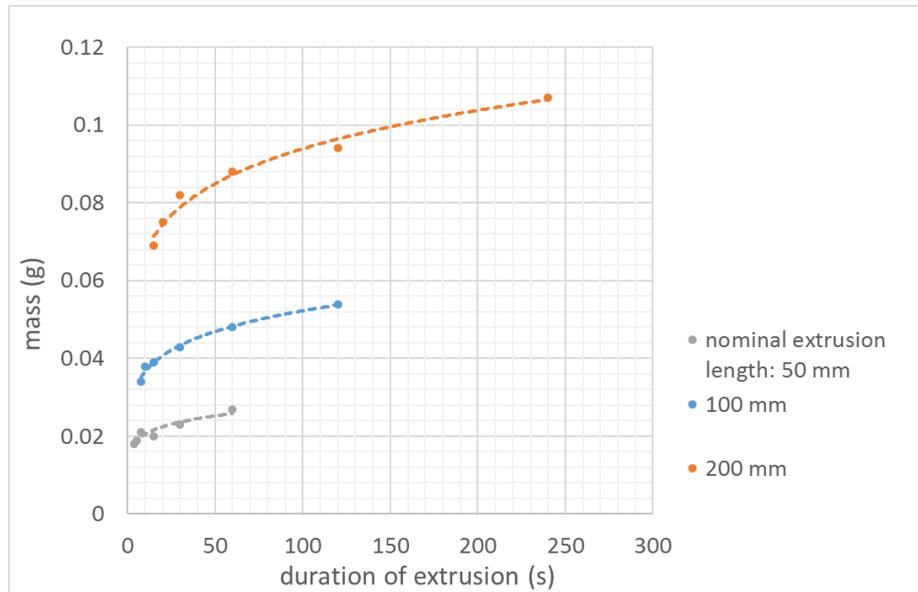
Fig. 3.20. Plot of deposited mass vs duration of extrusion for varying nominal lengths of filament.

The reason for this discrepancy can be traced to the high pressure (5 bar) exerted on the material in the feeding section of the setup, which has a time-dependent cumulative effect on the total amount deposited. High pressure was also responsible for the continuous flow of paste (*drooling*) after the rotor became stationary. However, lowering the pressure in the syringe significantly limited the attainable range of printing speeds. This problem was addressed through decompressing the nozzle's chamber and introducing a print-head cleaning stage between dispensing cycles. As can be seen in Fig 3.21, the amount of paste corresponding to 200 mm weighed twice as much as 100 mm of extruded filament across the whole range of speeds, which implies a high level of consistency of the extrusion rate.
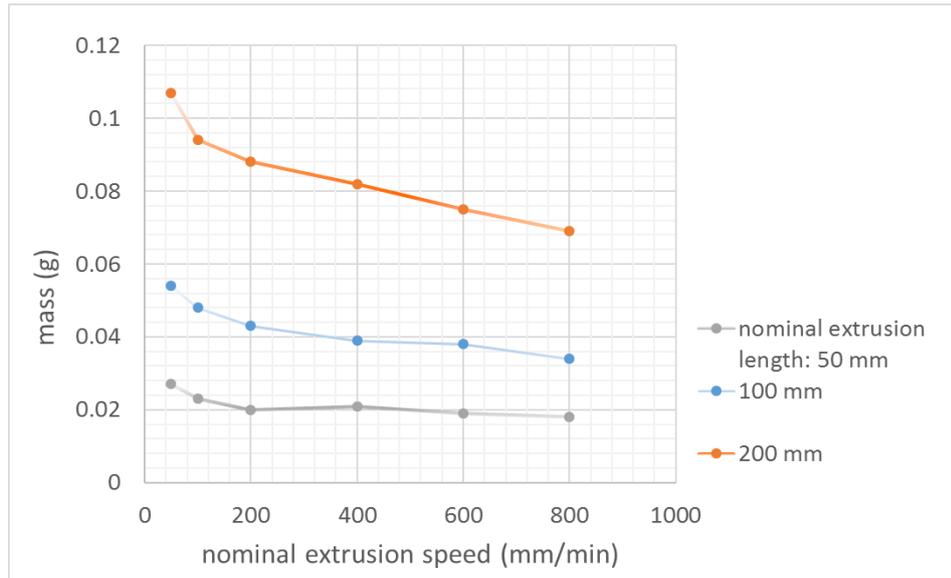
Fig. 3.21. Plot of mass vs nominal extrusion speed for varying nominal lengths of filament.

Through calibration tests it was determined that the extruder must rotate 8.5 times faster in relation to the motors that control the print-head's movement on the XY plane. With the layer thickness set at 0.38 mm, this rotational speed ratio resulted in beads approximately 0.7 mm in width. To ensure good adhesion between layers and prevent the extrusion from curling up around the nozzle, it is essential that layer height is smaller than the nominal diameter of the nozzle. Its value was established through 3D printing a series of simple orthogonal lattices with members that spanned across gaps of varying size, as shown in Fig. 3.22.
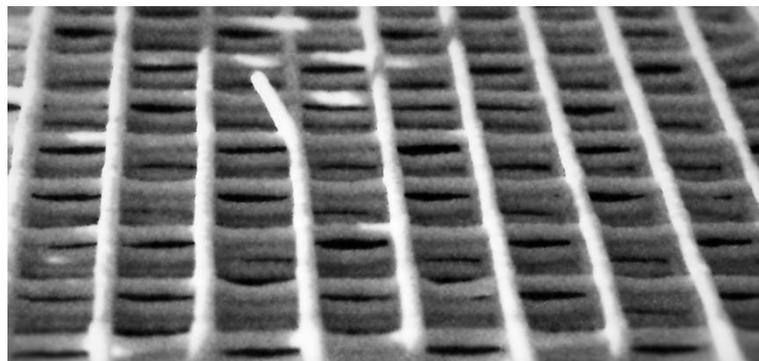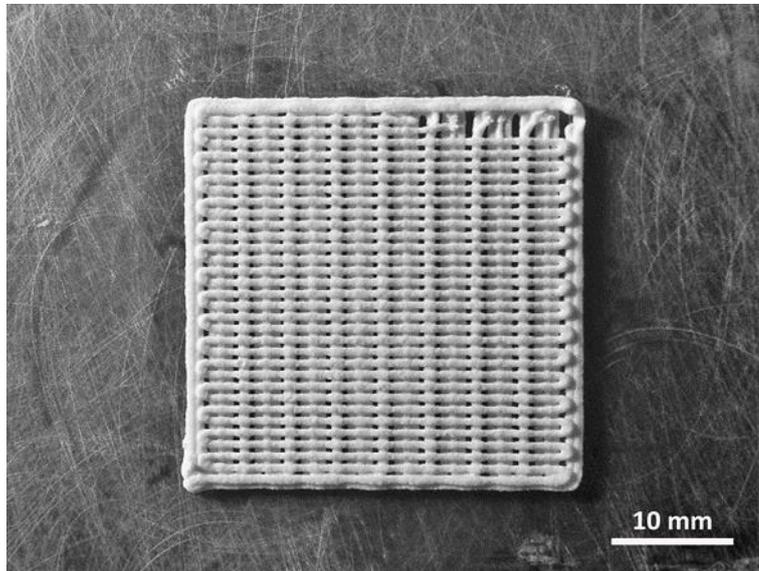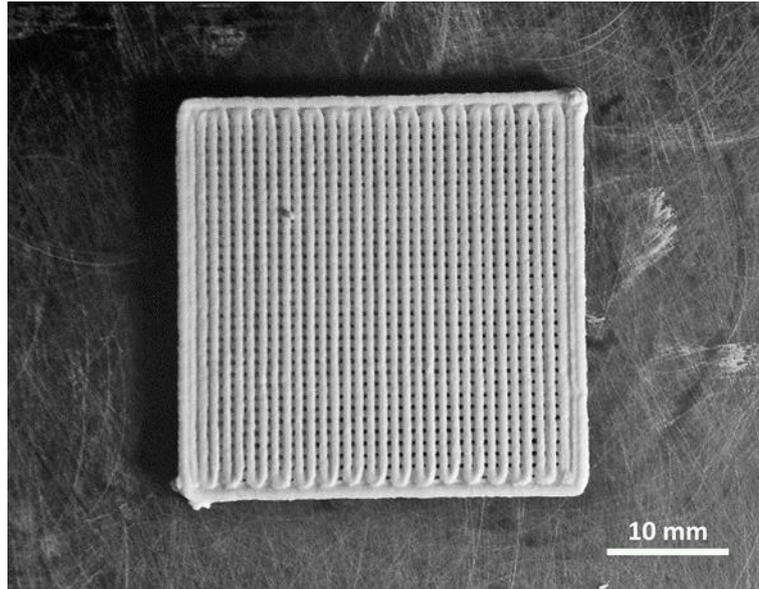
Fig. 3.22. 3D printing tests of orthogonal lattices with varying unit cell dimensions.

Overall, the system exhibited a satisfactory level of reliability and was capable of delivering reproducible results. It could potentially benefit from minor design modifications, such as:

- Minimising the clearance between the screw and its housing to prevent back-flow.

- Increasing the auger's length and/or its TPI to maximise the pressure differential between the inlet and outlet of the valve.

- Replacing Delrin® with a more durable material (i.e. stainless steel) to increase the valve's service life, since ceramic pastes can be highly abrasive.

- A significant amount of paste would occasionally accumulate between the stepper motor and the disposable material path. A rubber seal, positioned over the motor shaft, could address this issue.

Chapter 4
The effect of selected parameters on the microstructural outcome of LDM

Following the development of a printable β-TCP paste formulation and a dispensing system for Robocasting three-dimensional scaffolds, the research progressed into exploring the scope of LDM in structuring bioceramic materials at different orders of magnitude. This chapter begins with a description of the techniques and methods employed in this study and subsequently discusses the main findings. It is divided into three main sections:

- An attempt is first made to draw connections between the different variables of LDM and the overall quality of a printed object. The study subsequently emphasizes the micro-structural features in specimens comprising walls of single-bead thickness. It interprets experimental results obtained from optical micrographs using crystal growth theory.

- The second series of experiments seeks to clarify the effect of the paste's freezing rate on pore size distribution. To this end, Mercury Intrusion Porosimetry is employed in conjunction with a fluorescence-based visualisation technique, which shows the amount of free water present in the paste.

- The final part investigates how the architecture of a 3D printed scaffold influences the orientation and geometrical characteristics of the ice template. This understanding could open up opportunities for controlling with high precision the assembly of bioceramic particles at the micro-scale as the part is being fabricated.

4.1. Methods

4.1.1. Experimental setup and procedure

For the purposes of this study, the Robocasting system described in Section 3.3 was positioned in a commercial upright freezer (G591 Polar refrigeration – 440 lt). The freezer can reach temperatures down to -20°C, with the temperature fluctuating in average 0.5°C above and 1.5°C below the set value. The flow diagram in Fig. 4.1 illustrates the key stages of the experimental procedure.
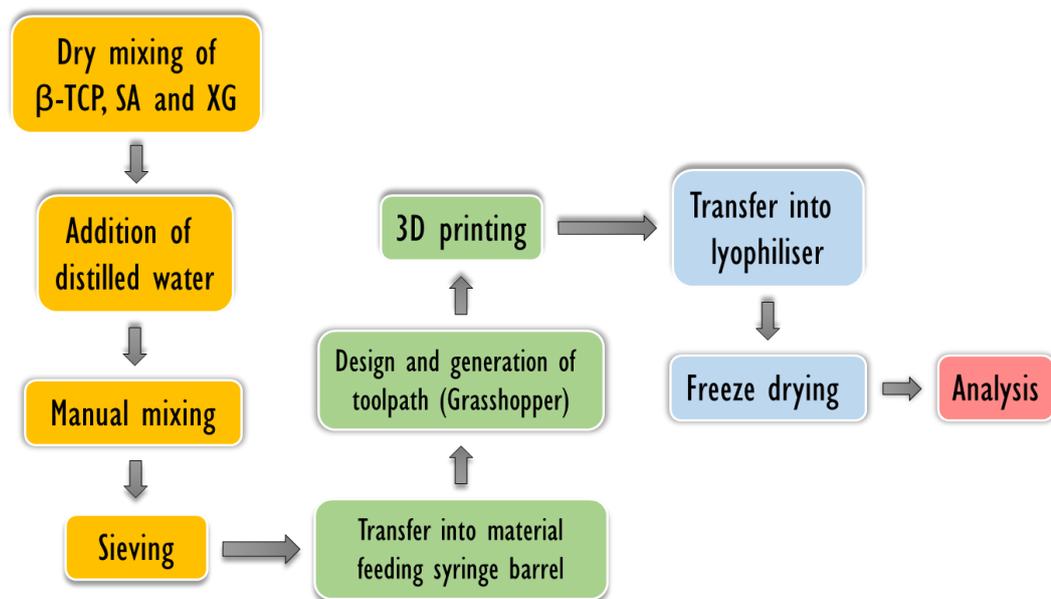
Fig. 4.1. Flow chart of the specimen fabrication process.

The parameters that determine the overall quality and microstructure of a printed object can be divided into two main categories:

- **Processing parameters:**
  - The *chamber temperature* affects directly the freezing rate of a layer.
  - Depending on the *set nozzle temperature*, and consequently the temperature of the material as it is being extruded, the ice-crystal structure in the underlying frozen layers can melt and reform several times as more layers are added.
  - *Printing speed* for a given nozzle diameter relates to the amount of material added within a specific length of time. Additionally, the slower it is, the longer the duration of contact between the previously deposited layers and the heated nozzle.
  - There is a *pause* before the addition of each layer to ensure that previous layers have solidified.
  - The *tool-path* followed can influence the degree of structural uniformity.
  - Depending on the *overall shape* of the printed part, certain sections may not be exposed to the same environmental conditions.
  - *Forced convection* can be used to achieve higher cooling rates in comparison to free convection alone.
  - The *thermal conductivity of the substrate,* upon which the object is printed, can affect the rate of heat dissipation during the deposition of the first few layers. It can also influence the extraction rate of latent

heat that is generated as the paste transitions from liquid to solid, resulting into structural differences between the base of the object and its successive layers. Furthermore, the *texture of the substrate* can determine the orientation of the ice-crystals, as it has been demonstrated with the directional freezing of ceramic slurries (Munch et al., 2009).

- **Material parameters:**

  - *Solid/Water ratio* (SWR); usually finer microstructures are obtained as the paste's water content increases.

  - With regards to *particle size* there are certain thresholds, below and above which the particles cannot be carried by the solidification front.

  - *The rheological behaviour* of the paste is of high importance, since high viscosity hinders ice-crystal nucleation and growth.

  - The presence of *additives*, such as salts or glycerol can depress the freezing point of the paste.

  - The *thermal conductivity* of particles in relation to that of the liquid can dictate whether they will be encapsulated in the freezing medium (Wegst et al., 2010).

To analyse the effect of these parameters, it is necessary to understand the key physical phenomena taking place within the colloidal paste during the LDM process. After a filament is deposited, it is cooled down to a temperature below the freezing point of water before solidification occurs. The degree of undercooling

is dependent upon the cooling rate and the intrinsic ice nucleation properties of the material. At a given printing speed, higher cooling rates can be achieved by reducing the ambient temperature. Additional key factors include the temperature and thermal conductivity of the underlying layers (or substrate), as well as the material's temperature as it is being extruded. Solidification proceeds in two distinct phases: *heterogeneous nucleation* and *ice-crystal growth*. In heterogeneous nucleation, calcium phosphate particles can act as nucleation sites. The rate at which nuclei are formed is controlled primarily by the degree of undercooling and is significantly lower at temperatures close to 0^oC. At this stage, two main mechanisms of ice-crystal growth can be identified:

a) the deposition of water molecules on an existing crystal lattice and

b) the agglomeration of small crystals to form large aggregates.

The major driving force is the difference in water concentration between the solid-liquid interface and the surrounding fluid. Water molecules diffuse through the polymer/ceramic matrix and are added to the growing crystals. As the matrix becomes progressively dehydrated, its viscosity increases and molecular diffusion slows down. Large temperature differentials between the solid-liquid interface and the bulk of the paste can yield high growth rates. However, crystallisation results in the release of energy in the form of latent heat, which is dissipated either through the crystal by conduction or into the liquid by convection. This can become a limiting factor when heat dissipation is poor. At low freezing rates the amount of heat generated is small and can be easily removed, resulting into an ice front that progresses slowly but produces large continuous crystals. Growth can also be hindered by the deposits of calcium phosphate particles that are expelled from the

solidification front and accumulate between the ice-crystals (see Fig 4.2) (Aguilera and Lillford, 2008; Cook and Hartel, 2010).

Fig. 4.2. Simplified representation of the solid-liquid interface during ice-crystal growth - adopted after (Aguilera and Lillford, 2008).

The SA/XG/β-TCP paste formulation described in section 3.2.2 was used as a model material for investigating the effect of selected processing and material parameters on part quality and micromorphology. The toolpaths used in each set of experiments were generated parametrically with Grasshopper. The paragraphs that follow demonstrate how this plugin can interface with a 3D printer; a script developed for fabricating meander-shaped specimens is provided as an example. Robocasting would commence approximately 30 minutes after the freezer had reached the desired temperature to ensure minimal temperature fluctuation around the set value. Each sample was transferred into a freeze-dryer, where it was left to dry overnight (read Section 4.1.3).

4.1.2. Parametric tool-path generation

A script for generating each sample's tool-path (see Fig. 4.3) was developed using Grasshopper for Rhino (for more information read Section 2.3). In this case, a meander was selected for its continuity, as it offered the advantage of printing an entire layer with a single start and stop. Furthermore, it allowed for a large number of segments of varying length to be generated within a surface area of approximately only 7 cm^2. This was of particular importance, since each specimen was transferred, after the completion of a printing session, into a cold chamber with limited space. Finally, it assisted in observing microstructural differences that may be present between the internal and external areas of a printed sample.
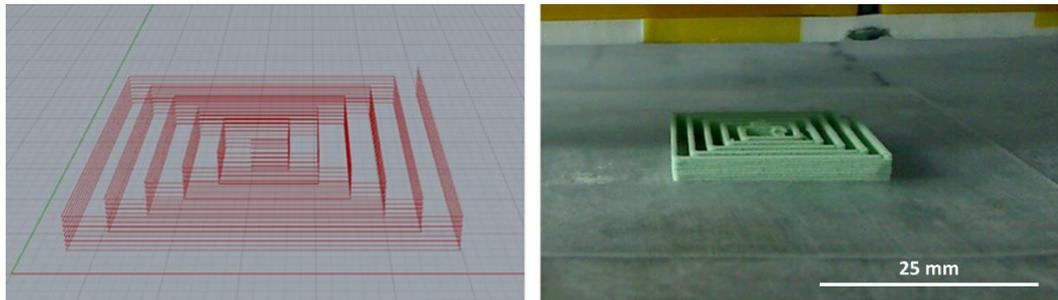
Fig 4.3. Visual representation of tool-path (left) and respective robocast part (right).

The following paragraphs describe step-by-step the tool-path (G-code) generation script and the print-head operations performed for the deposition of each layer. The script consists of two main parts: the first generates the desired geometry, while the second converts it to instructions for the 3D printer. The G-code is subsequently transferred to Repetier, an open-source 3D printing software.
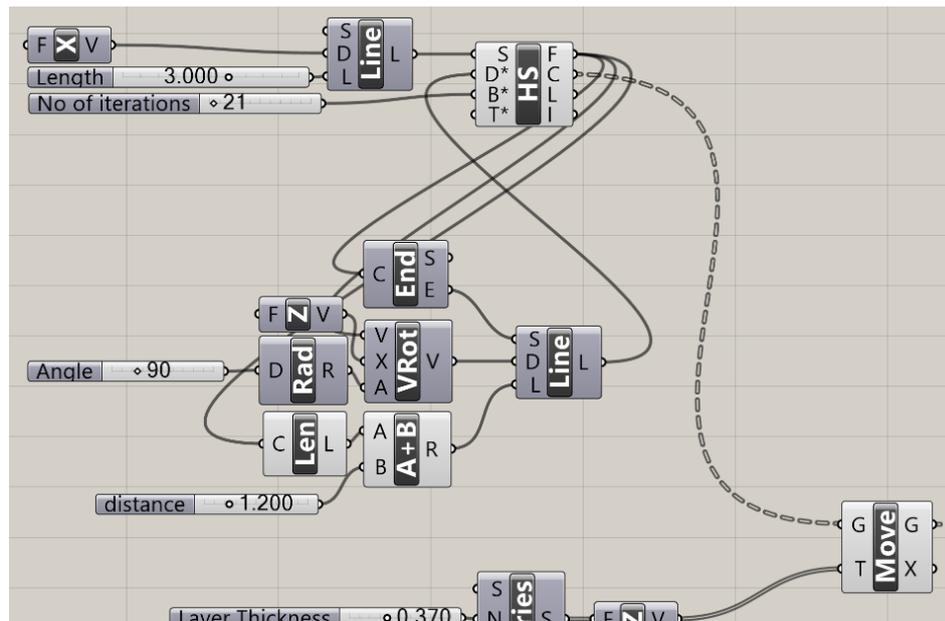
Fig. 4.4. The "Hoopsnake" (HS) feedback loop.

This script uses *Hoopsnake,* a plugin for incorporating feedback loops (Fig. 4.4). The corresponding component, named "**HS**" has the following inputs:

- **T*** triggers the execution of the loop.

- **B*** is the termination condition, which in this case is the number of iterations.

- **S** (Starting Data) is only run once and is linked to a line generating component, the starting point (**S**), length (**L**) and direction (**D**) of which can be specified.

- **D*** (Data) constitutes the main body of the loop. Initially, the components **End**, **VRot** and **Len** read respectively the end point (**E**), vector (**V**) and length (**L**) of the line (**C**) obtained from the previous iteration or *Feedback Output* (**F**). The coordinates of **E** are used to define the starting point (**S**) of the line that follows. **VRot** generates a new vector through rotating **V** by 90 degrees around the z axis. **L** is extended by a certain distance (**B**) using an addition

component (**A+B**). Finally, their outputs are fed correspondingly into the direction (**D**) and length (**L**) inputs of the next line. After the execution of the loop, the lines that have been generated are all returned as *Cumulative Feedback* to the **C** output of the **HS** component.
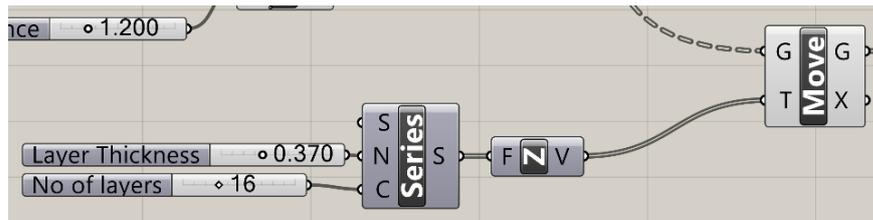
Fig. 4.5. Translation of each generated line to multiple planes.

The resulting lines are subsequently translated to multiple planes with the use of a **Move** component. Each translation (**T**) is defined by a vector along the **z** axis. A list of vectors is populated with a **Series** component, where the starting number **S**, the step size for each successive number **N** and the number of values **C** can be specified. In this regard, **N** corresponds to the layer thickness and **C** to the desirable number of layers (Fig. 4.5).
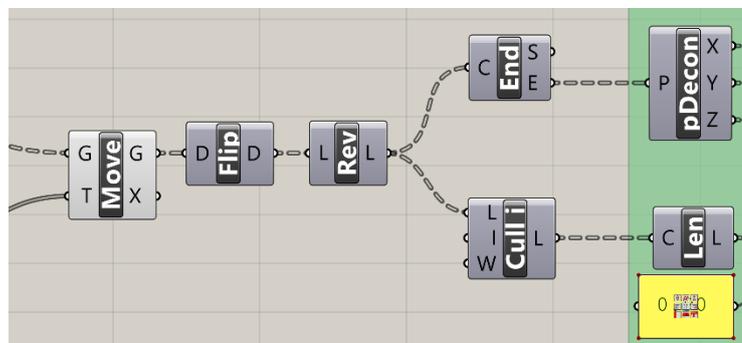
Fig. 4.6. Rearrangement of lines into a stack of meanders.

The **Flip** component in Fig. 4.6. groups the translated lines according to the vector used for their generation. It effectively arranges them into a stack of "C" number of meanders. Subsequently, the order of lines in each group is reversed using a *Reverse List* (**Rev**) function, so that the shortest line in the centre becomes the first item in the list. Thus printing starts from the centre of the pattern and moves towards the outer edge of the sample. The endpoints of each line are extracted and inserted into **pDecon**'s input. This component deconstructs a point into its Cartesian Coordinates **X**, **Y** and **Z**, which dictate the print-head's position in 3D space.
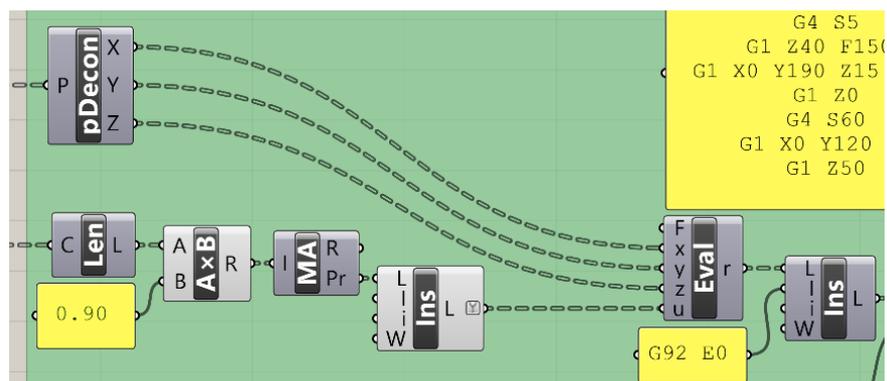
Fig. 4.7. Determination of the position (X, Y, Z) and extrusion (U) parameters of the printing process.

The synchronisation of the extruder with the movement of the print-head required the generation of yet another set of instructions. In order to extrude a filament of consistent diameter from point A to point B, the motor that powers the auger-screw valve of the dispensing unit has to rotate by a certain number of increments (steps). The default number of steps per mm of extruded material is specified in the control unit's firmware. However, the extrusion rate can be affected by the pressure inside the pressurised syringe barrel and the rheological behaviour of the

material, both of which can vary significantly. The true length of each segment is therefore multiplied by a correction factor to compensate for this effect. Subsequently, the corrected values are inserted into a *Mass Addition* (**MA**) component (see Fig. 4.7), which generates a matrix of their cumulative sums. This is done so that each layer is printed out of a single continuous line.

The Cartesian coordinates **x**, **y**, **z** and the variable **u** that specifies the volume of material deposited between two points are fed into an *Evaluation* (**Eval**) component, where a series of strings are constructed based on the following expression:

$$\textit{Format("\{0:G1 X0.00 \}\{1:Y0.00 \}\{2:Z0.00 \}\{3:U0.000\}",x,y,z,u)}$$

The output constitutes in effect the main body of G-code commands for the additive fabrication of the sample.
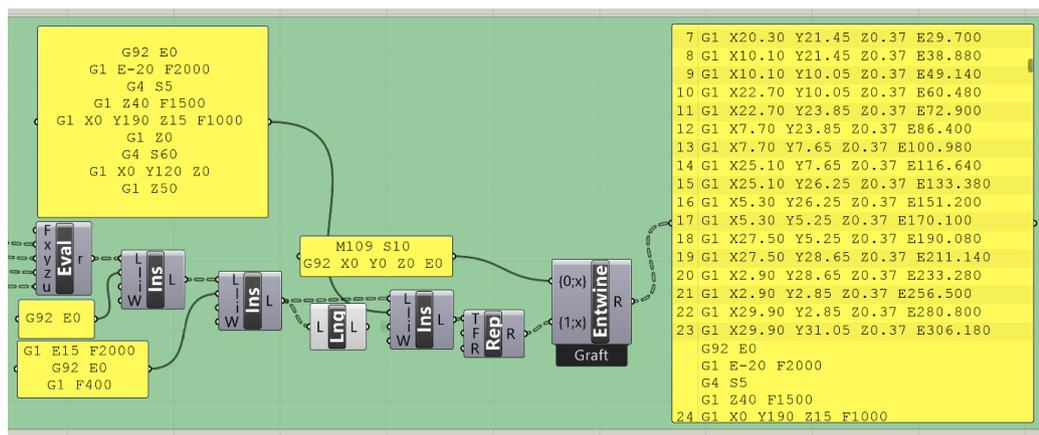
Fig. 4.8. Generation of the G-Code.

Multiple lines of strings were also manually inserted before and after each sequence of linear moves (see Fig. 4.8). These are listed in Table 4.1, together with descriptions of their corresponding actions:

M109 S10	Nozzle temperature is set at 10°C	only run once
G92 X0 **Y**0 **Z**0 **E**0	Current position set as origin/extrusion length is reset to zero	
G92 E0	Extrusion length is reset to zero	run at the start of each layer's deposition
G1 X17.9 **Y**14.85 **Z**0 **E**0	The print-head moves to the starting point of the pattern	
G1 E15 **F**2000	A small amount of material is purged/printhead is static	
G92 E0	Extrusion length is reset to zero	
G1 F400	Printing speed is set at 400 mm/min	
…		
deposition of a layer		
…		
G92 E0	Extrusion length is reset to zero	run after the deposition of each layer
G1 E-20 **F**2000	Paste retracts inside the hot-end	
G4 S5	5 sec pause	
G1 Z40 **F**1500	Print-head is lifted…	
G1 X0 **Y**190 **Z**15 **F**1000	…moved to the edge of the printbed	
G1 Z0	and lowered to zero height	
G4 S60	Printing is paused (waiting for layer to solidify)	
G1 X0 **Y**120 **Z**0	Nozzle is cleaned as the print-head travels back to the object	
G1 Z50	Print-head is lifted before a new layer is added	

Table 4.1. Manually inserted commands and their corresponding actions.

4.1.3. Lyophilisation (freeze-drying)

Lyophilisation or Freeze-drying uses sublimation to extract a solvent from a frozen mixture. Sublimation refers to the direct transition of a substance from a solid to a gaseous state without melting. The phase diagram of pure water (see Fig. 4.9) indicates that this phase transition can only occur below its triple point, i.e. below 611.73 Pa vapour pressure and 0.01^{o}C temperature.

Fig. 4.9. Phase diagram of water, after (Berk, 2009)

The entire process is carried out with the part being in a solid state, which allows for the preservation of its ice-templated microstructure and prevents its overall shrinkage. Additionally, it facilitates substantially the sintering process, since the resulting green body has an exceptionally low moisture content. Maintaining a low pressure and temperature over an extended period of time can be energy-consuming. The employment of this method, however, can be justified on the basis of the low volume and high added value of customised hard tissue implants (Berk, 2009; Franks and Auffret, 2007; Liu and Chen, 2014). The process was carried out with a benchtop Christ freeze-dryer (model ALPHA 1-2 LD) shown in Fig. 4.10. A typical setup consists of a refrigeration device, where the solution can be cooled down to the required temperature before the main drying process is initiated under reduced pressure. Some high-end units allow for the controlled heating of the solidified material so as to remove any residual water that might be present in the form of unfrozen molecules. This constitutes the secondary drying phase of the freeze-drying process. The sublimated water (vapour) is collected by a condenser or "cold trap" before it reaches the vacuum pump, preventing its corrosion and

ensuring high performance. The device employed in this study was rudimentary, without the option for controlling the temperature of a specimen or the pressure inside the freeze-drying chamber.

Fig. 4.10. The Christ ALPHA 1-2 LD freeze-dryer (left) and the condenser (right) where the samples are maintained at -20°C before the initiation of the main drying process.

Each sample, after it had been successfully printed, was transferred into the condenser, where the temperature was maintained at approximately -20°C (see Fig 4.10). It is important that this transfer is done rapidly, to minimise the risk of annealing or melting of the ice matrix. *Annealing* or *Maturation* refers to structural changes that can occur as a result of rewarming. During annealing large ice crystals grow at the expense of small crystals, resulting into reduced porosity (Franks and

Auffret, 2007). What follows is the main drying process, which was carried out overnight at a vapour pressure of 0.021 mbar.

4.1.4. Confocal Microscopy Imaging and determination of weighted average pore size and distribution

The freeze-dried samples were broken up into segments, in order to study their micromorphology in the x/z and y/z planes. Conventional optical fluorescence microscopy performs poorly when thick specimens are imaged, because fluorescent signals from areas above and below the focal plane reduce the contrast of the final image. In Laser Scanning Confocal Microscopy (LSCM) these signals are rejected through the combined use of a focused laser beam that scans the object point by point and an adjustable pin-hole aperture that is positioned in front of the electronic photon detector. A typical LSCM setup is illustrated in Fig. 4.11. A confocal microscope also uses a stepper motor that changes the microscope focus in small increments along the z - axis, generating a stack of images, each one acquired at a different focal plane. This information can be projected into a single image where all the areas of interest are in focus. The stack can also be processed in order to generate a three-dimensional representation of the specimen's surface (Murphy and Davidson, 2012). For the first set of experiments, a series of 1075x1075 px images from randomly selected areas of each sample were acquired with an effective magnification of 10x.

Fig. 4.11. Diagram of a typical confocal optical arrangement, after (Murphy and Davidson, 2012).

The generated images were processed and analysed with *ImageJ*, an open-source image processing software. The series of steps executed in order to identify and measure the pores present in an image is described in the paragraphs below:

- The information of an image in the spatial domain was converted into the frequency domain through a Fast Fourier Transform command (FFT). ImageJ produces a plot of the Fourier Transform's magnitude (amplitude), in which finer structural features correspond to higher frequencies. Similarly, large scale features are represented by low frequencies near the centre of this plot. An inverted 8bit grey-scale image with its equivalent in the frequency domain are presented in Fig. 4.12.
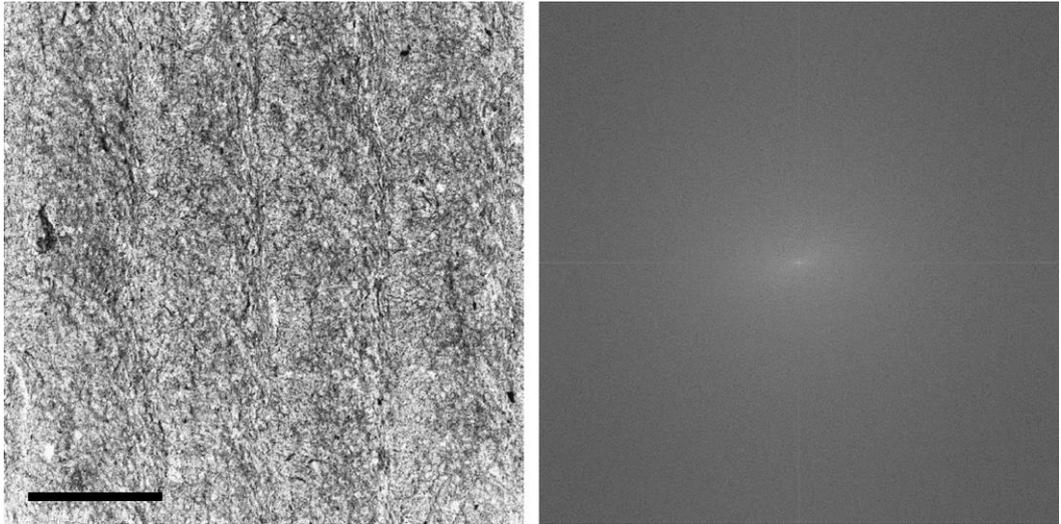
Fig. 4.12. Confocal microscopy image, scale bar: 400 µm (left) and its equivalent in the frequency domain (right).

FFT

IFFT
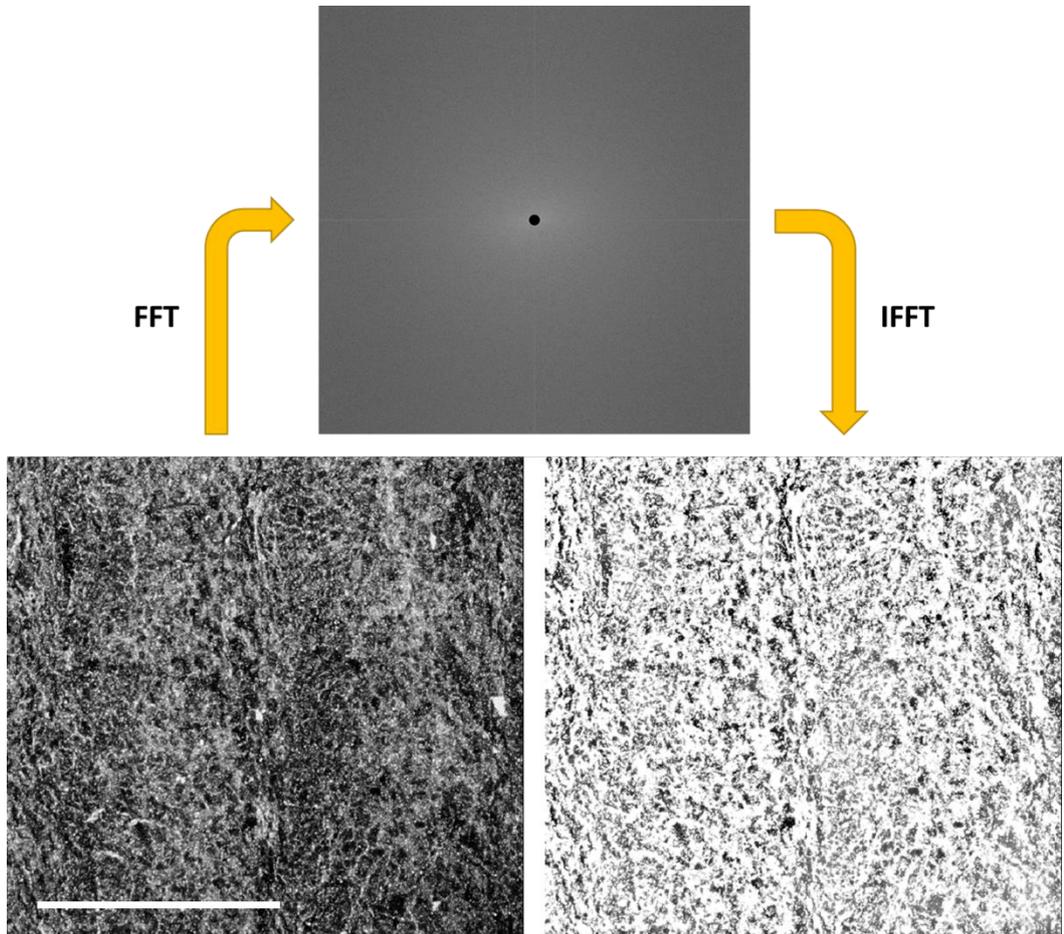
Fig. 4.13. The process of high band-pass filtering, scale bar: 400 µm.

- A mask can be applied on the Fourier Transform to discard or retain spatial frequencies below, between or above desired thresholds. A circular area (51px in diameter) in the centre of the FFT plot was cropped so as to remove low frequency artefacts (see Fig. 4.13). This procedure is termed high band-pass filtering and results in a sharper image with enhanced pore edges in the spatial domain. This image can be retrieved though Inverse Fourier Transform on the masked FFT. A detail of the image, before and after the application of the high band-pass filter demonstrates the efficiency of this particular process.
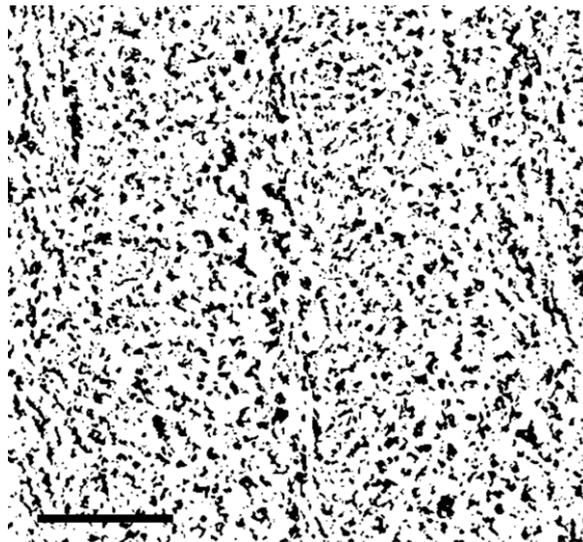
Fig. 4.14. Binary image obtained after segmentation, scale bar: 200 μm.

- This facilitated the segmentation (thresholding) process, in which the pores/voids are separated from the background in order to be measured. The resulting image is presented in Fig. 4.14. A built-in algorithm was used to calculate each pore's area and other geometrical characteristics of interest. To assess the method's reliability, a map of all the pores counted

in a microscopy image was generated and superimposed over the original image. As it is seen in Fig. 4.15, the outline of each identified void has been marked in red with a satisfactory level of accuracy.
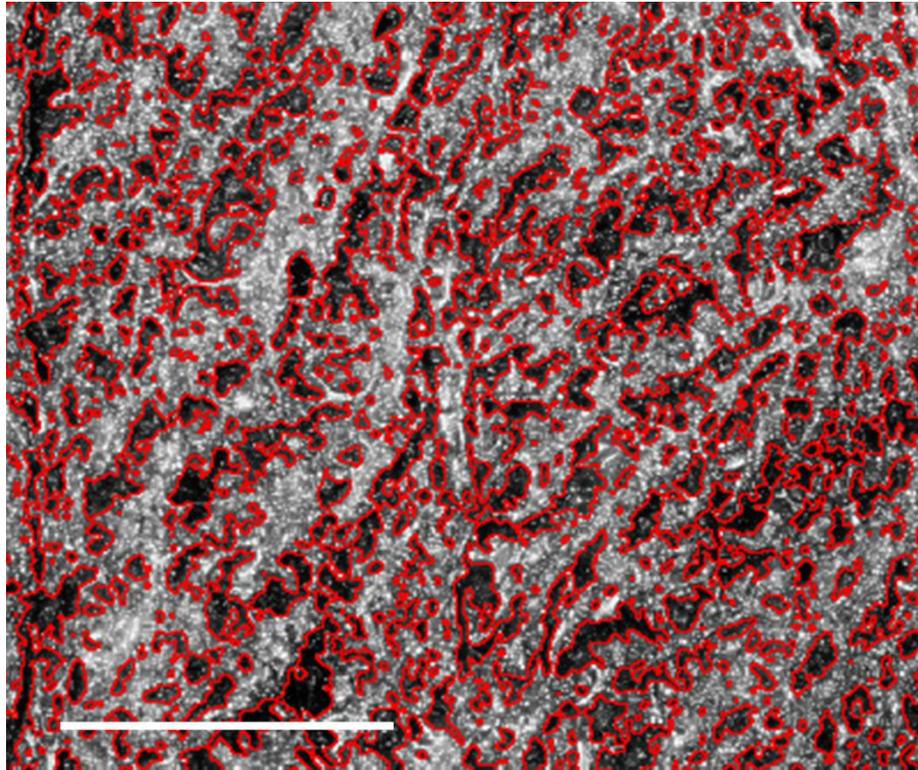
Fig. 4.15. Outlines of identified voids (shown in red) employed for assessing the efficiency of the proposed image processing and analysis sequence, scale bar: 150 μm.

The average pore surface area and its standard deviation for a specimen were determined from a sample size of approximately 15 randomly acquired images. ImageJ outputs to an Excel spreadsheet a list of the surface area of all the pores that have been identified in an image. Due to the presence of a large number of small pores ranging between 0 and 20 μm^2, the raw data distribution was heavily skewed to the left. As a result, the normal average could not be used as a variable for comparing the microstructures of different samples. For this reason, the weighted average pore size was calculated by using the squared value of each

pore's surface area, giving "more importance" to larger pores. More specifically, the sum of the square values was divided by the total surface area of the pores. A distribution plotted from the raw data and its transformed equivalent are provided for comparison in Fig. 4.16.
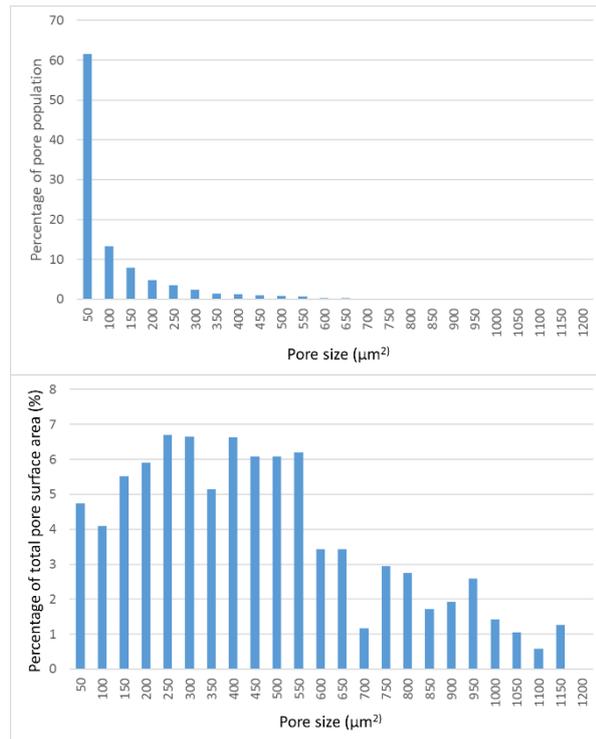
Fig. 4.16. Raw data distribution (top) vs its transformed equivalent (bottom).

The first set of experiments explored the effect of four main processing parameters on the micromorphology of a printed part, and in particular its pore size and structural uniformity; these were the chamber temperature, printing speed, set nozzle temperature and pause before the addition of a new layer, each analysed separately in section 4.2.2. The samples consisted of 9 layers and were printed on a sheet of acetate. These first experiments, despite being crude to some extent,

assisted in gaining a better understanding of the process and the mechanisms involved.

4.1.5. Fluorescence-assisted visualisation of the solidification front

Following these initial experiments, the research progressed into establishing the relationship between the freezing rate and the pore distribution in a robocast sample. A fluorescent dye (Sodium fluorescein) was added to the paste formulation so as to visualize the solidification front within a sample as it is being printed. More specifically, fluorescein is expelled from the ice crystals as they nucleate and grow. In a dehydrated state the dye has a characteristic orange-red colour. This results in a progressive reduction of the material's fluorescence intensity. One of the first experimental applications of this phenomenon is reported in a study of a saline water demineralisation process published in 1959 (Miller et al., 1959). More recently, fluorescein was used as a tracer for determining unfrozen zones of saline water solutions in coarse-grained sands (Arenson and Sego, 2006).
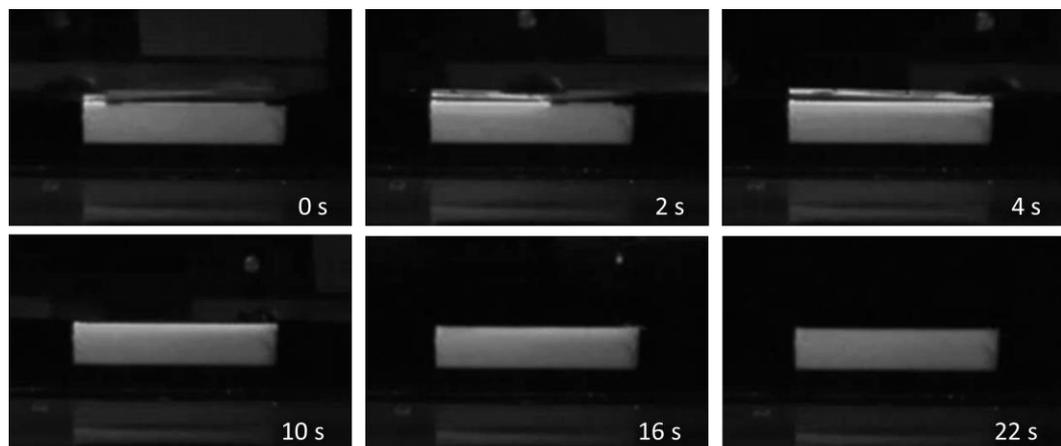
Fig. 4.17. Sequence of video frames captured at different time intervals showing the evolution of fluorescence intensity in a layer during and after its deposition.

The Robocasting process was recorded with a web camera (Logitech QuickCam Pro, 2MP) mounted on the print-bed and a UV light source directed towards the object. The recorded videos have a frame rate of 15 frames per second. The experiment was repeated for different operating conditions (8 samples in total). Figure 4.17 presents a sequence of video frames captured at different time intervals. The substrate used on this occasion was a heatsink with a heat transfer coefficient of 2.2 W/(m^{2}K), which is very close to that of ice.
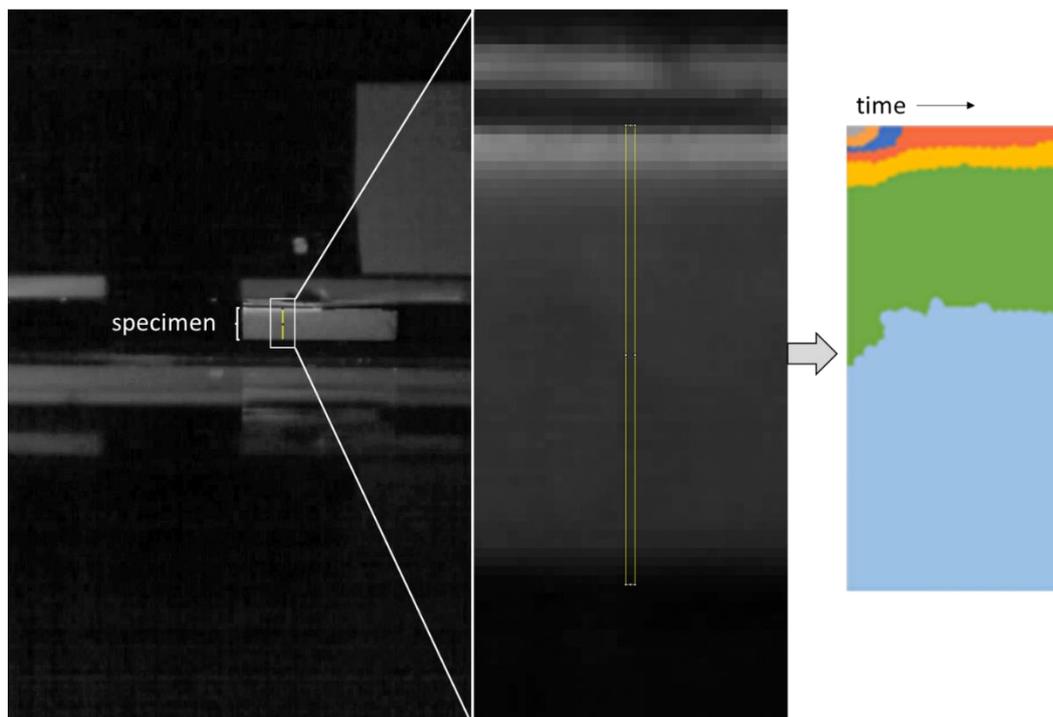
Fig. 4.18. Measurement of pixel values along a thin vertical section (marked in yellow) of the sample.

Frames from selected clips were extracted in a jpg format using Adobe Premiere. ImageJ was employed for converting the sequence from colour to 8-bit greyscale and for measuring the grey value of an array of pixels along a thin vertical section

of the sample, as demonstrated in Fig. 4.18. The number of fps was reduced to 3 in order to minimise the processing time without compromising the quality of the data. The process was automated for the entire frame sequence from the moment of deposition until the addition of a new layer. Grey values were plotted as a function of time to determine the paste's freezing rate.

4.1.6. Mercury Intrusion Porosimetry

On this occasion, Mercury Intrusion Porosimetry (MIP) was employed for measuring the overall porosity and pore size distribution, as opposed to confocal microscopy. MIP is a well-established characterisation technique for porous materials. It is important to mention that MIP measures the widest opening to a pore and not the actual size of the pore itself. For this reason, the values of diameter for internal pores are usually significantly smaller than those determined through microscopy (Giesche, 2006). Each specimen was heat treated at 50°C to remove any absorbed moisture and placed inside a penetrometer. Five segments measuring approximately 6×0.5-1×12-28 mm (W×H×L) were used for each test, which was repeated twice to ensure reproducibility of the results. A typical procedure starts from evacuating the system and introducing mercury until all the void spaces in the sample cell are filled. Following this, the pressure is increased incrementally, forcing mercury deeper into the pore network through progressively narrower channels, while continuously measuring changes in the liquid's volume. The maximum pressure attainable by the particular setup was 200 MPa. The tests were carried out by Sheffield Hallam University's Materials and Engineering

Research Institute using a Pascal 140/240 Mercury Intrusion Porosimeter in accordance with BS ISO 15901-1:2005. The results were also compared with data obtained from confocal microscopy.

MIP was also used for quantifying the effect of lower solid to water ratio, which is the sole material parameter examined in this study. The paste's water content was increased from 55.3% to 60% (w/w) and samples were fabricated at 400 mm/min with the chamber temperature set at -10 and -20°C. Their pore size distribution was compared with samples produced with the original paste composition under similar operating conditions.

4.1.7. Micro Computed Tomography (μ-CT) of 3D lattices

X-ray micro-tomography allowed for a non-destructive qualitative analysis of 3D printed lattice structures. The basic principle of μ-CT involves illuminating an object with an X-ray source. The attenuated X-rays are captured by a detector that is positioned behind the object, producing a shadow image. Attenuation is caused by absorption and scattering of photons as they travel through a material. The object is rotated in order to retrieve projections from multiple orientations. Increasing the number of projections improves the contrast between a reconstructed point and empty space. This collection of shadow images is then used in generating a sequence or stack of virtual slices of the object along an axis. A volumetric reconstruction of the entire object can be obtained from this dataset, as well as sections along arbitrarily selected cutting planes (Clerck and Postnov, 2007). In total, four samples were produced at different chamber temperatures (-5, -10, -15

and -20°C) and scanned with a Bruker SkyScan in order to compare their pore size and morphology. The facility was provided by BASF - Advanced Materials and Systems Department in Ludwigshafen, Germany.

4.2. Results

4.2.1. Macroscopic evaluation of specimens
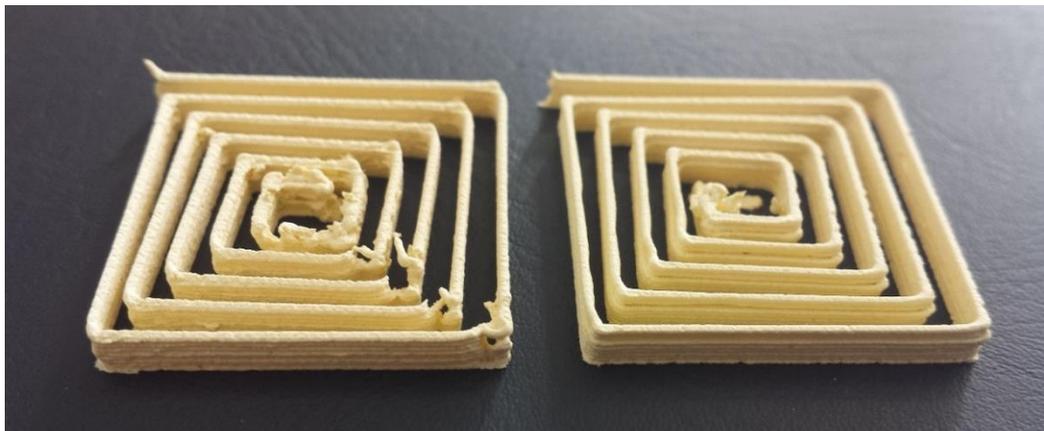
Fig. 4.19. Specimens printed with 60 s (left) and 120 s (right) of pause between layers.

The quality of a printed object was reliant predominantly on the speed at which it has been printed. Outside a certain range of speeds, it was virtually impossible to complete the Robocasting process successfully owing to slumping of the underlying layers. Providing that the ambient temperature remained constant, this range became gradually narrower as the temperature of the extrudate increased. Its extent was reduced dramatically for specimens printed at ambient temperatures close to the freezing point of water; at -5°C it spanned only between 200 and 600 mm/min. This is illustrated in Tables 4.2 to 4.5, where a gradual decline in quality is evident at low speeds (failed attempts are marked in red). The duration of pause before the deposition of a new layer also had a significant effect. This is evidenced

in Fig. 4.19, where an increase of 60 s improved the overall quality of parts printed

at -20ºC, 800 mm/min and 30ºC SNT.
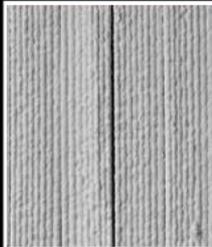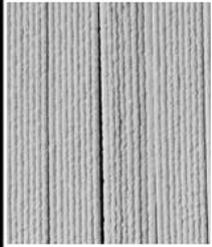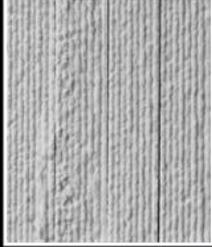
Table 4.2. Side profiles of sample segments printed at -5ºC.

Speed (mm/min) / SNT (°C)	5	10	20
50			
100			
200			
400			
800			

Table 4.3. Side profiles of sample segments printed at -10ºC.

SNT (°C) \ Speed (mm/min)	10	20	30	40
800				
400				
200				
100				
50				

Table 4.4. Side profiles of sample segments printed at -15°C.

SNT (°C) / Speed (mm/min)	50	100	200	400	800	120 s pause 800mm/min	180 s pause 800mm/min
20							
30							
40							

Table 4.5. Side profiles of sample segments printed at -20ºC.

4.2.2. *The effect of selected processing parameters on average pore size*

4.2.2.a. Chamber temperature

The general trend that was observed with increasing chamber temperature was larger pores. This is evidenced by measurements of the weighted average pore size in samples printed at 200 and 400 mm/min (see Fig. 4.20) and appears to correlate with the theory described in the paragraph above. More specifically, a chamber temperature of -5°C favoured ice-crystal growth, in contrast to printing at -20°C, where ice-nucleation was more pronounced. At high printing speeds, i.e. 800 mm/min, the values of weighted average pore size across all samples seem to converge.
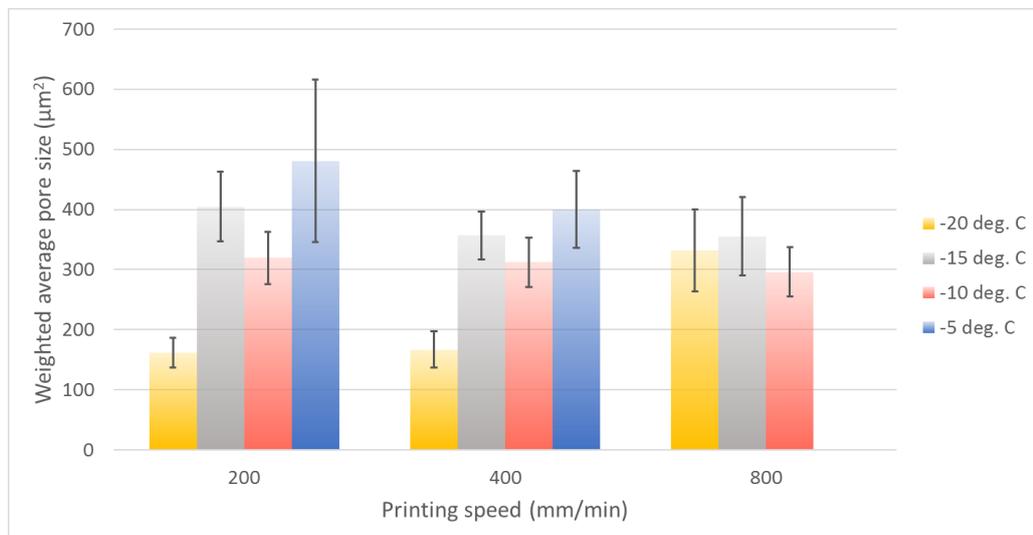
Fig. 4.20. The effect of chamber temperature on the weighted average pore area
of specimens printed at different speeds.

An additional observation is that specimens fabricated at -15°C exhibited larger pores than those at -10°C. There are several possible reasons for this behaviour; the time elapsing between the completion of a layer and the addition of a new layer

was only 60 s for the former set of experiments and 180 s for the latter. In this case, it appears that ambient temperature played a secondary role: this short pause of 60 s could entail a higher temperature and reduced degree of solidification in the preceding layers at the moment of deposition. This particular effect is discussed in more detail in Section 4.2.2.d. Moreover, there is a possibility that the conditions were such that the maximum rate of transformation was achieved. The transformation rate is a product of the nucleation and growth rates.

Finally, it is worth noting that the set nozzle temperature was not the same across the experiments compared in this section. However, there was a minimum temperature, under which the paste could not be extruded, as it froze at the tip of the nozzle. This varied between 5 and 20°C depending on the ambient temperature. These values were determined through a process of trial-and-error and assisted in making some rough comparisons between the samples.

4.2.2.b. Printing speed

Printing speed refers to the speed at which the print-head travels while extruding material. It is related to the amount of material deposited within a certain length of time (deposition rate) and also to the duration of contact between the heated nozzle and the preceding layer. Figures 4.21 and 4.22 suggest that both high and low printing speeds (below 200 mm/min) had a similar effect. Not only did they reduce the cooling rate of a new layer, but even caused melting and slumping of the underlying frozen structure. A common finding in both extremes was large pore size heterogeneity within a sample. This was observed at all chamber temperatures

and was more pronounced at higher set nozzle temperatures. This is due to the greater amounts of thermal energy being conducted through the frozen medium. The dissipation of heat dictates the microstructural outcome and overall quality of a print. This depends on a number of factors including the chamber temperature and local density, volume and geometry of the frozen structure.
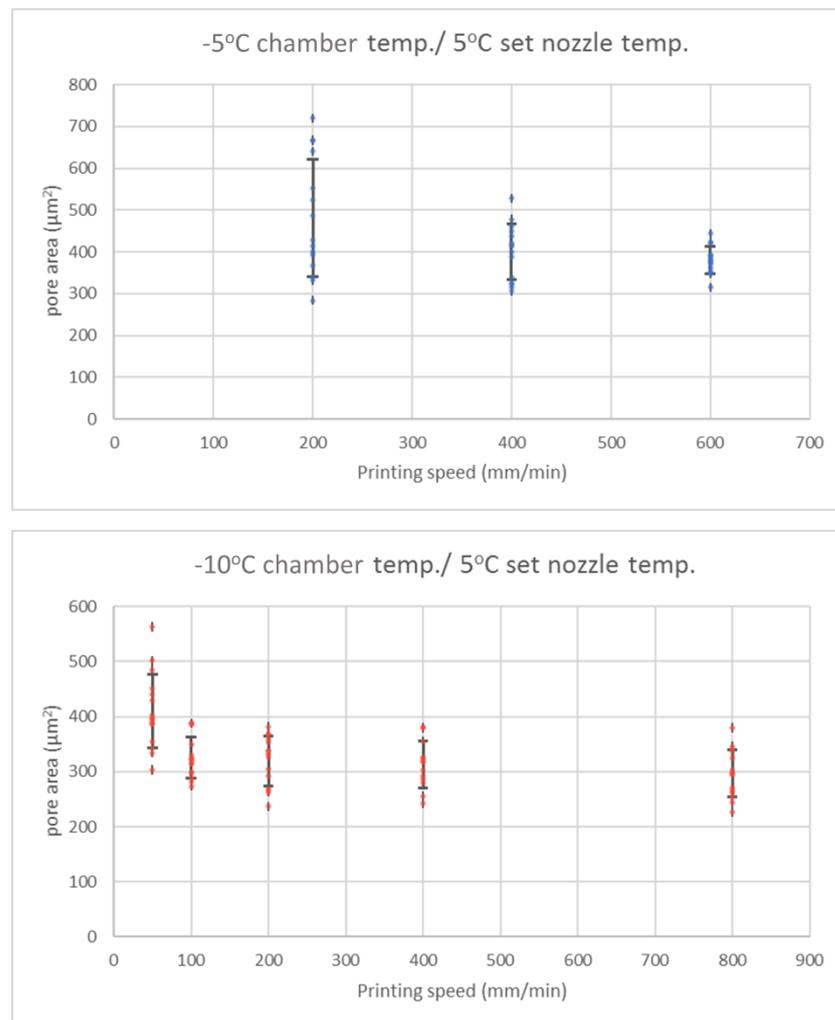
Fig. 4.21. Plots of pore area vs printing speed for specimens printed at -5 and -10°C respectively.
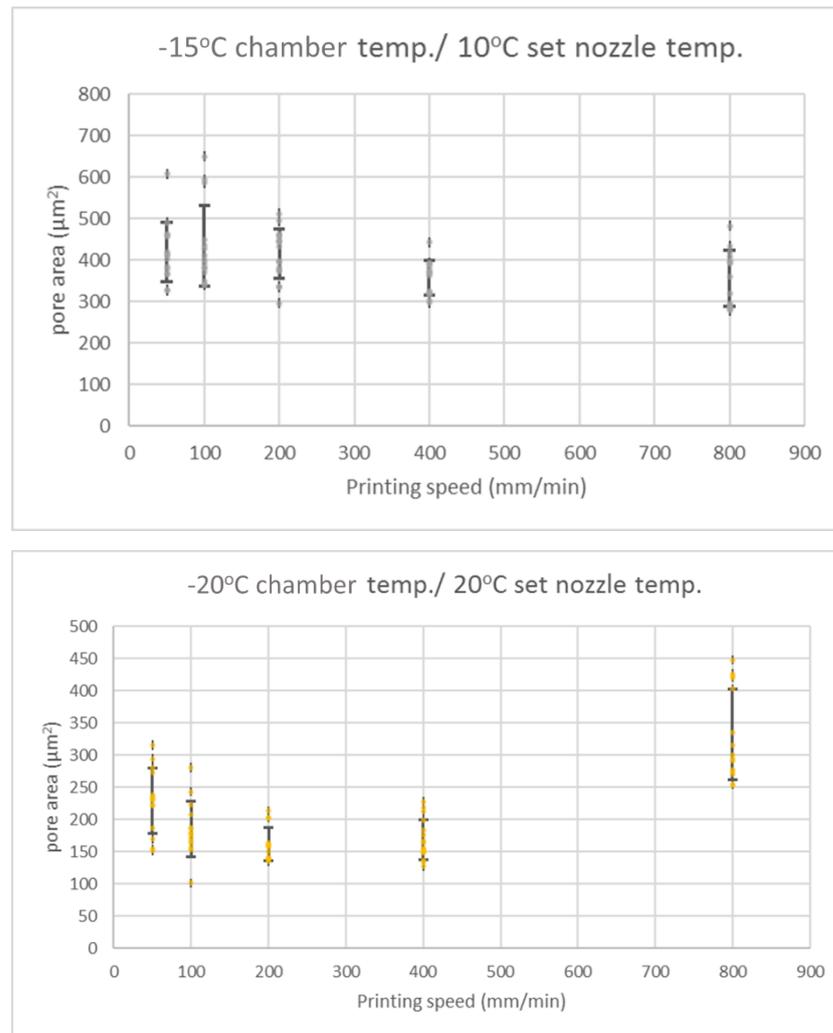
Fig. 4.22. Plots of pore area vs printing speed for specimens printed at -15 and -20°C respectively.

Furthermore, specimens printed at low speeds exhibited clusters of comparatively large pores, resulting in a more localised variation in pore size. On the contrary, those printed at high speeds displayed a smooth transition between pore sizes in the form of extensive micro-structural gradients. The cause of this discrepancy possibly lies in the phenomenon of Ostwald ripening, in which large crystals grow at the expense of smaller ones. Each time a new layer is deposited, an amount of energy is added to the underlying ice structure. This accelerates the rate of Ostwald ripening, gradually increasing the size of ice crystals as more layers are added. The

rate and degree of localisation of the supplied heat could therefore be responsible for the microstructural differences observed between these two extreme cases. At high printing speeds, the heat originating from the filament as it is being deposited, is distributed more evenly throughout the system. Alternatively, when the print-head is travelling at low speeds, a high degree of heat localisation exists. Additionally, the total amount of energy supplied to the system increases the longer it is in contact with the heated nozzle. A sharp increase in pore size from 175 to 350 μm^2 can be noticed at -20°C, between specimens fabricated at 800 and 400 mm/min. The reason may lie in the elevated amounts of latent heat that were released as larger volumes of paste solidified, coupled with the phenomenon of Ostwald ripening as described above.
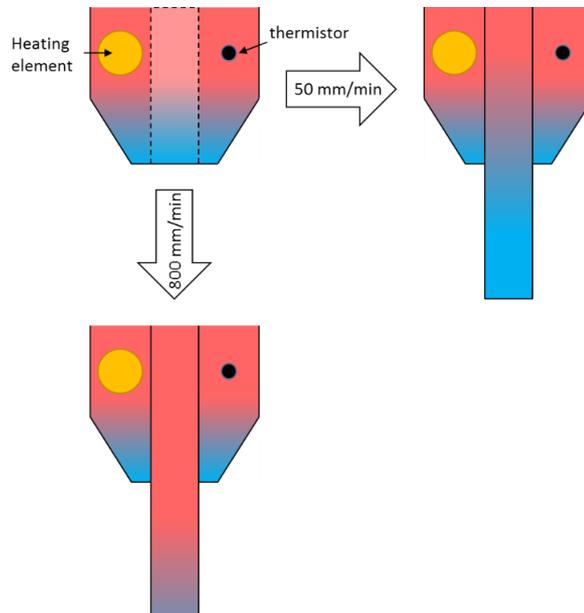
Fig. 4.23. Schematic representation of the temperature gradient along the filament for two extreme scenarios of printing speed.

It is important to note that printing speed also affected the temperature of the material as it is being extruded. A temperature gradient exists along the heated

127

nozzle (see Fig. 4.23), whose lower limit is dictated by the temperature inside the freezer. Consequently, low extrusion rates can shift the extrudate's temperature towards this lower limit, altering the way it freezes. At high printing speeds, the temperature of the material is expected to be closer to that which the nozzle is set to. Figures 4.24 and 4.25 provide a comparison between the microstructures of two pairs of samples. Each pair was printed at the same ambient temperature (-20 and -10°C respectively) but at different speeds.
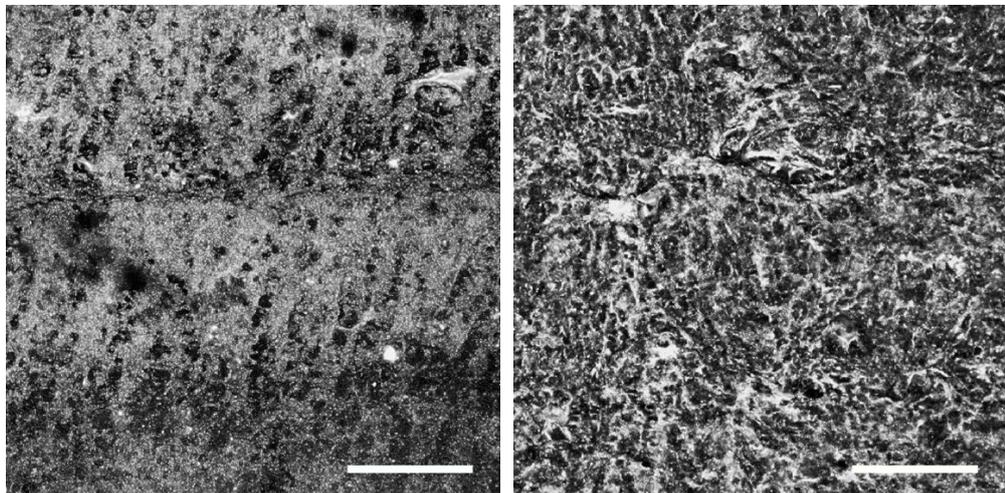
Fig. 4.24. Confocal microscopy images of specimens printed at -20°C and 50 mm/min (left), 800 mm/min (right). The scale bar corresponds to 200 μm.
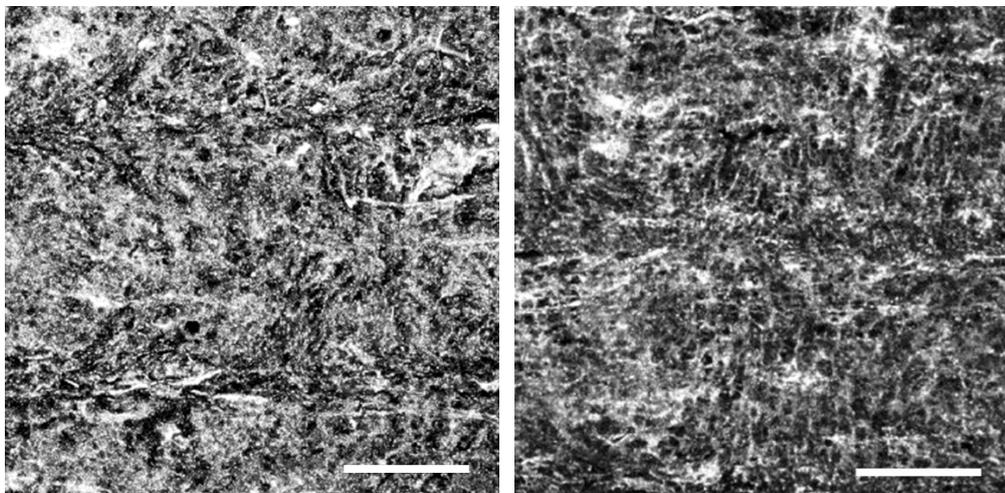
Fig. 4.25. Confocal microscopy images of specimens printed at -10°C and 50 mm/min (left), 800 mm/min (right). The scale bar corresponds to 200 μm.

4.2.2.c. Set nozzle temperature (SNT)
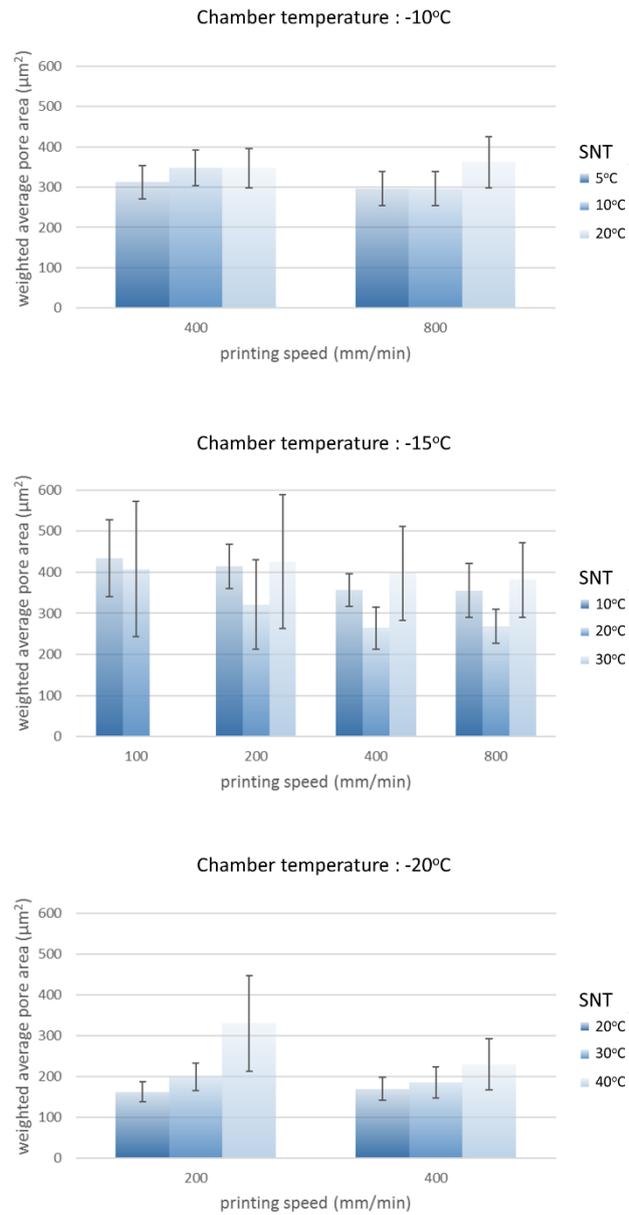
Fig. 4.26. Charts of weighted average pore area - samples printed with varying set nozzle temperature and speed at -10, -15 and -20° C respectively.

The system had some inherent limitations due to the configuration of the hot-end. The temperature of the material as it is being deposited could not be controlled with precision. This, however, did not pose a problem when studying the effect of increasing nozzle temperature. Fig. 4.26 presents a series of graphs that illustrate

the variation in pore size at -10, -15 and -20°C. It was not possible to raise the temperature of the nozzle above 5°C for specimens fabricated at -5°C due to their collapse. Both at -10 and -20°C, a slight increase in pore size was observed at elevated set nozzle temperatures. Samples printed at -15°C did not seem to follow the same pattern. Paradoxically, printing with a nozzle temperature set to 20°C resulted into smaller pores compared to 10°C. This difference was more pronounced at speeds above 200 mm/min and its cause remains unclear. From the standard deviation of the weighted average pore area values for each sample it can be deducted that high extrusion temperatures widen the spread of their distribution; in other words, they introduce micro-structural heterogeneities. Fig. 4.28 demonstrates this effect more clearly with a number of confocal microscopy images from specimens that were printed at -15°C. The graph also suggests that the impact of high nozzle temperature can be minimised by either increasing the printing speed or extending the duration of time for which the printer remains idle following the completion of a layer. The latter is discussed in the section that follows.

Finally, Fig. 4.27 provides a summary of the effect of all three processing conditions on weighted average pore area.
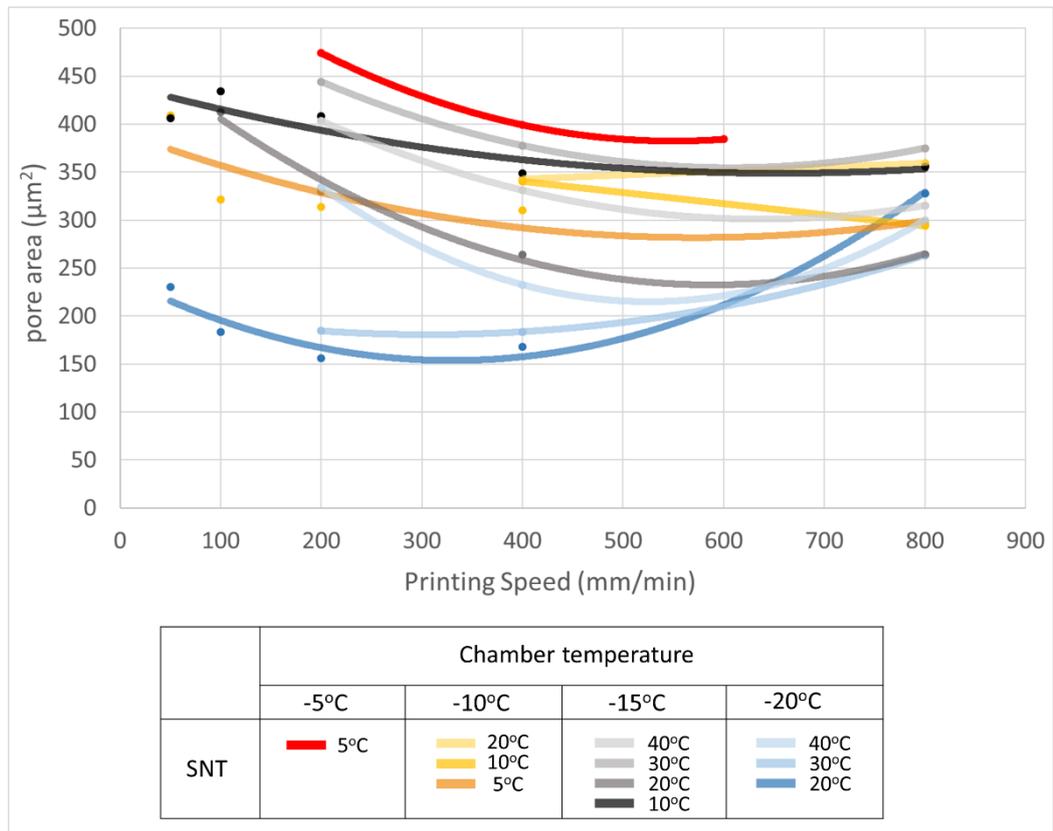
Fig. 4.27. Summary plot of pore area vs printing speed for specimens
printed at varying operating conditions.

4.2.2.d. Pause

A short pause after the deposition of each layer was essential for the successful
fabrication of a part, as it allows for its solidification and cooling before the addition
of another layer. The duration of this pause depends on the set freezing and nozzle
temperatures. Figure 4.28 illustrates how a prolonging of this duration by 60 s, not
only allowed for printing with the nozzle set at 40°C, but also delivered a more
homogenous part.
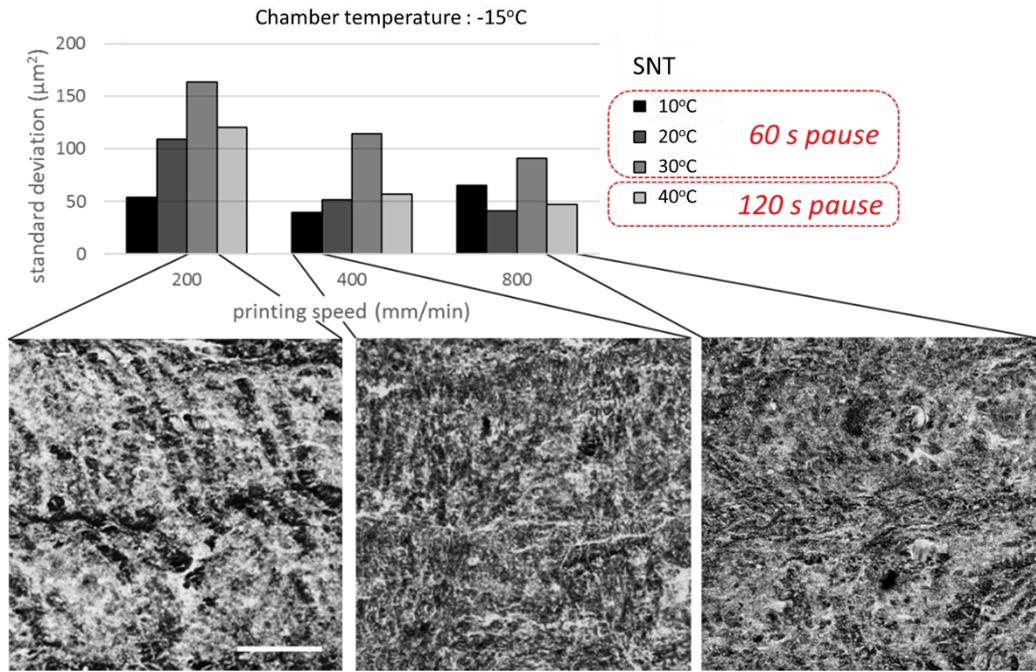
Fig. 4.28. Illustration of the effect of set nozzle temperature and pause between layers on the standard deviation and microstructural features of a series of samples printed at -15°C (scale bar = 200 μm).
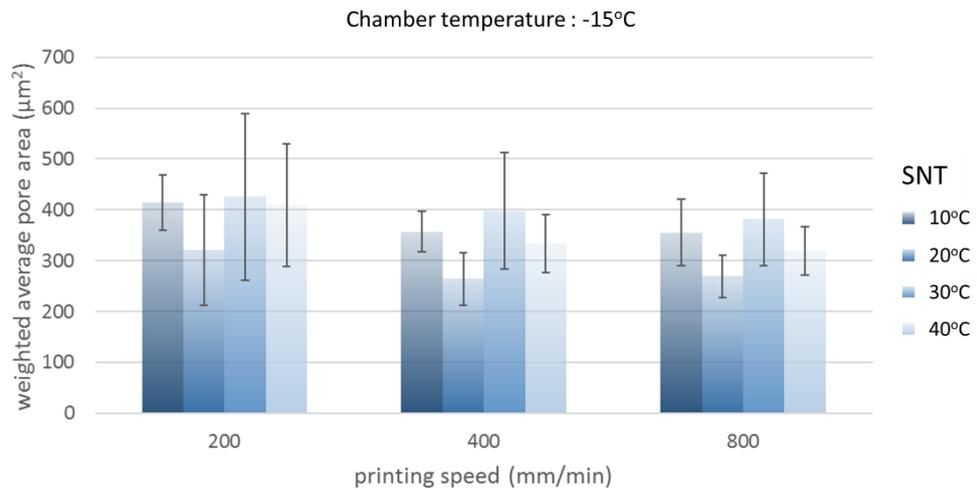
Fig. 4.29. The reduction in pore size at 40°C compared to 30°C SNT is attributed to an increase in the duration of pause.

This observation is further reinforced by the chart in Fig. 4.29, which shows that despite the high extrusion temperature, a reduction in pore size was achieved at 200 and 400 mm/min. Similar conclusions can be drawn from experiments

conducted at -20°C and speeds of 800 mm/min, which were impossible to complete successfully at nozzle temperatures above 30°C without increasing the length of rest. The graph presented in Fig. 4.30, indicates a considerable enhancement in micro-structural uniformity in comparison to lower extrusion temperatures.
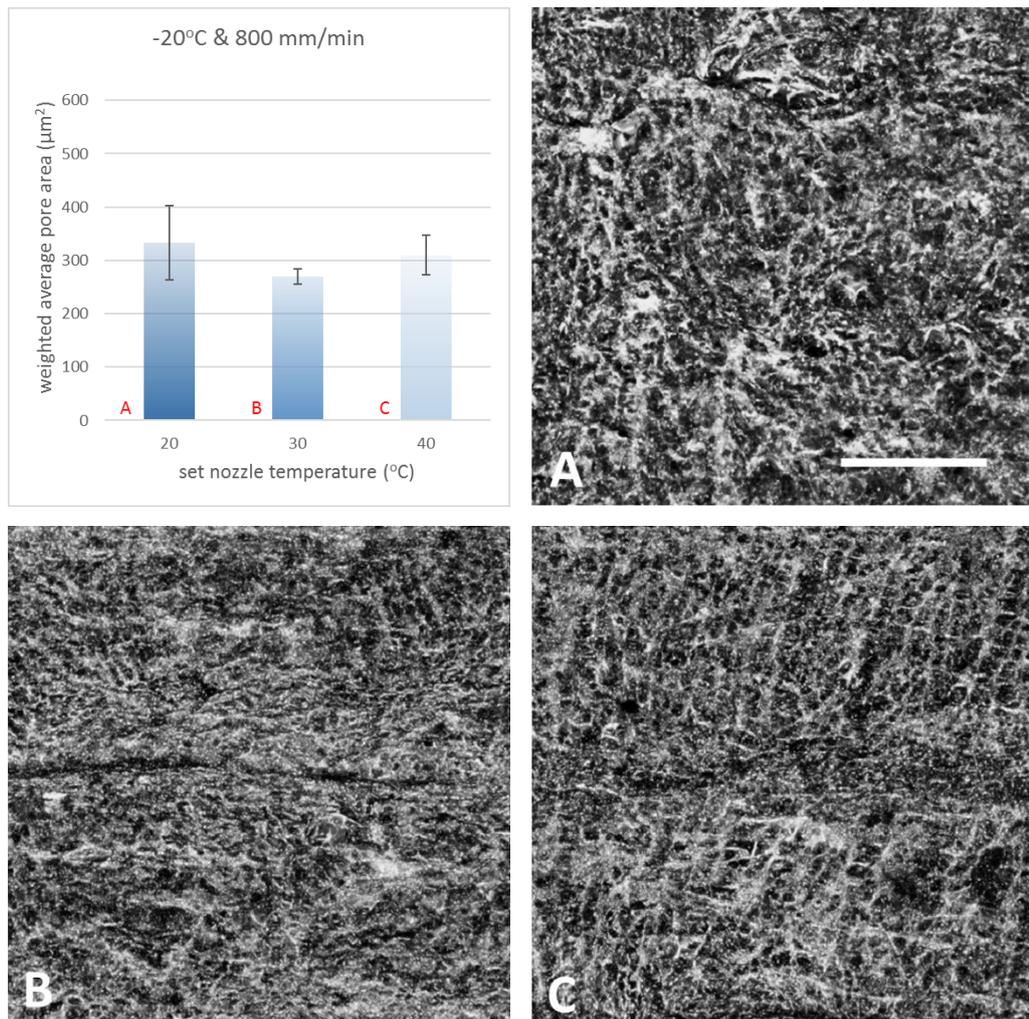
Fig 4.30. Printing with higher SNT at -20°C and 800 mm/min was made possible through prolonging the pause by 60 (B) and 120 s (C). A reduction in pore size for sample B compared to A is evident in the corresponding microscopy images (scale bar = 200 μm).

4.2.3. Drawing connections between pore size distribution and freezing rate

4.2.3.a. Pore size distribution as determined by MIP

The pore structure properties of 8 samples, printed at varying operating conditions are summarised in Table 4.6. Their theoretical maximum attainable porosity was estimated at approximately 80%, based on the volumetric proportion of water present in the mixture. There was large discrepancy between this value and the actual porosities determined by MIP, which range between 40.1 and 57.8%. This can be attributed to the following reasons:

- A small volume of water remained in the sample.

- Collapsed pores during the freeze-drying process causing shrinkage.

- Porosity in the nano-scale, below the minimum value measurable by the system (7nm).

- Ineffective (closed) porosity.

Sample	Operating conditions	Modal pore diameter (μm)	Porosity (%)	Total pore surface area (m^2/g)
A	-5°C ; 400 mm/min ; 5°C SNT	13.168	40.01	2.186
B1	-10°C ; 400 mm/min ; 5°C SNT	5.458	53.48	2.529
B2	-10°C ; 800 mm/min ; 5°C SNT	5.267	57.8	2.774
C1	-15°C ; 400 mm/min ; 10°C SNT	5.663	56.17	4.069
C2	-15°C ; 400 mm/min ; 20°C SNT	6.137	48.11	1.888
D1	-20°C ; 200 mm/min ; 20°C SNT	4.756	52.14	1.595
D2	-20°C ; 400 mm/min ; 20°C SNT	5.086	54.11	1.217
D3	-20°C ; 800 mm/min ; 20°C SNT	5.078	53.98	2.366

Table 4.6. Values of modal pore diameter, porosity and total pore surface area for specimens printed under varying operating conditions as determined by MIP tests.

Freezing conditions can influence the total amount of water that gets converted into ice. As freezing takes place, a solute-rich phase with a rubbery consistency is formed between the growing ice needles. The freezing point of this matrix is

depressed as the concentration of the solute increases. The higher the rate of ice-crystal nucleation and growth, the lower the moisture content and viscosity of this phase. Part of the water is also sorbed to the polymer mixture, acting as a plasticiser (Fennema, 1996). For this reason, a certain amount of non-crystallised water is always present in what appears to be a frozen mixture. Further cooling of the samples to -20°C in the lyophiliser may form crystallites in the freeze-concentrated matrix; however, their size is restricted by its extremely high viscosity. During freeze-drying, it is possible for some pores to partially collapse under gravity or capillary pressure. To prevent shrinkage, it is important that this amorphous phase is in a glassy state as the ice-crystals sublime. To achieve this, freeze-drying must be performed at temperatures below its glass transition temperature (T_g), which is inversely proportional to water content (Krokida et al., 1998). When most of the ice has sublimed, the temperature rises and the unfrozen water is diffused out of the glassy matrix (secondary drying). At this stage, if the framework is not rigid enough, significant shrinkage can occur (Franks and Auffret, 2007). A large amount of non-crystallised water in the original frozen structure perhaps explains why the porosity obtained at -5°C (40.01%) was significantly lower than the average porosity (52%) of all the samples compared in this study.

The mercury's intrusion volume was plotted as a function of pore diameter to determine the effect of chamber temperature on pore distribution. As shown in Figure 4.31, the pore distribution in *A* was skewed towards larger diameters in comparison to samples *B1, C1* and *D2*. More specifically it peaked at approximately 13 μm, which is nearly three times higher than the values corresponding to lower

chamber temperatures (5 μm). Additionally, samples *B1* and *C1* had a higher percentage of pores ranging between 6 and 12 μm than *D2*.
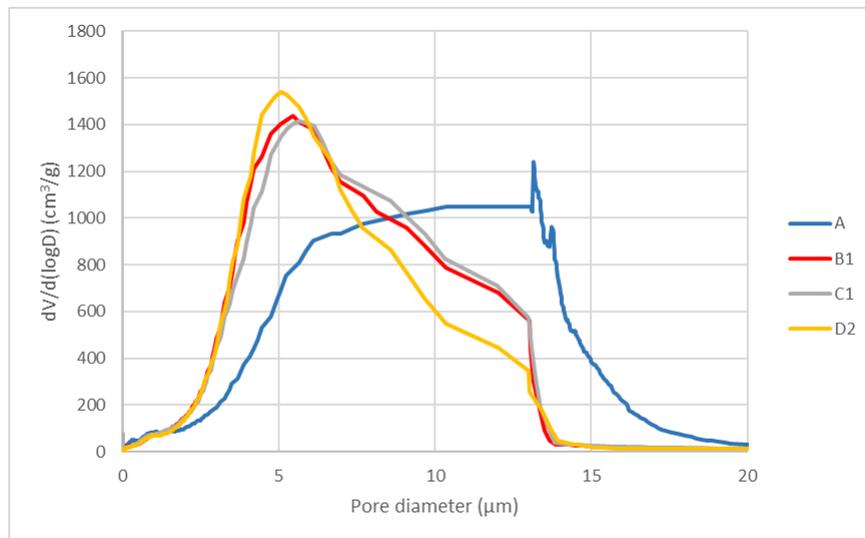
Fig. 4.31. Pore distribution for samples fabricated at different chamber temperatures: -5°C (A), -10°C (B1), -15°C (C1) and -20°C (D2).
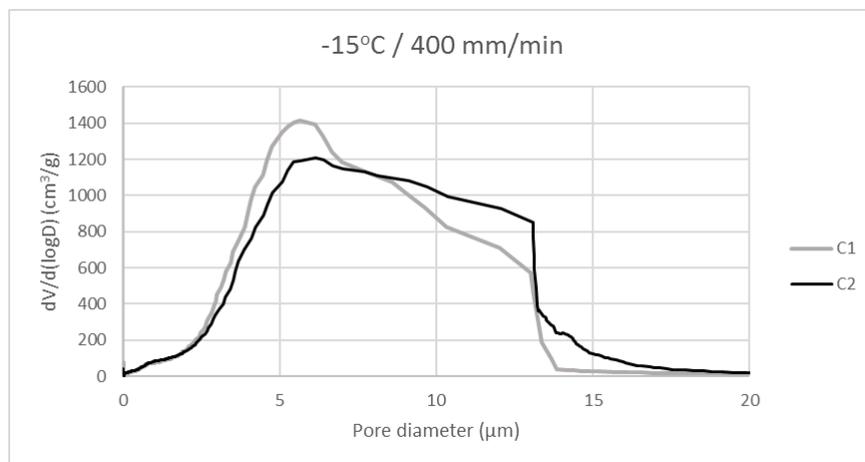
Fig. 4.32. Pore distribution for samples fabricated at -15°C and different set nozzle temperatures: 10°C (C1) and 20°C (C2).

As can be seen in Figure 4.32, increasing the temperature of the heated nozzle by 10°C, not only widened the pore distribution but also shifted it towards larger diameter values. For example, the volume of mercury that corresponds to 13 μm increased by 30%. This appears to have occurred at the expense of pores ranging

between 1 to 8 μm. Fig. 4.33 and 4.34 suggest that printing speed did not alter the pore size distribution in samples fabricated at -20 and -10°C. These results contradict some of the observations made in Section 4.2.2. *D3*, in particular, was expected to contain larger pores in comparison to *D1* due to the higher deposition rate. The reason for this discrepancy perhaps lies in the use of a heat sink as a printing substrate instead of a sheet of acetate, as in the first series of experiments.
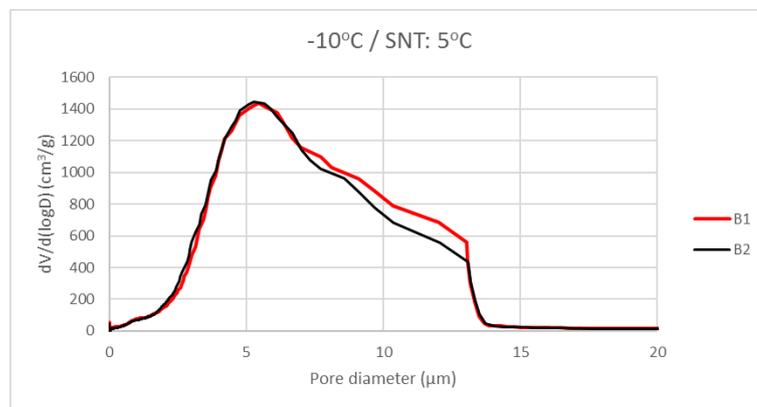
Fig. 4.33. Pore distribution for samples fabricated at -10°C and varying printing speeds: 400 (B1) and 800 mm/min (B2).
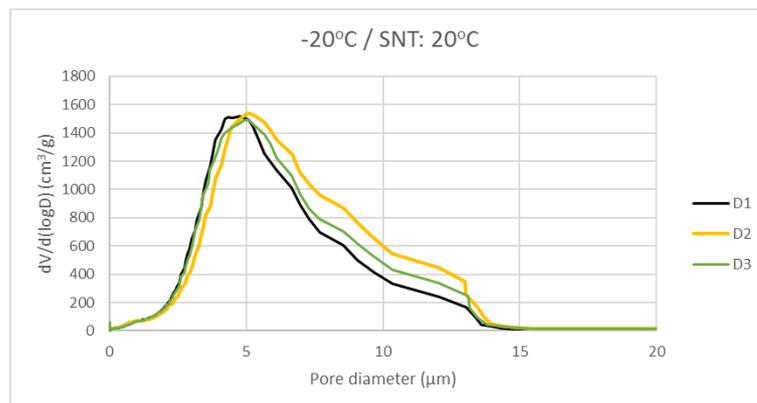
Fig. 4.34. Pore distribution for samples fabricated at -20°C and varying printing speeds: 200 (D1), 400 (D2) and 800 mm/min (D3).

4.2.3.b. Freezing front velocity

The evolution of fluorescence intensity with time across samples *A, B1, C1* and *D2* is plotted in Fig. 4.35. Each colour corresponds to a range of intensity values. It was observed that lowering the chamber temperature increased the speed of the solidification front with its main direction being away from the substrate.
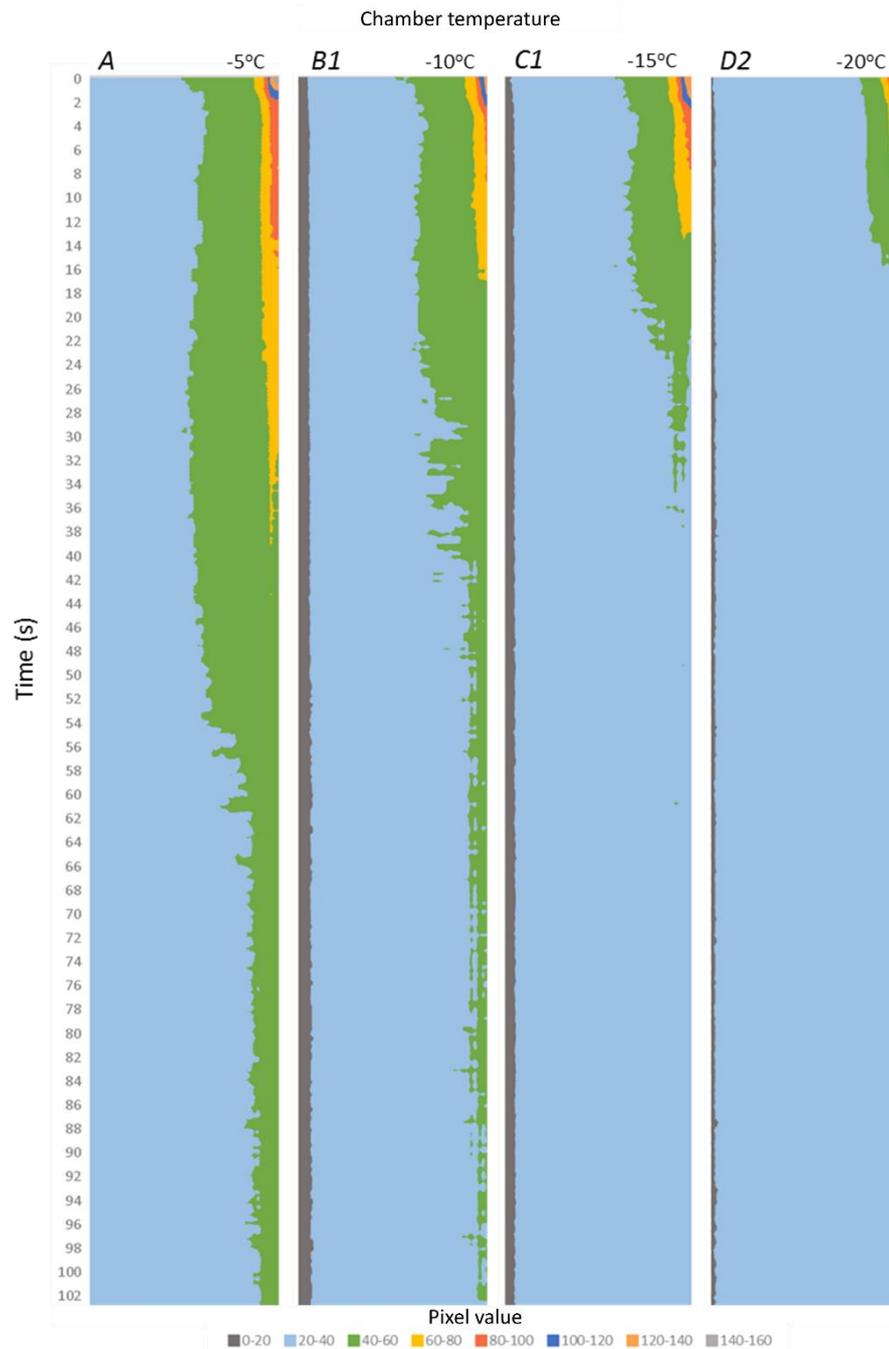
Fig. 4.35. Graphs of fluorescence intensity vs time for different chamber temperatures.

The region with intensity values ranging between 40 and 160 was used to estimate the extent to which the underlying ice-crystal structure melted after the deposition of a new layer. Its maximum depth (D_{max}) was calculated as a fraction of the overall thickness of each sample (L) and plotted against chamber temperature. As can be seen in Figure 4.36, the width of this zone, for a given printing speed, increased with increasing ambient temperature. Figure 4.37 suggests that this phenomenon can be mitigated by printing at high speeds and low nozzle temperatures. This is in agreement with observations made regarding the overall quality of a part (see Section 4.2.1), since extensive melting can cause slumping of the preceding layers.
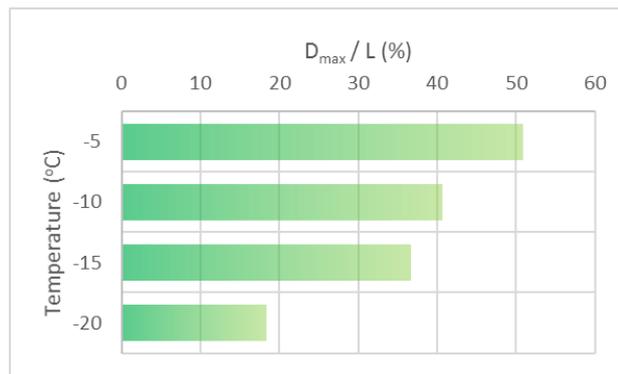
Fig. 4.36. Maximum depth of melted zone in relation to sample thickness for various chamber temperatures (speed: 400mm/min).
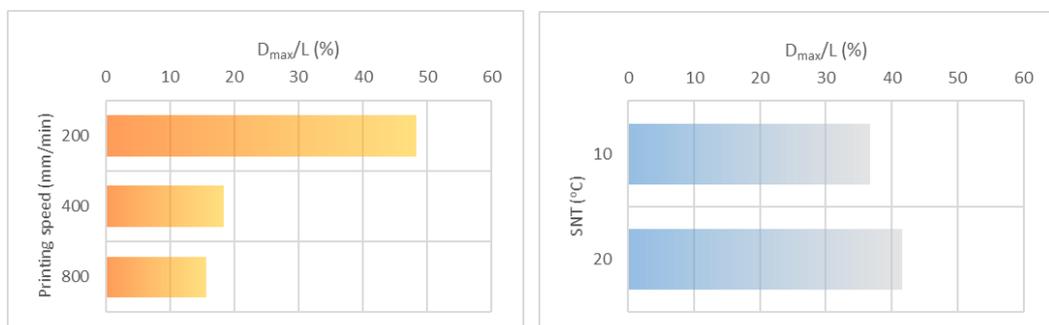
Fig. 4.37. Maximum depth of melted zone in relation to sample thickness for different printing speeds at -20°C (left) and nozzle temperatures at -15°C (right).

The experiments also provided an understanding of the crystallisation process after the deposition of a layer. To this end, the average value of the first 15 pixels, counting downwards from the newly added layer, was plotted over time (see section 4.1.5). Fluorescence intensity was expressed as a percentage between the minimum and maximum values attained in each experiment. An exponential decay with a characteristic "kink" in relation to time across all chamber temperatures can be seen in Figure 4.38.
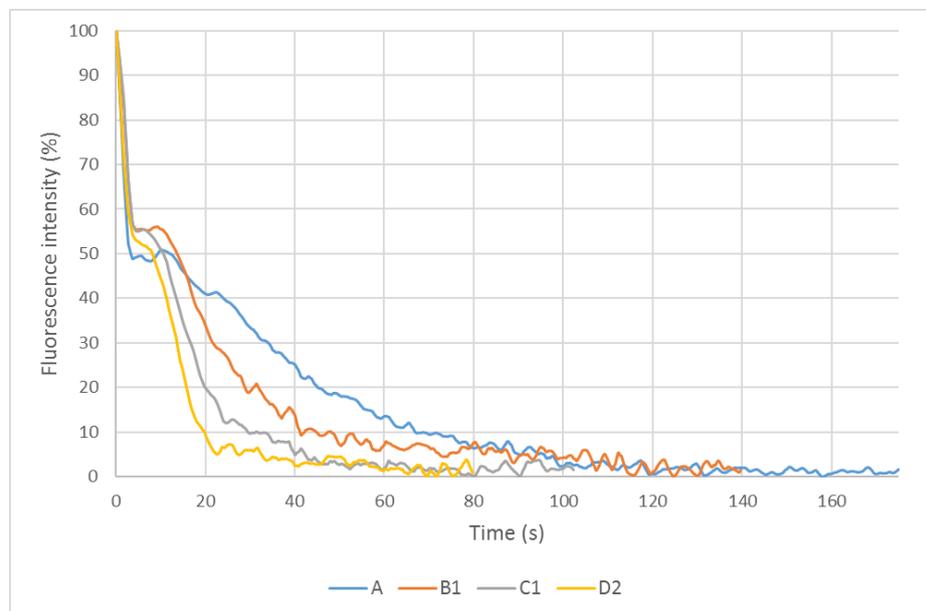
Fig. 4.38. Graph of average fluorescence intensity against time for samples printed at different chamber temperatures: -5°C (A), -10°C (B1), -15°C (C1) and -20°C (D2).

A possible reason for the sharp drop observed immediately after its deposition lies in the solubility of fluorescein, which decreases as the paste cools down. Crystallisation followed a sigmoidal profile, which is typical of phase transformations (Avrami equation, Avrami 1940). It begins with a short plateau, due to its slow initial rate and accelerates once a critical number of nuclei have

been formed. The initial slope of each curve was calculated and plotted as a function of chamber temperature. From Figure 4.39, it can be deduced that the highest freezing rate was achieved at -20°C (D2), nearly four times faster than that corresponding to -5°C (A). Furthermore, the relationship between freezing rate and temperature can be modelled as a second order polynomial. This perhaps justifies the large discrepancy in pore size distribution that exists between B1 and A, as opposed to B1 and D2.
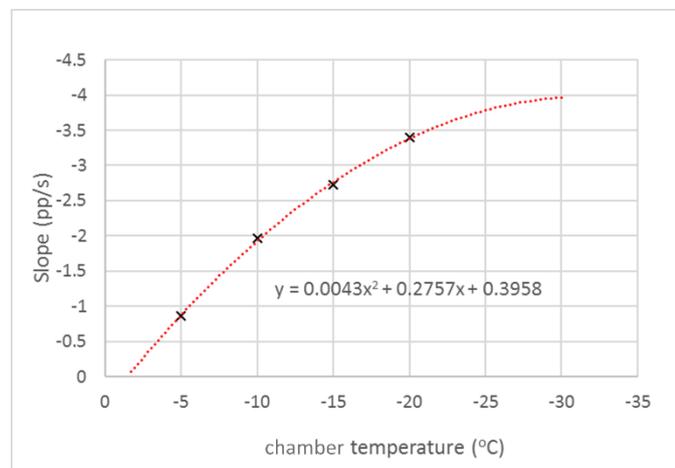
Fig. 4.39. Plot of the initial slope of fluorescence intensity curves as a function of chamber temperature.

Following a period of fast growth, crystallisation gradually ceases as the volume of available free water diminishes, causing viscosity to rise. The value of fluorescence intensity at which the paste plateaus ranged between 37.5 and 50% of its maximum value at the moment of deposition. This could be related to the amount of water that remains in an unfrozen state in the freeze-concentrated matrix. Freezing time in this context was the time elapsed between the deposition of a layer and the moment its fluorescence intensity reached a constant value (below 5% of the original). For example, crystallisation at -5°C (A) continued until an elapsed time of

90 s. In contrast, the solidification of a layer at -20°C (D2) lasted approximately 20 seconds, as can be seen in Fig. 4.40. This explains why it was not possible to fabricate specimens at -10 and -5°C without prolonging the pause after the deposition of each layer to 120 and 240 s respectively.
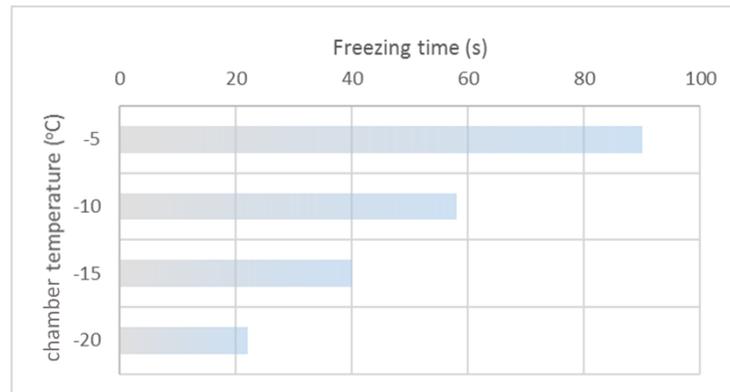
Fig. 4.40. Freezing time for various chamber temperatures.
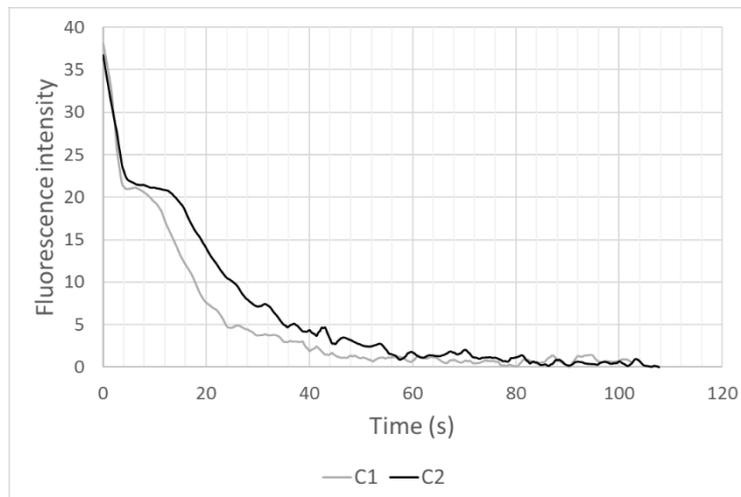
Fig. 4.41. Graph of average fluorescence intensity against time for samples printed at -15°C and different set nozzle temperatures: 10°C (C1) and 20°C (C2).

Raising the set nozzle temperature from 10 to 20°C, at an ambient temperature of -15°C, considerably slowed the sample's freezing rate for the first 20 s (see figure

4.41). This discrepancy may be responsible for differences observed in the pore distribution between *C1* and *C2,* as described in section 4.2.3.a*.*

Figure 4.42 shows that the impact of printing speed on freezing front velocity was negligible at -10ºC and -20ºC. It altered the initial cooling rate of the paste which took place within the first 10 s; the majority, however, of the freezing process remained unaffected, since the curves corresponding to different printing speeds overlap. This correlates with findings from the MIP tests, which showed no differences between their pore distributions.
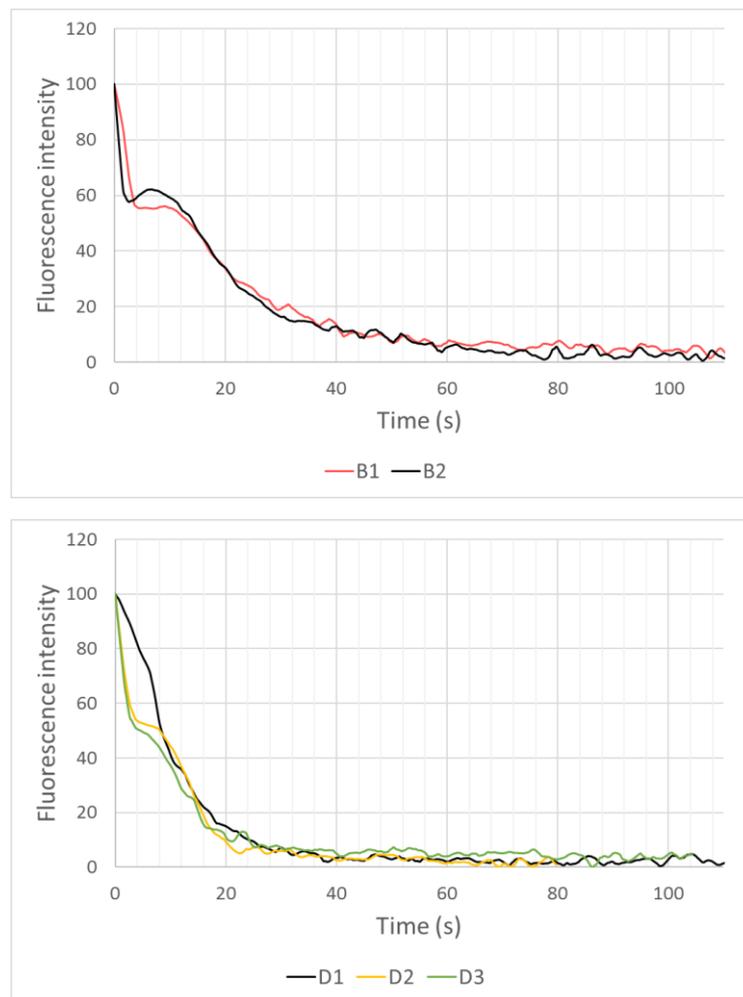
Fig. 4.42. Graphs of average fluorescence intensity vs time for specimens printed at varying speeds at -10ºC (top) and -20ºC (bottom): 200 (D1), 400 (B1, D2) and 800 mm/min (B2, D3).

4.2.4. Altering the solid/water ratio of the bioceramic paste
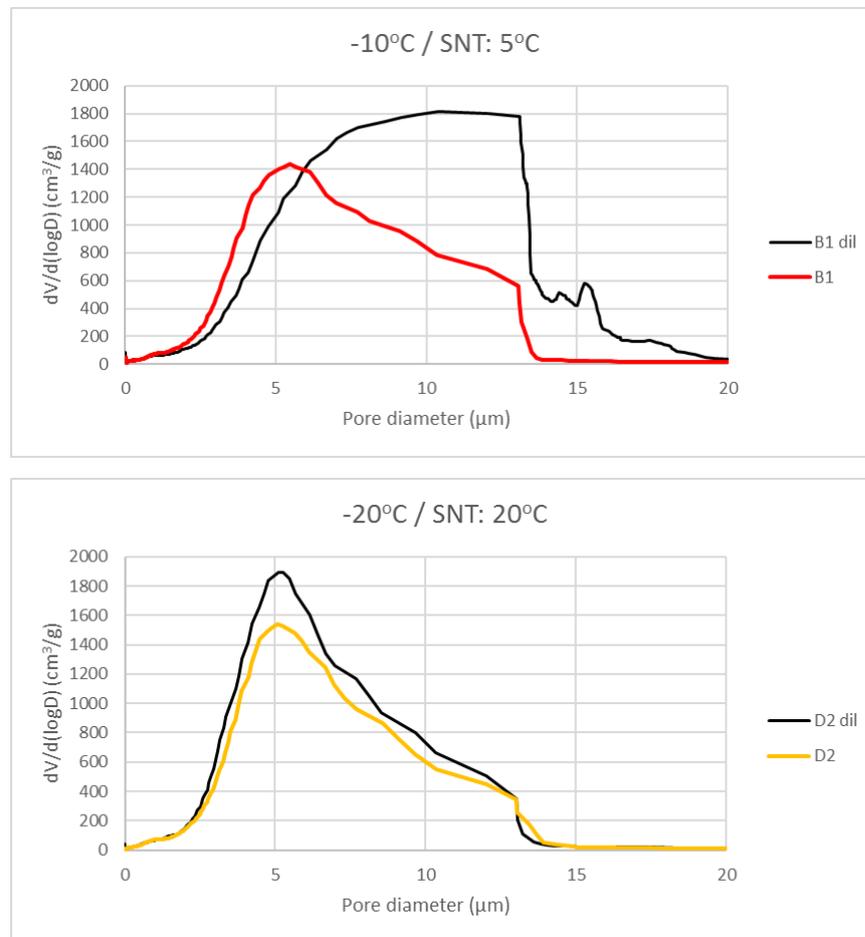
Fig. 4.43. Pore distribution for samples fabricated at -10°C (top) and -20°C (bottom).
dil refers to a paste formulation with higher water content (60% vs 55% w/w).

The graphs in Fig. 4.43 illustrate the dramatic effect that a 5% w/w difference in the paste's water content had on pore distribution. At -10°C the curve corresponding to the diluted formulation resembles that obtained at -5°C using the original formulation (see Fig. 4.31). The presence of large pores suggests that it solidified at a much slower rate in comparison to B1. This was also verified during the specimen's fabrication. It was necessary to increase the pause after the completion of each layer by 60s in order to mitigate the problem of sagging. For

the same reason, it was not possible to produce samples at -5ºC. At -20ºC on the other hand, the high freezing rate resulted in a pore distribution for the diluted formulation that closely approximates that of D2. The former appears to feature a larger proportion of pores in the 5 μm range, since its curve peaks at a higher value. It is hypothesised that this is linked to its low viscosity, which gave rise to finer microstructures.

4.2.5. μ-CT scans of hierarchical 3D lattice structures

A representation of the 3D lattices that were robocast at varying chamber temperatures is presented in Figure 4.44. They had a diameter of approximately 19.5 mm and consisted of 10 layers, each one laid in a hatching pattern configuration at different angles (0º, 45º, 90º and 135º). The μ-CT scans assisted in evaluating the overall quality of the samples in a non-destructive manner. Figure 4.45 shows the projections of each stack on the xy plane based on their average intensity. Figure 4.46 provides a comparison between a middle cross section of an idealized 3D model and its analogous cross sections in the robocast samples. Paradoxically, there was better agreement between the two at higher chamber temperatures. A small inconsistency was observed in the distance between rods that were deposited diagonally in relation to the gantry's x-y stage (45º and 135º). Their width ranged between 600 and 700 μm for samples A(-5ºC), B(-10ºC), C(-15ºC) and 600 to 800 μm for D(-20ºC). This is due to the fact that the actual layer thickness was affected by ambient temperature; It reduced from 0.39 mm at -5ºC to 0.33 mm at -20ºC. A possible reason is the contraction of the setup's mechanical

components and more specifically the lead screw that actuates the print-bed along

the z-axis.
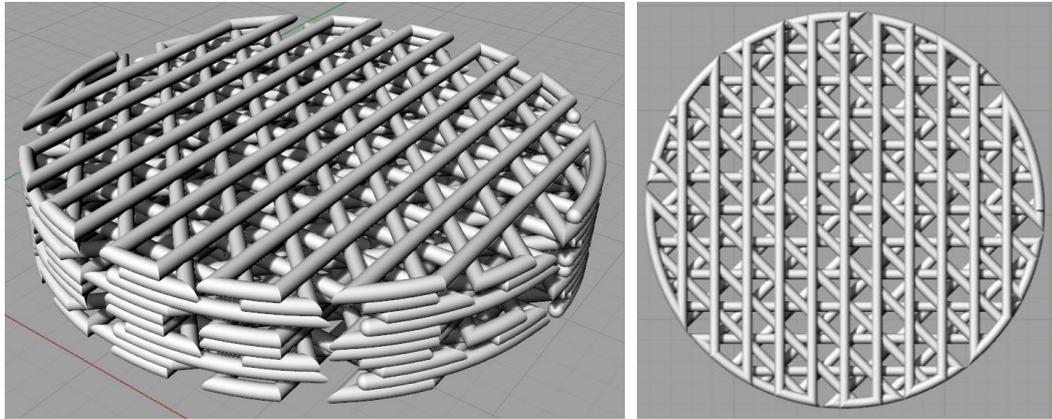
Fig. 4.44. Perspective (left) and top (right) view of the 3D model.
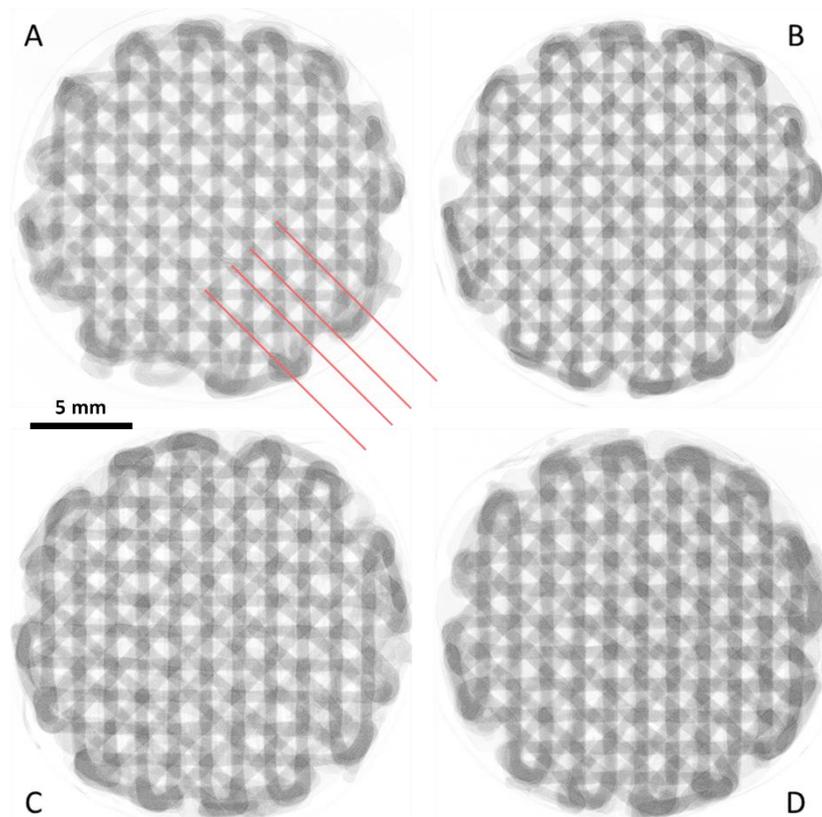
Fig. 4.45. Z-projections of μ-CT stacks for samples A(-5ºC), B(-10ºC), C(-15ºC) and D(-20ºC).
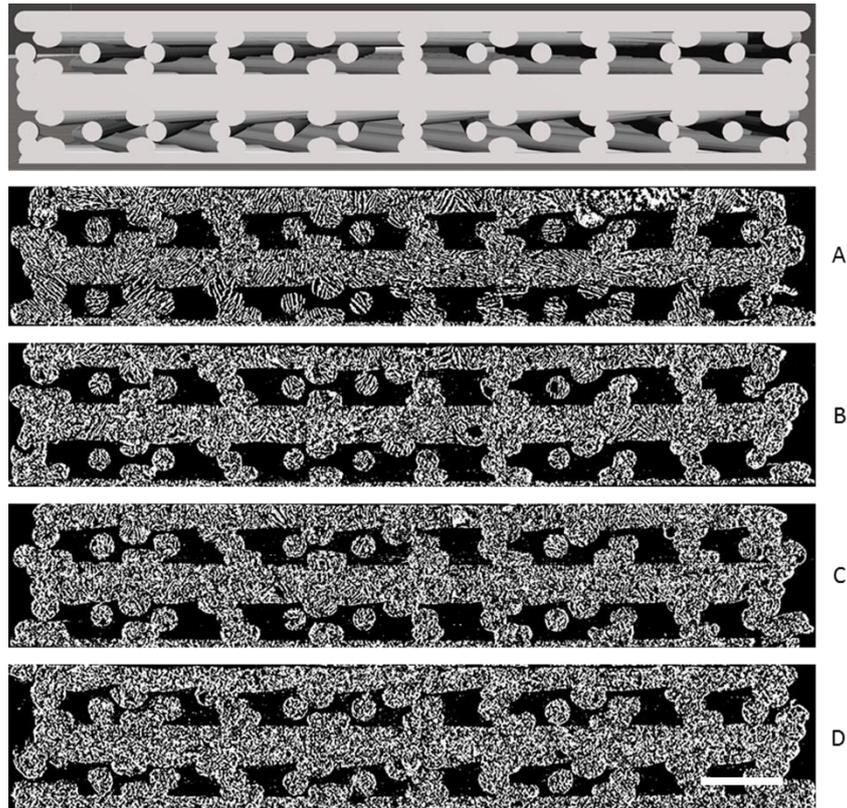
Fig. 4.46. Middle cross section of the 3D model (top) and its equivalent in the generated 3D lattice structures, scale bar: 2 mm.

Figure 4.47 illustrates the 3D volumetric reconstructions of 4.3 × 4.3 × 3.5 mm sections taken from the centre of each specimen. There was a noticeable difference between *A* and the rest of the samples; it contained randomly orientated lamellar pores, with the largest situated nearest to its base. Cross-sections on vertical planes provided a clearer picture of the microstructural features that resulted from the freezing process.
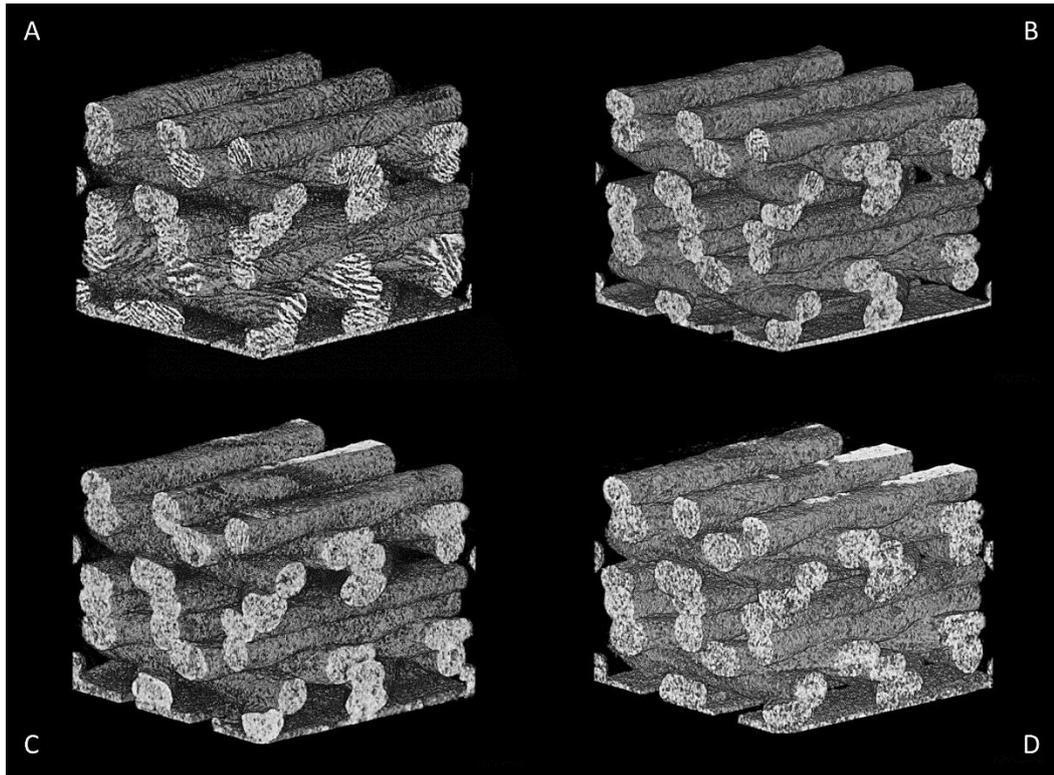
Fig. 4.47. Volumetric reconstructions of A(-5°C), B(-10°C), C(-15°C) and D(-20°C).

As can be seen in Fig. 4.48, printing at -20°C (*D*) resulted in a highly homogeneous cellular microstructure consisting of pores in the range of 30 to 100 μm. At -15°C (*C*), lamellar pores on average 200 μm long could be distinguished primarily in areas that span across gaps. This is because they froze at a slower rate in comparison to those that are were contact with previously deposited layers.
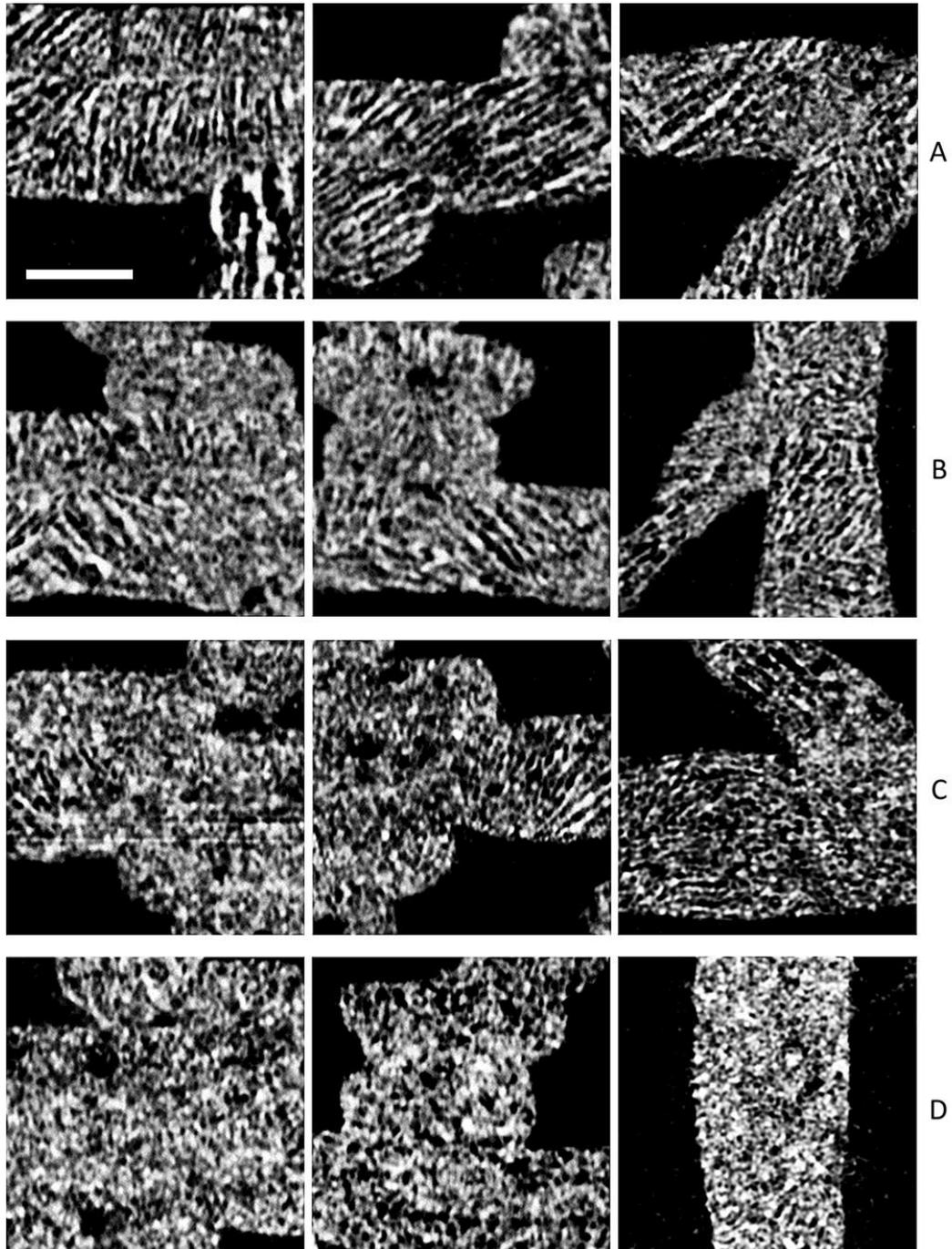
Fig. 4.48. Vertical (1st and 2nd columns) and horizontal (3rd column) cross-sections of A(-5°C), B(-10°C), C(-15°C) and D(-20°C). The scale bar corresponds to 500 µm.

Similar observations were made for *B*, which was printed at -10°C, the key difference being an increase in the average spacing of the lamellae from 25 to 40 µm. At higher chamber temperatures, the sample's micromorphology was characterised almost entirely by lamellar pores with a high degree of local

alignment and length that ranged between 50 and 300 µm. Figure 4.49 also suggests that the first three layers in *A* solidified significantly slower in comparison to succeeding layers, as they featured some exceptionally large pores up to 500 µm long and 100 µm wide.
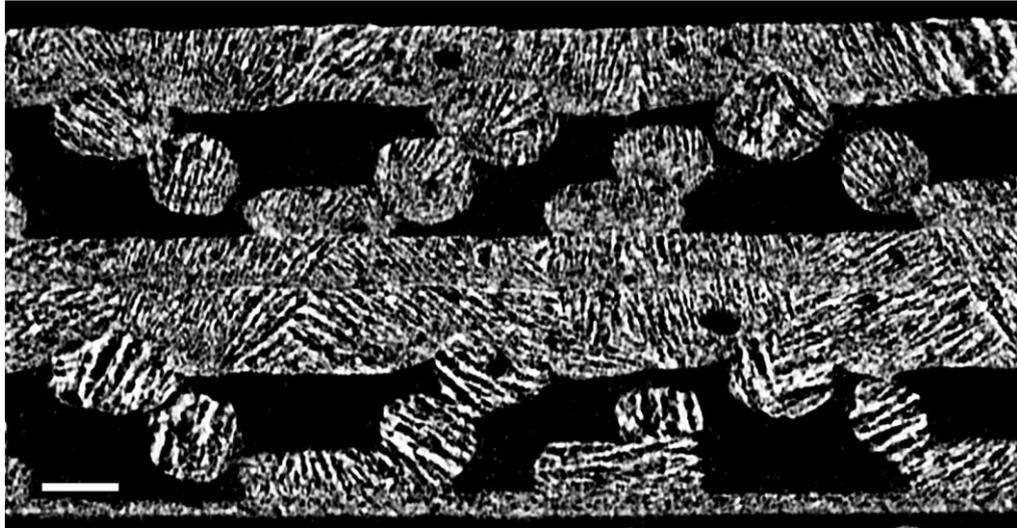
Fig. 4.49. Vertical cross section of sample A (-5°C) (scale bar corresponds to 500 µm).

Furthermore, the µ-CT scans revealed that ice-crystal growth occurred epitaxially; its direction in each layer was dictated to some extent by the underlying ice-crystal structure at the points of contact with the preceding layer. This phenomenon was more pronounced at -5°C, as it favoured the formation of more ordered particle assemblies. A remarkable characteristic of these assemblies was the presence of symmetrical patterns of growth, similar to those presented in Figure 4.50 and 4.51. It is hypothesised that the dispensing toolpath geometry, in conjunction with epitaxy and the localised physical conditions were the key factors contributing to the emergence of these patterns. In these images, one can notice that the overall shape of the selected cross-sections is symmetrical (a vertical yellow dashed line

represents their axes of symmetry). The ice-crystals located towards the base of the sample are also mirrored about the same axis, establishing bilaterally a common starting point for the ice structure that grew in each successive layer. These two conditions, along with the fact that both sides were subjected to similar environmental conditions due to their proximity, are thought to have given rise to nearly identical microstructures mirrored along the z-axis.
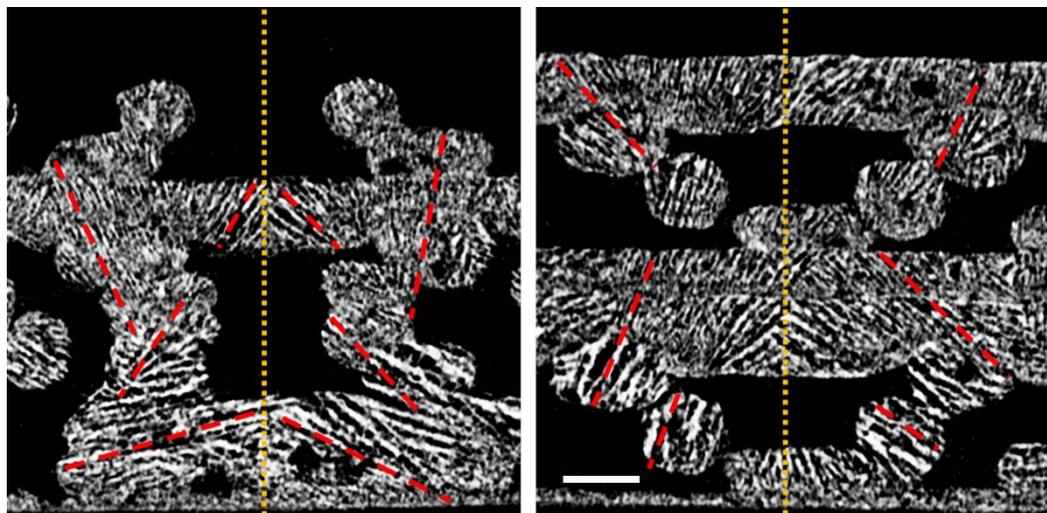
Fig. 4.50. Symmetrical patterns in pore structure as seen in vertical cross-sections (the red dashed lines indicate the lamellar orientation), scale bar: 500 μm.

Furthermore, it appears that the direction of growth can change depending on how the filaments are positioned in 3D space. For example, in Fig. 4.51 the filaments are stacked in an arch-like arrangement. A closer look reveals that the orientation of their lamellar pores also follows a similar pattern; It is worth noting the analogy between this microstructure and the arch-like trabecular structure observed in the trabecular section of the upper human femur. It is thanks to this architecture that the femur is capable of withstanding high compressive loads (Rudman et al., 2006).

The ability of LDM to replicate such structures, could be a valuable feature for improving the toughness of bioceramic scaffolds.
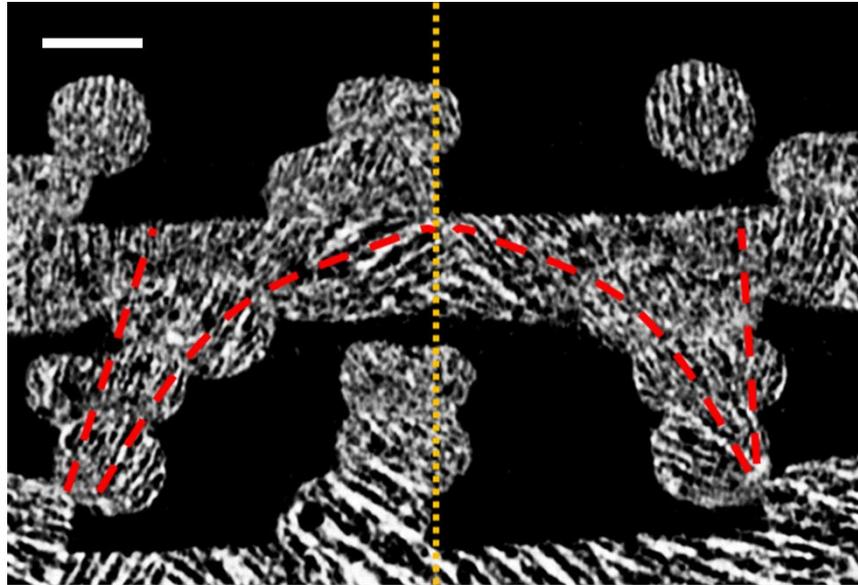
Fig. 4.51. Symmetrical arch-like arrangement in the 3D printed sample, scale bar: 500 µm (top) and its analogy with the trabecular architecture of human upper femur (bottom).

4.3. Discussion

These experiments demonstrated that the overall quality of a part diminishes below a printing speed of 200 mm/min for a 0.5mm nozzle. Maintaining a low nozzle temperature can also significantly improve the performance of the LDM process. Another important parameter is the duration of pause between

dispensing cycles, which should be long enough for each layer to solidify before a new layer is added.

The findings are summarised in a diagram, presented in Fig. 4.52. The temperature inside the chamber and water content appear to have the most marked effect on freezing rate, which in turn impacts on pore morphology. Ordered micro-architectures comprising lamellar pores with a high degree of alignment were obtained at -5°C (lowest freezing rate attained). Their direction was dictated by the ice structure in preceding layers (epitaxy) in conjunction with the temperature gradients that emerged following each layer's deposition. This places an emphasis upon both ice-crystal orientation in the initial layer and the toolpath used for the construction of the object. On the contrary, low ambient temperatures (e.g. -20°C) yielded cellular pores of reduced size that displayed a higher degree of uniformity. At intermediate temperatures, pore shape varied between cellular and lamellar. The former type was observed in areas of a filament that made contact with its underlying layer. This was due to the faster dissipation of heat in comparison to segments that spanned gaps. A slight increase in water content significantly decreased the paste's freezing rate at a given temperature, giving rise to lamellar structures. This leads to the conclusion that altering the paste's solid-to-water ratio whilst deposition modelling takes place may be the most effective strategy for introducing functional gradients in a printed part. The remaining processing parameters influenced the microstructural outcome of LDM to a lesser extent: low printing speeds, high nozzle temperatures and short pauses between dispensing cycles, all contributed to greater heterogeneities and larger average pore diameters.
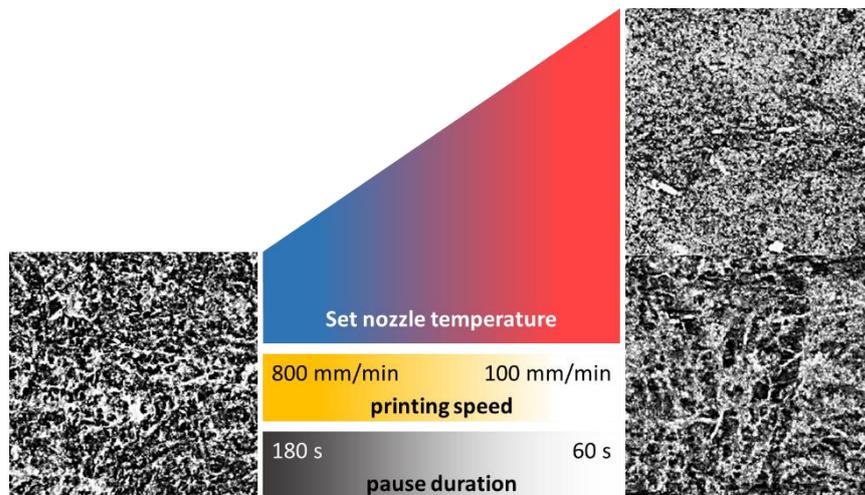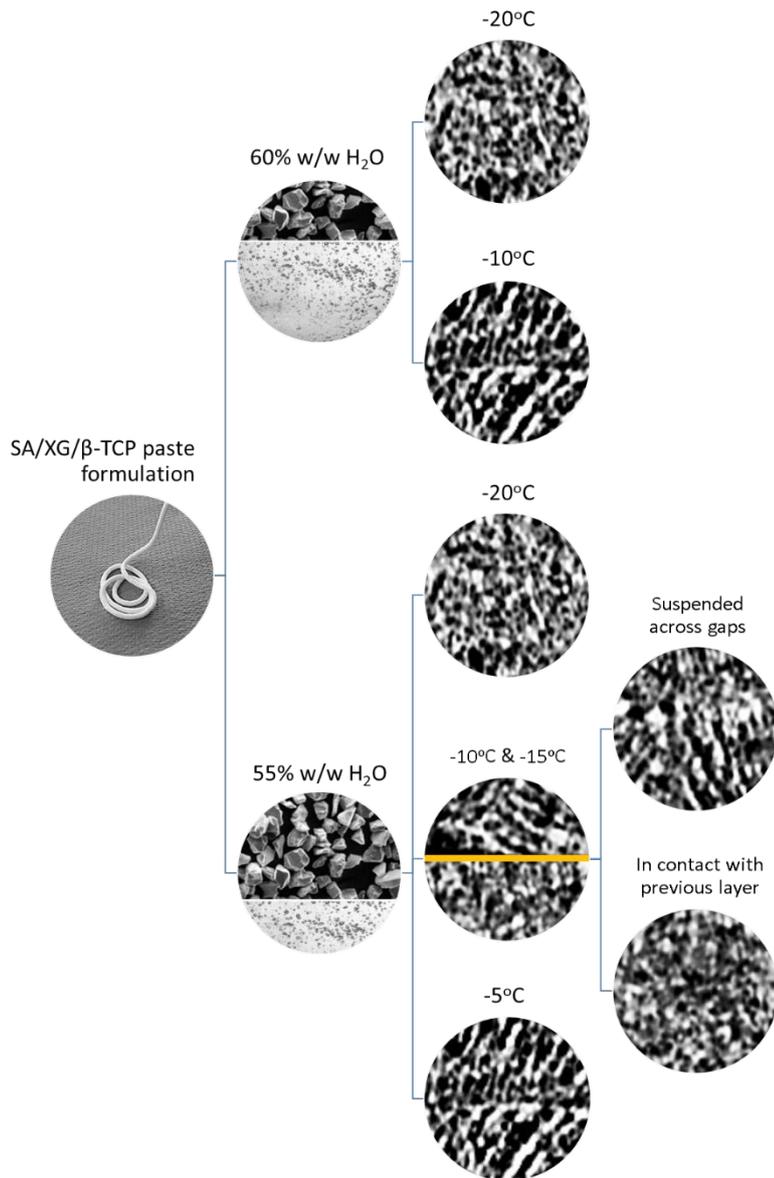
Fig.4.52. Diagram illustrating the effect of selected parameters on the microstructure of printed parts.

Chapter 5
Robocasting of flexible 2D lattices featuring hollow struts

An alternative method was investigated for modifying the microstructure of a robocast bioceramic scaffold based on solvent diffusion and evaporation. This novel fabrication route can produce flexible 2D lattices with well-defined architecture that comprise hollow struts. This chapter begins with a brief overview of the processes currently available for incorporating a hollow-tube construction in additively manufactured lattice structures. It proceeds with a description of the main steps and materials involved in the proposed method. The processing and material parameters that determine its structural outcome are also examined, focusing primarily on paste rheology and temperature of heat treatment. Finally, it explores the idea of manipulating flexible green bodies in the form of planar lattices to achieve various configurations.

5.1. Additive Manufacturing of hollow-tube lattice structures

Hollow struts are a highly desirable feature for synthetic hard tissue substitutes. They distribute oxygen and nutrients to the cells more efficiently than their solid counterparts, improving vascularization and new bone formation in the centre of scaffolds (Luo et al., 2015). In addition, cellular materials with hollow struts exhibit higher compressive strengths than equivalent structures with solid members thanks to their greater resistance to plastic buckling (Karam and Gibson, 1995). So far, one can distinguish between three main fabrication routes:

Fig. 5.1. Single-step robocasting of hollow-tube lattice scaffolds based on concentrated alginate pastes (Source: Luo et al. 2013).

- The first employs a nozzle tip, specifically designed to extrude filaments with tubular profiles (see Figure 5.1). In its most simple configuration, it comprises a stainless steel right angle nozzle positioned inside a larger plastic conical nozzle (Luo et al., 2013). Hollow beads, however, are susceptible to structural collapse. In order for them to withstand the weight of overlying layers during robocasting, a fine tuning of the material's rheology and drying kinetics is necessary. This has been addressed to some

extent by printing in a liquid medium, which provides buoyancy (see Section 2.2) (Schlordt et al., 2013). Another disadvantage is that the cavities in points of intersection between layers are not connected, resulting into a linear instead of a planar or three-dimensional network of interconnected channels.

- Another strategy involves the co-extrusion of two materials with different viscosity followed by selective dissolution of the core (Moroni et al., 2006). Moon et al. went one step further by introducing micro-porosity in a tubular framework. This was achieved through freeze-drying the dendrites that grew within the alumina/camphene shell of co-extruded rods. Porosity could also be controlled through altering the alumina content of the ceramic slurry (Moon et al., 2015).

Fig. 5.2. Co-extrusion combined with freeze-drying. Schematic diagram of the process (left) and micrographs of a hollow-tube lattice at different magnification levels (Source: Moon et al. 2015).

- Finally, a technique that can accomplish exceptionally high resolutions combines Stereolithography with sacrificial templating. Following this

strategy, Zheng et al. 3D printed highly complex polymeric micro-lattices that were coated with alumina via atomic layer deposition. Subsequently, the template was thermally decomposed, leaving behind a hollow-tube framework that deforms elastically and exhibits a linear relationship between stiffness and density (Zheng et al., 2014).

Fig. 5.3. Mechanism of hollow shell formation in droplets containing suspended solids (Source: Handscomb et al. 2009).

This chapter introduces an alternative approach to fabricating such structures, one in which the extruded filament itself assembles into a hollow-tube configuration after it has been deposited. The technique employs the mechanism of hollow shell formation in drying droplets of colloidal suspensions (see Fig. 5.3). This is achieved by heating the extrusion rapidly, which forms a "skin" as water evaporates from its surface. Its radius decreases until the point it reaches a critical solids volume fraction, at which a rigid shell starts to grow inwards. Capillary forces arise as water that is entrapped in its core diffuses through the thickening shell; the lower its permeability the larger the pressure differential. This can cause the shell to buckle

and collapse, depending on its stiffness. At the same time, a vapour bubble grows in its centre, supplied with drying air from the surrounding environment (Handscomb et al., 2009). The air enters the bubble through the widest pores, as they drain faster in comparison to narrow menisci, while particles pile up on the receding air-water interface (Tsapis et al., 2005).

5.2. Materials

β-TCP powder (1-5 µm) was used unprocessed, as supplied by Sigma-Aldrich. Food grade Sodium Alginate was supplied by Special Ingredients Ltd. The reader can refer to Sections 1.1.2 and 3.2 respectively for more information regarding these materials.

A cellulose nano-fibril (CNF) suspension with a mean diameter of 25 -30 nm and a solids content of 1.56% (w/w) was supplied by the Technical Research Centre of Finland (VTT). Cellulose is a polydispersed linear polymer of poly-β(1,4)-D-glucose units. It can be isolated from the cell walls of plants in the form of nano-fibrils, using a combination of chemical and mechanical methods. It has received a lot of interest recently as a reinforcement in polymer composites due to its high strength and stiffness (Young Modulus of 150 GPa). Other attractive attributes include its low weight, high surface area, biodegradability and abundance. Cellulose nano-fibrils interact strongly with each other through hydrogen bonds. This results in the formation of a percolating network of fibrillar aggregates, which further enhances the mechanical properties of CNF-reinforced composites. The reader can refer to

Kalia et al. (2011) and Qiu & Hu (2013) for an overview of the main applications in the areas of medicine, tissue engineering, electronics and smart materials.

The combination of nano-crystalline (NCC) and fibrillar (NFC) cellulose with SA has been reported in bibliography. In a study conducted by Huq et al. (2012), the incorporation of NCC in alginate-based films resulted in an increase of their tensile strength by up to 37%. This is attributed to their similar molecular structure, which gives rise to strong interfacial bonds between the two types of polysaccharides. Lin et al. (2012) cross-linked freeze-dried mixtures of alginate and oxidised cellulose in a calcium chloride solution to produce sponges with enhanced mechanical strength, high porosity and excellent water absorption and retention. Another study established that CNF can increase the tensile modulus of alginate-based films by almost 5 times, as well as reduce their swelling and water solubility. The biodegradation rate of these nano-composites can be controlled by altering their CNF content (Deepa et al. 2016).

5.3. Methods

5.3.1. Paste Preparation

First, SA and TCP were dry mixed, followed by the addition of a cellulose nano-fibril suspension. The mixture was homogenised with a mortar and pestle and sieved through a 62 µm mesh. It was then transferred into syringes for manual extrusion or robocasting.

5.3.2. Experimental procedure

The factors that influence the transformation of a filament to a hollow-tube upon heating are summarised below:

- Sodium Alginate content

- CNF content

- Solid/water ratio of the paste formulation

- Filament diameter

- Type of substrate

- Heating method and temperature

The effect of each parameter was studied independently, in an effort to optimise the process for robocasting planar hollow-tube lattice structures. To this end, filaments of varying diameter and composition were manually extruded on microscope slides and dried at different temperatures in a convection oven. Microwaves and IR radiation were also used while exploring alternative methods of heating. Several cross-sections (6 in average) from each specimen where imaged using optical microscopy. ImageJ was employed for extracting information regarding the surface area of the cavity in relation to the overall surface area of the dried hollow-tubes (termed *void ratio*), as an indirect measurement of shell thickness. Their borders were delineated manually with a polyline, as shown in Fig. 5.4.
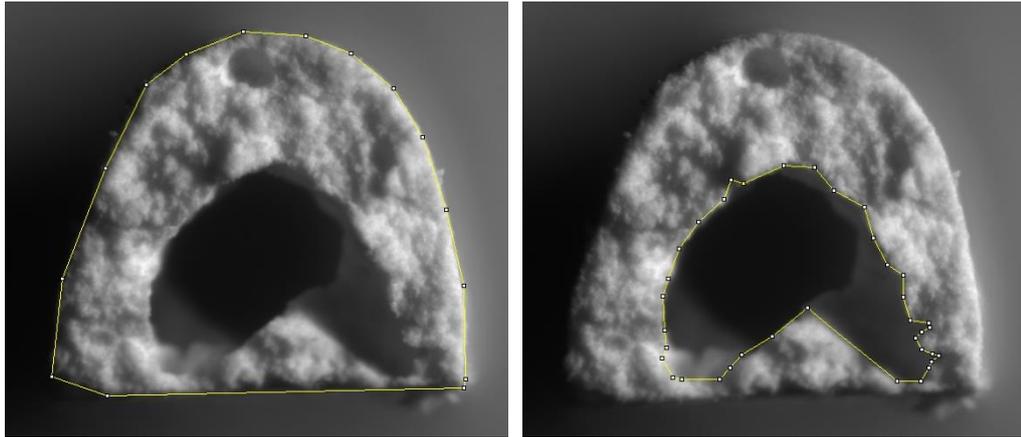
Fig. 5.4. Manual tracing of the cross-sectional area (left) and cavity (right) with ImageJ.

Oscillatory rheology tests were conducted in order to establish a link between hollow-tube formation and the rheological behaviour of bioceramic paste formulations with varying sodium alginate content. Paste samples were subjected to increasing levels of oscillating frequency ranging from 0.1 to 150 rad/s at a torque of 50 μN·m.
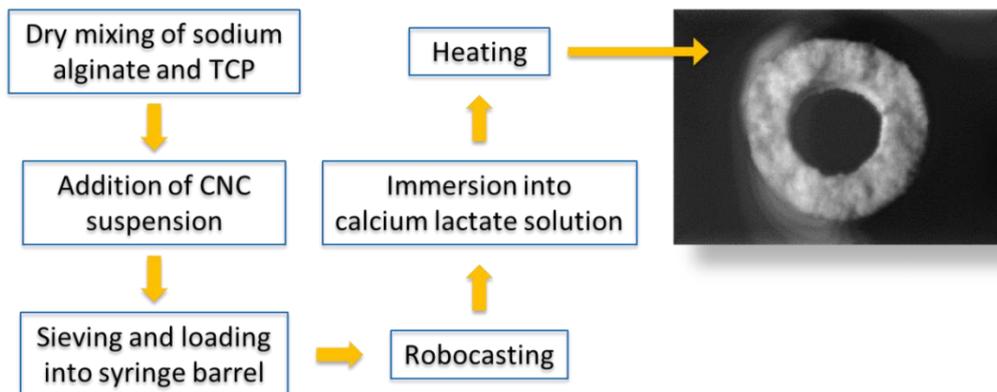
Fig. 5.5. Flow chart of the proposed process for manufacturing scaffolds with hollow struts.

A flow chart of the process is illustrated in Fig. 5.5. As a proof-of-concept, a planar lattice was robocast with a 1.6 mm diameter nozzle tip (see Fig. 5.6A), using the additive manufacturing system described in Section 3.3 (3 bar inlet pressure and

printing speed of 150 mm/min). The paste consisted of 3% (w/w) SA and a solid/water ratio of 2:3. In this case, the aqueous phase in the mixtures is the CNF suspension. The surface of the lattice was crosslinked through immersion in a calcium lactate solution (1% w/w) for 60s (Fig. 5.6B), followed by rinsing with distilled water. It was assumed that cross-linking increased the stiffness of the shell, an important factor in the formation of hollow tubes. The sample was cut along the edges (Fig. 5.6C) and subsequently heated for 60 s on an aluminium mesh (Fig. 5.6D), placed between two infrared lamps (500W) 45 mm apart. Trimming the edges ensured a uniform shrinkage, thus preventing the formation of cracks on the cross-linked surface from pressure build-up. The setup can be seen in Fig. 5.7. Finally, it was cross-sectioned and imaged for qualitative assessment.
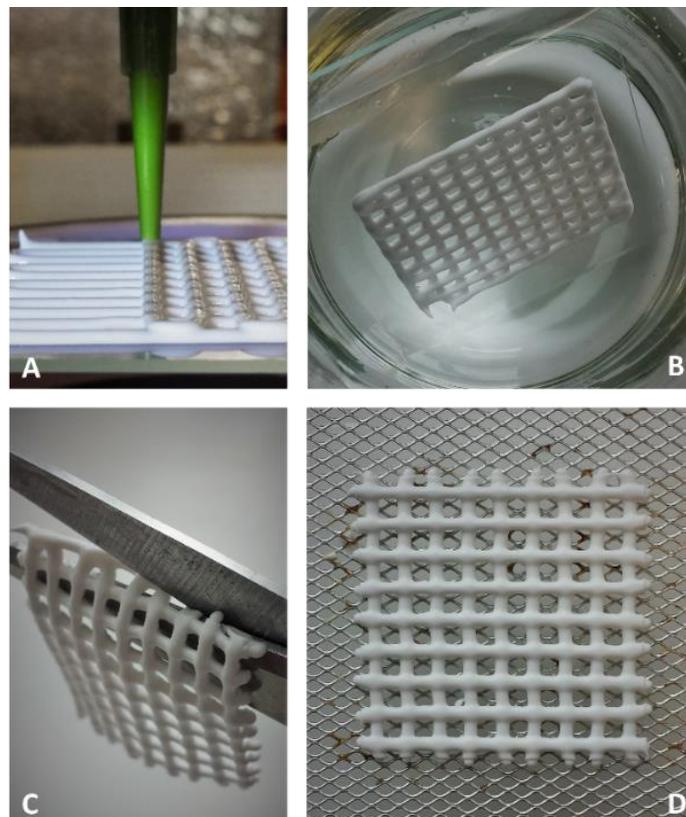
Fig. 5.6. Fabrication steps for planar hollow-tube lattices: robocasting (A), cross-linking (B), trimming (C), infrared heating on aluminium mesh (D).

163
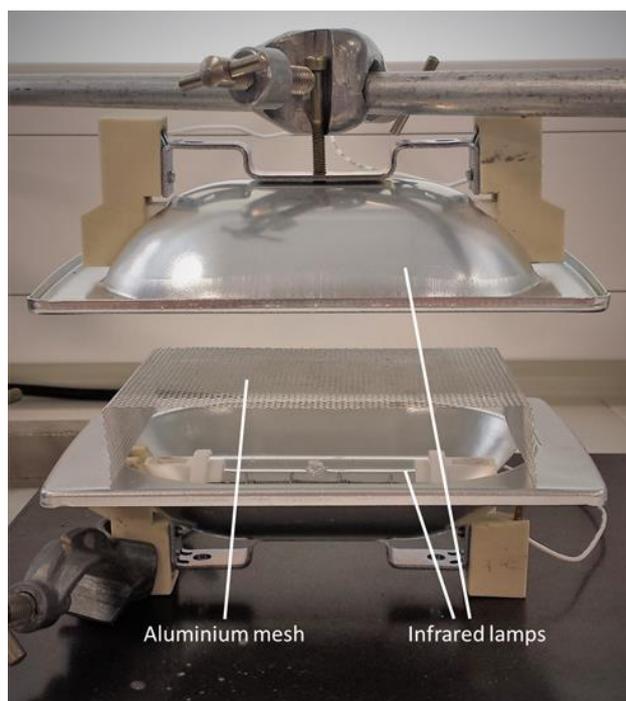
Fig. 5.7. Infrared heating setup.

Crosslinking of the paste in a Ca^{2+}-rich solution results in a flexible particle-reinforced gel that can be manipulated and shaped to the required configuration. The concept of printing origami structures was reported for the first time by Ahn et al. (2009). The flexible lattice in this case was manipulated as the solvent slowly evaporated. Instead, the CNF-reinforced ink can be re-wetted as many times as required. A number of planar lattices with 40% and 50% solids were robocast using a nozzle tip of 580 μm nominal diameter. They were immersed for 120s in 1% (w/w) $CaCl_2$ solution, rolled into cylinders and left to dry overnight. They were sintered with the following program: the temperature was ramped up to 600°C at a rate of 100°C/h and held for 30 minutes to burn away the organic phase. Subsequently, the temperature was increased to 1260°C at a rate of 600°C/h, where it was held for two hours. Cooling was natural (cooling down of the furnace). The degree of shrinkage was measured before and after crosslinking and sintering.
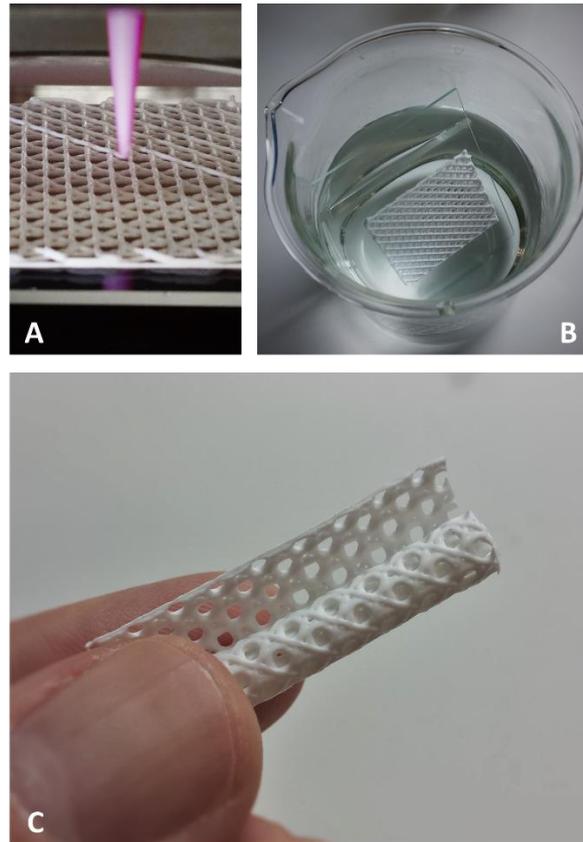
Fig. 5.8. Main fabrication steps for flexible β-TCP/SA/CNF composite scaffolds: robocasting (A), cross-linking (B), shaping through rolling or folding (C).

5.4. Results

5.4.1. The effect of selected parameters on hollow-tube formation

5.4.1.a. Sodium Alginate content

Figures 5.9 and 5.10 illustrate the effect of SA content on hollow-tube formation at 150°C and 250°C respectively. The solid loading of the paste for this series of experiments was 40% w/w. For filaments heated at 150°C, void ratio attained its maximum value at a concentration of 3% (w/w) across all nozzle sizes. At 250°C, it shifted slightly towards higher concentrations as nozzle size increased. The formation of hollow-tubes was not possible without the presence of alginate, as Fig. 5.11 suggests.
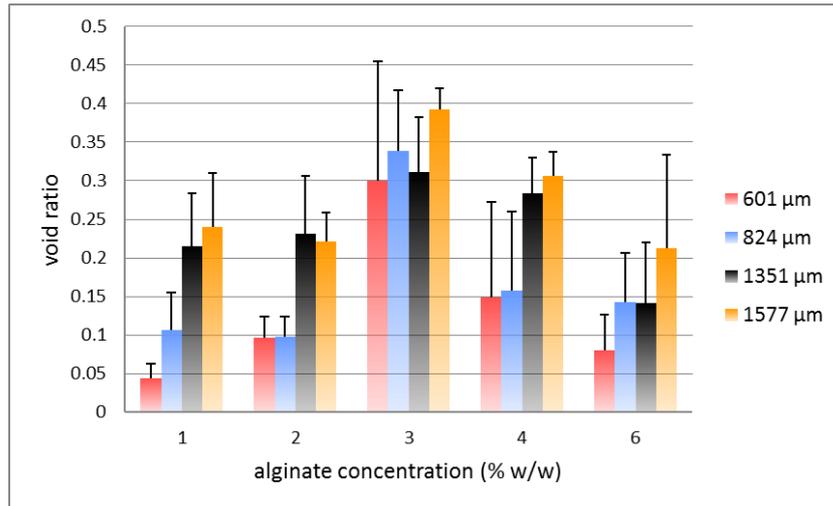
Fig. 5.9. Void ratio for specimens of varying alginate concentrations heated at 150°C.
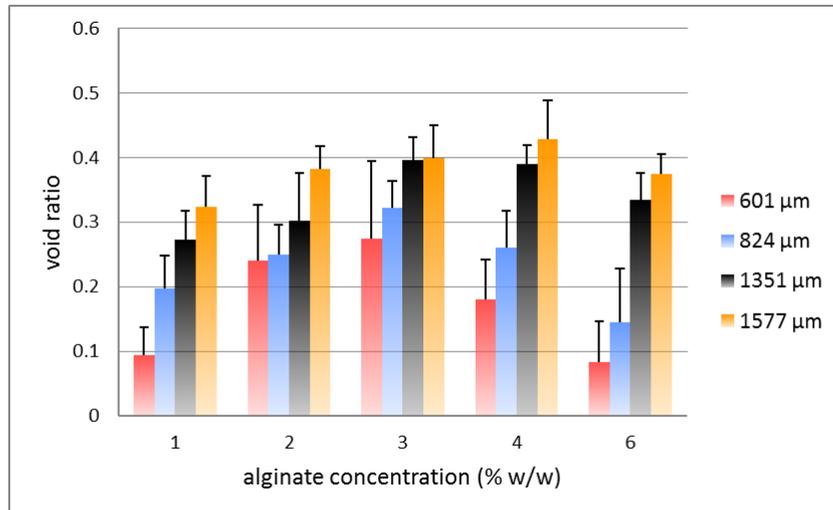
Fig. 5.10. Void ratio for specimens of varying alginate concentrations heated at 250°C.
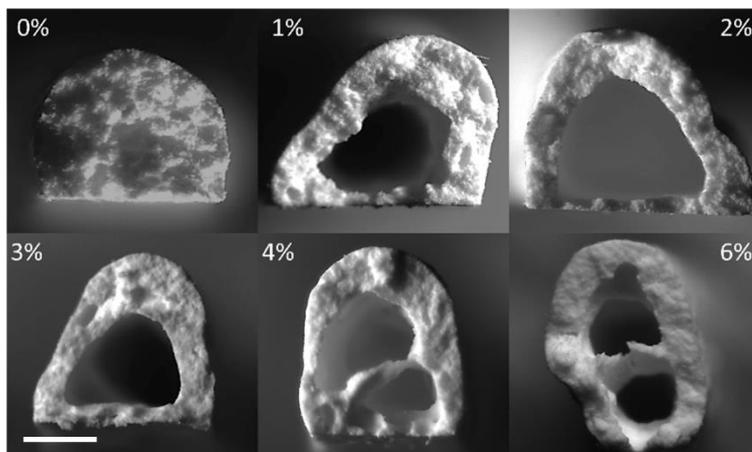
Fig. 5.11. Micrographs of cross-sections obtained from specimens of varying SA content, extruded through a 1577 µm nozzle tip and heated at 250°C, scale bar: 500 µm.

The amount of SA together with solid loading are the major factors regulating the viscosity of the paste. It appears that above a certain viscosity, the formation of hollow-tubes can be hindered. While high viscosity enhances the stiffness of the shell, it can impact on the mobility of particles that pile up on the receding air-water interface. Additionally, high polymer content reduces the permeability of the structure, impeding the entry of air from the surrounding environment to the vapour bubble in the filament's core. This may result in an increase of the evaporation-induced capillary forces, causing the shell to buckle. This is confirmed by the presence of multiple pores and the considerable deformation of the shell in samples with 4 and 6% alginate (see Fig. 5.11).

5.4.1.b. Filament diameter

Fig. 5.9 and 5.10 also suggest that, at a given heating temperature, void ratio increases with filament diameter. The thinner the filament, the more rapid the temperature rise in its core, resulting in accelerated growth of the vapour bubble. However, this impacts on the amount of time required for the complete evaporation of the solvent, which is significantly reduced. As a result, the air-water interface moves faster but ceases sooner in comparison to thicker filaments. Furthermore, the degree of shrinkage is more sensitive to variations in alginate content amongst filaments of larger diameter, as evidenced in Fig 5.12. This is partially due to the low thickness-to-span ratio of the resulting shell, which renders it susceptible to buckling. The observed increase in cross-sectional surface area with polymer concentration was thought to be associated with enhanced stiffness.
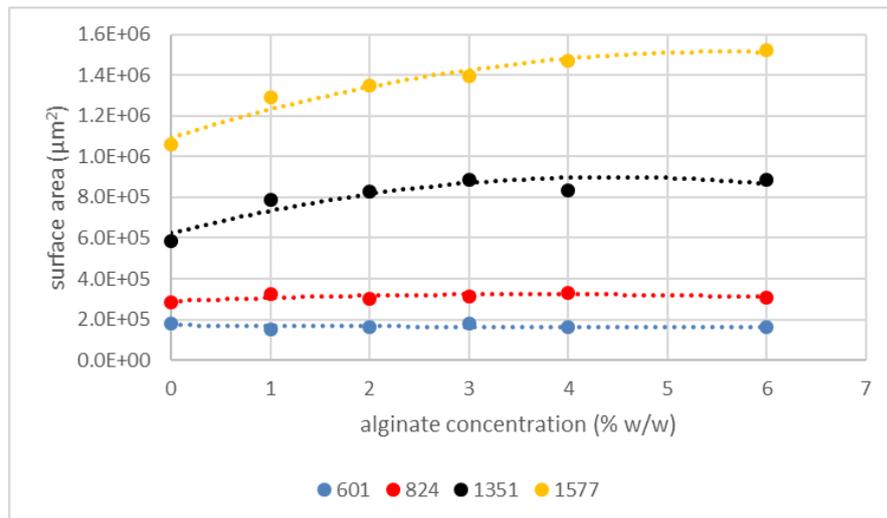
Fig. 5.12. Cross-sectional surface area for filaments of varying SA content, heated at 250°C.

5.4.1.c. Type of substrate

As can be seen in Fig. 5.13, replacing the glass slide with a fine aluminium mesh resulted in circular cross-sections, as opposed to the bell-shaped profiles that were obtained from the initial experiments (Fig. 5.11). There was no noticeable difference between the two groups in terms of their average void ratio. Minimising the area that is in contact with the substrate provides a more uniform evaporation rate, as most of the filament's surface is subjected to the same environmental conditions (convective air drying). In contrast, when the filament is placed on a glass slide, heat is transferred to its flat lower section via conduction, imparting a non-uniform temperature distribution. Furthermore, the glass acts as a barrier to water evaporation and diffusion, which results in slower drying rates in comparison to areas exposed to hot air. This explains the significant warping that was observed, predominantly amongst specimens of low solid loading.
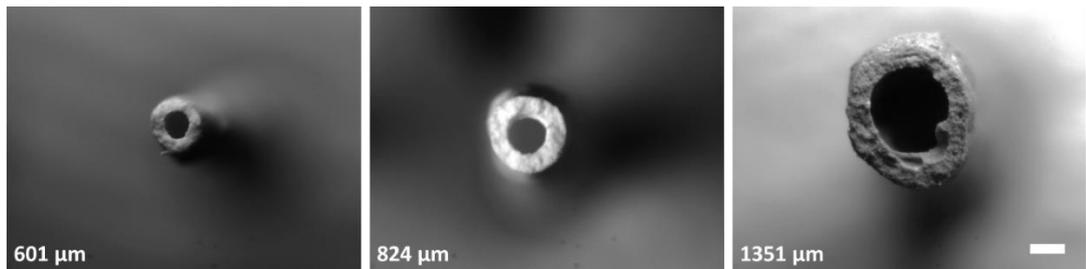
Fig. 5.13. Cross-sections of hollow-tubes of varying diameter produced by heating at 250°C on an aluminium mesh (3% SA, 40% S/W ratio), scale bar = 300 μm.

5.4.1.d. Heating method and temperature

Heating temperature determines the solvent's evaporation rate and consequently, the time required for a rigid shell to form. As can be seen in Fig. 5.14, specimens heated at 250°C displayed a void ratio that was consistently higher or at least equal to that obtained at 150°C, across all tested SA concentrations. It can be deduced that a high evaporation rate, combined with the right rheology, can minimise shell thickness for a given solid loading.
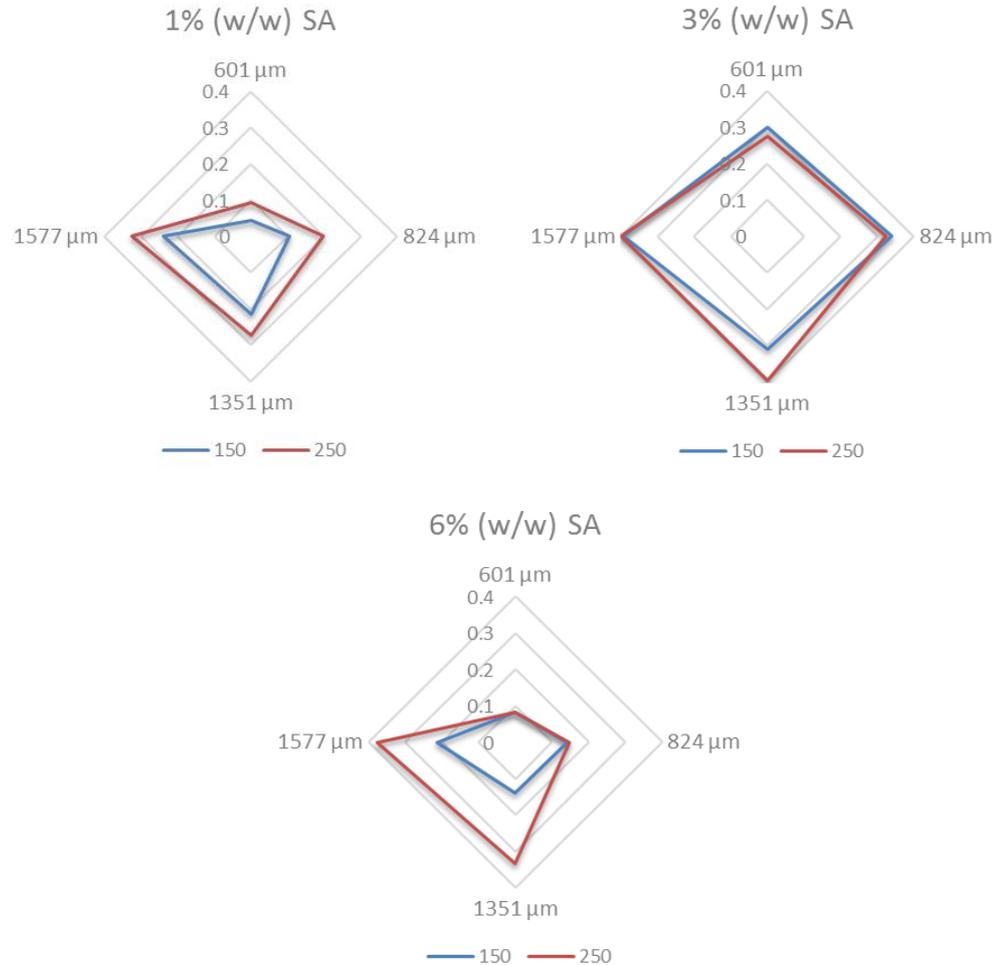
Fig. 5.14. Radar graph of void ratio against diameter for filaments of varying alginate content, heated at 150°C and 250°C.

Microwave heating produced highly porous filaments without a defined hollow-tube architecture. As can be seen in Fig. 5.15, the pores were interconnected and randomly distributed with a large variation in size. Microwaves (750 W) penetrate through the sample supplying an excessive amount of energy in a very short time scale, creating vapour bubbles throughout the entire volume of the filament. The result was very different from convection heating, which imparts a well-controlled radial diffusion of water, thanks to the large temperature differential between the surface and core.
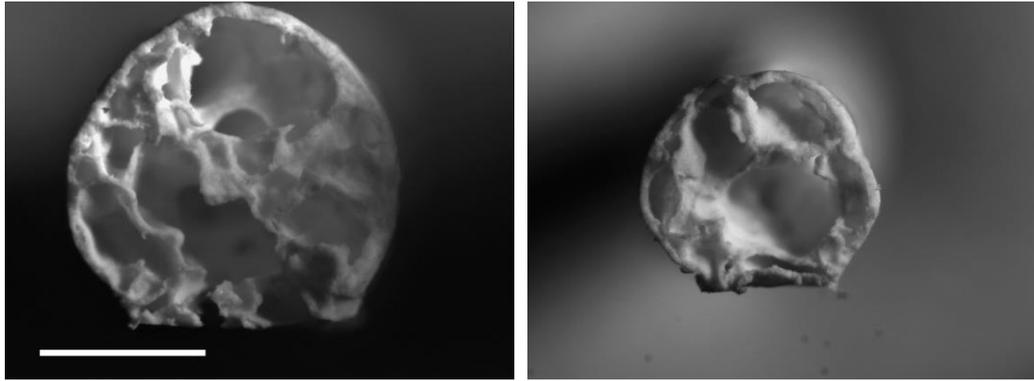
Fig. 5.15. Micrographs showing cross-sections of microwave-heated specimens, extruded through a 1577 μm (left) and 1351 μm (right) nozzle tip (6% w/w SA), scale bar: 1 mm.

Infrared lamps (2×500W), on the other hand, allowed for a precise control of the heating rate and duration of the process, the outcome of which displayed great similarity with convection heating (see Fig. 5.16). These two features make IR heating highly suitable for manufacturing hollow-tube lattice structures.
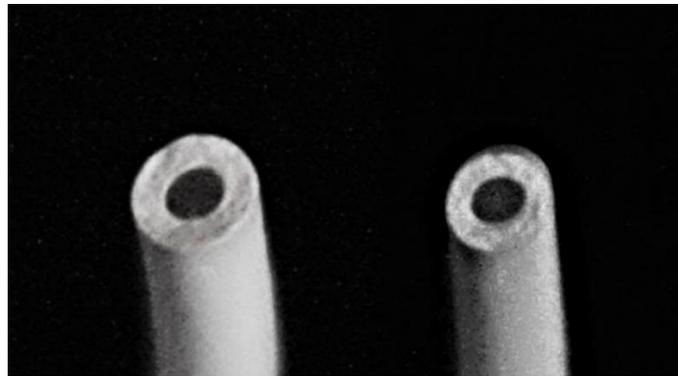
Fig. 5.16. Hollow-tubes produced using of infrared heating.

5.4.1.e. CNF content

The amount of CNF was reduced from 0.9% to 0.6% (w/w), while maintaining constant the solid loading (40%) and SA concentration (3% w/w) of the paste. The graph in Fig. 5.17. shows a sharp decrease in void ratio across all filament

diameters, which demonstrates the importance of CNF in the process of hollow-tube formation. Besides their role in reinforcing the shell, they are thought to facilitate the accumulation of material towards the dry exterior.
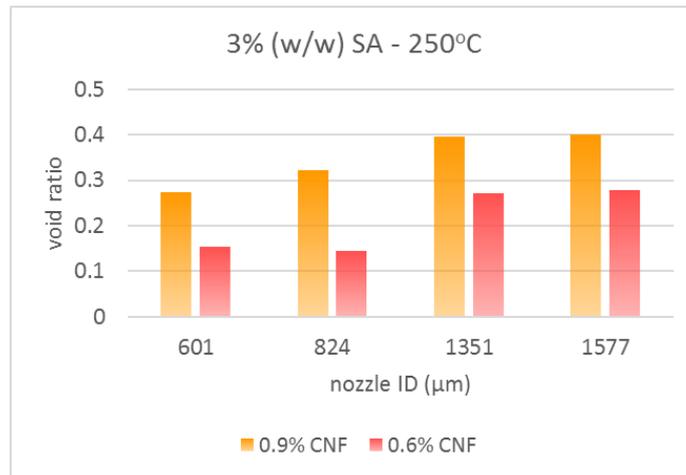
Fig. 5.17. Graph of void ratio *vs* nozzle diameter for pastes of varying CNF content.

5.4.1.f. Solid loading
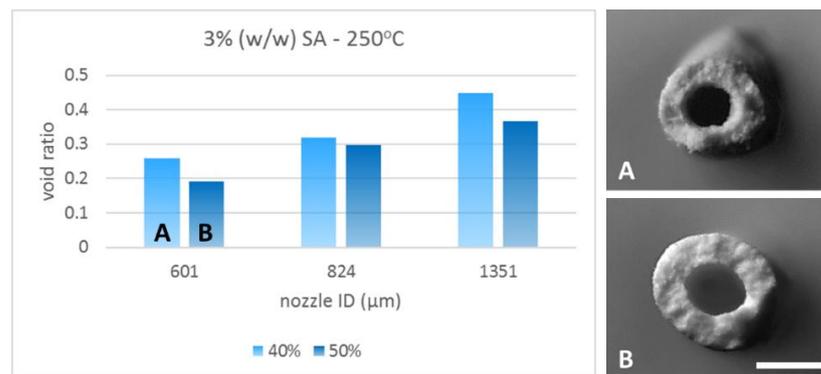
Fig. 5.18. Graph of void ratio against nozzle tip diameter for pastes with 40% and 50% w/w solid loading (left) and respective cross-sections (right), scale bar = 300 μm.

An increase in solid loading from 40 to 50% reduced the degree of shrinkage by 7% in average, but at the same time increased the relative shell thickness, as Fig. 5.18 suggests.

5.4.2. Oscillatory rheology tests
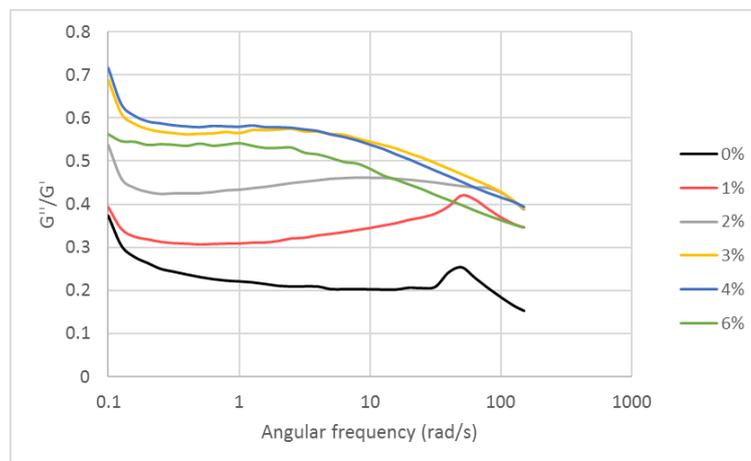
Fig. 5.19. Graph of loss tangent plotted against angular frequency for pastes of varying SA content.

The results suggest that the loss tangent, which is the ratio of the paste's loss modulus to its storage modulus, peaks at 3 and 4% (w/w) alginate content over a wide range of frequencies (see Fig. 5.19). During hollow-tube formation, the fluid's displacement is in the sub-millimetre scale depending on filament diameter (radial movement from wet core to dry shell). Additionally, even at 250°C, the process can take several minutes to complete. It is therefore assumed that the shear rates the material experiences, correspond to angular frequencies well below 1 rad/s. The present study has not been able to quantify these values. It was observed, however, that at 0.1 rad/s, the formulation containing 3% (w/w) alginate demonstrated the lowest values of complex viscosity (see Fig 5.20). This implies

that it behaves more like a fluid in comparison to all the other compositions but was still able to form a rigid crust on the surface of a filament once heated. At high shear rates, complex viscosity had an almost quadratic relationship with alginate concentration, with a shoulder appearing at 2%.
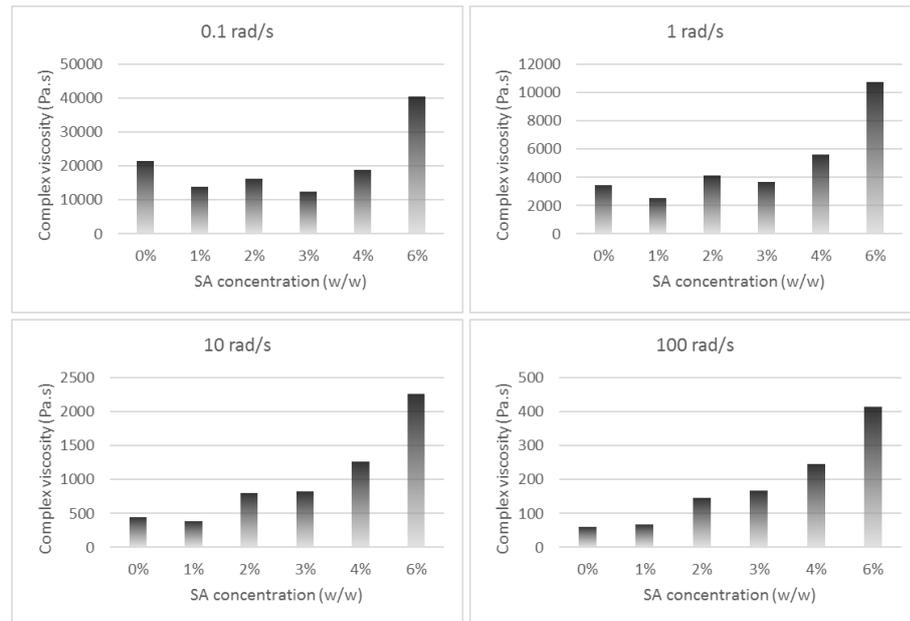
Fig. 5.20. Graphs of complex viscosity for pastes of varying alginate concentration oscillated at angular frequencies of 0.1, 1, 10 and 100 rad/s.

5.4.3. Qualitative assessment of the planar hollow-tube lattice

Several cross-sections of the generated hollow-tube lattice are illustrated in Fig. 5.21. The overall reliability of the process was diminished in comparison to single filaments. For example, shell thickness was greater near the centre of the lattice, with some members appearing to be solid. This was due to variations in the heating rate, which resulted in certain areas shrinking significantly before forming a rigid shell. Possible reasons include the uneven spatial distribution of heat emitted by the IR lamps and the increased thickness observed in junctions. Also, warping

174

suggests that evaporative cooling and the square geometry of the part caused the edges to dry more rapidly than its centre.
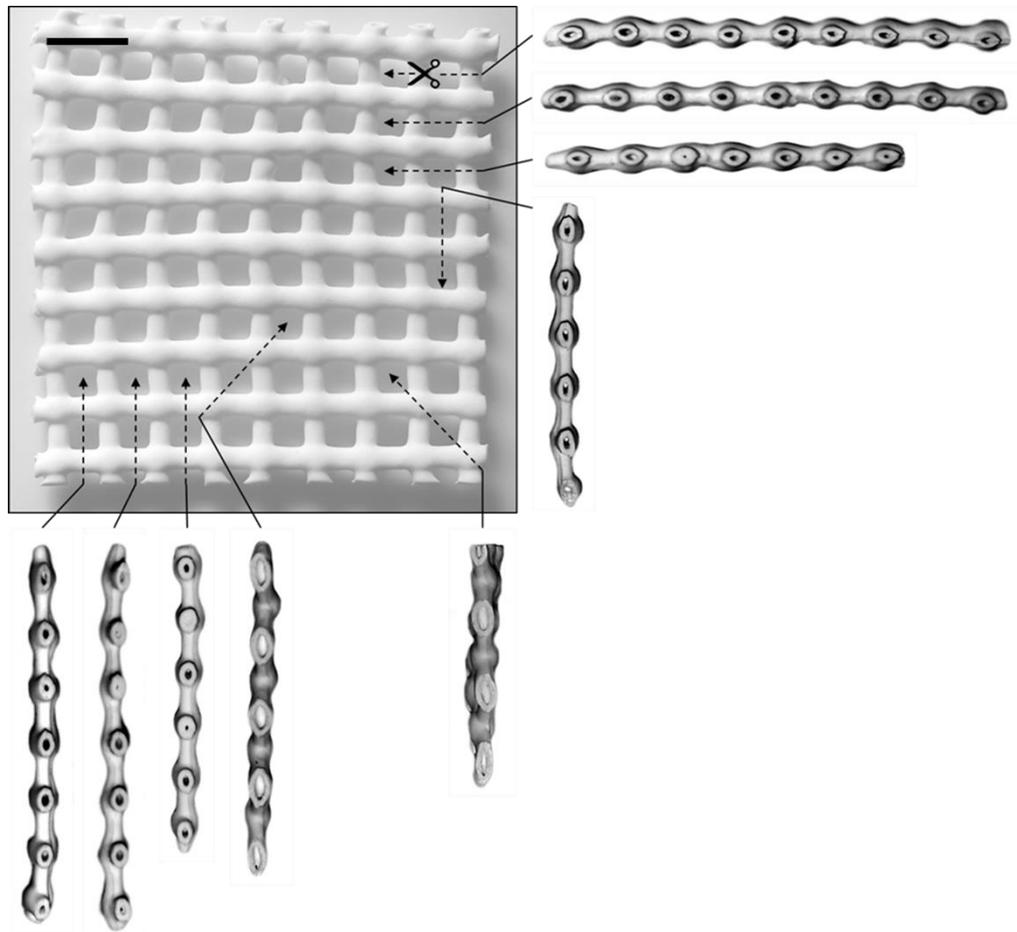
Fig. 5.21. Top view of planar hollow-tube lattice and images of cross-sections cut along indicated dashed lines, scale bar: 5mm.

It was possible to flatten the dry lattice and subsequently shape into various configurations by re-immersing in the calcium lactate solution (see Fig. 5.22). The majority of crossings were hollow, creating a continuous network of interconnected channels within the lattice structure. It is also worth mentioning that the cross-linking step imparted approximately 6% shrinkage, while drying further reduced the size of the specimen by another 15%. This resulted in average

member thickness decreasing from 1.55 mm to 1.35 mm. The use of IR lamps addressed the problem of thermal disintegration of the polymeric matrix, as it allowed for a precise control of the heating process.
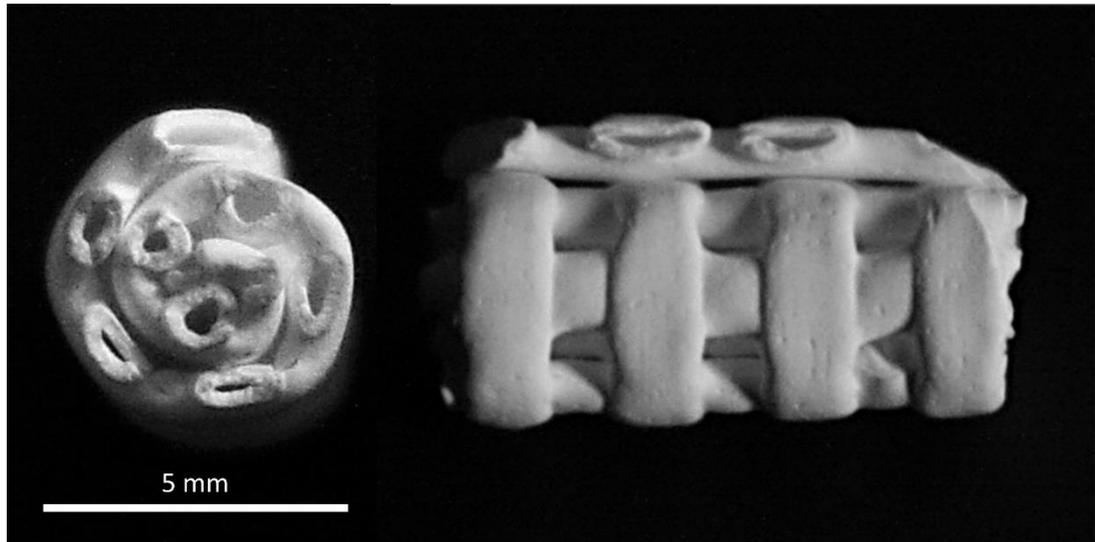
Fig. 5.22. Dry specimen in cylindrical configuration after immersion in calcium lactate solution.

These initial findings suggest that it is possible to fabricate structures with up to four levels of hierarchy with this particular technique. Starting from the smallest feature, the following levels can be identified: the shell's pore network (1) in each tubular member (2). The latter constitutes the structural unit of a flexible planar lattice (3), which can be manipulated to deliver a three-dimensional shape (4). Attempts to create hollow-tube lattices with thinner struts have been unsuccessful. Nonetheless, diminishing the diameter of the channels beyond a certain threshold could impair both cell migration and nutrient flow.

5.4.4. Fabrication of flexible 2D lattices.
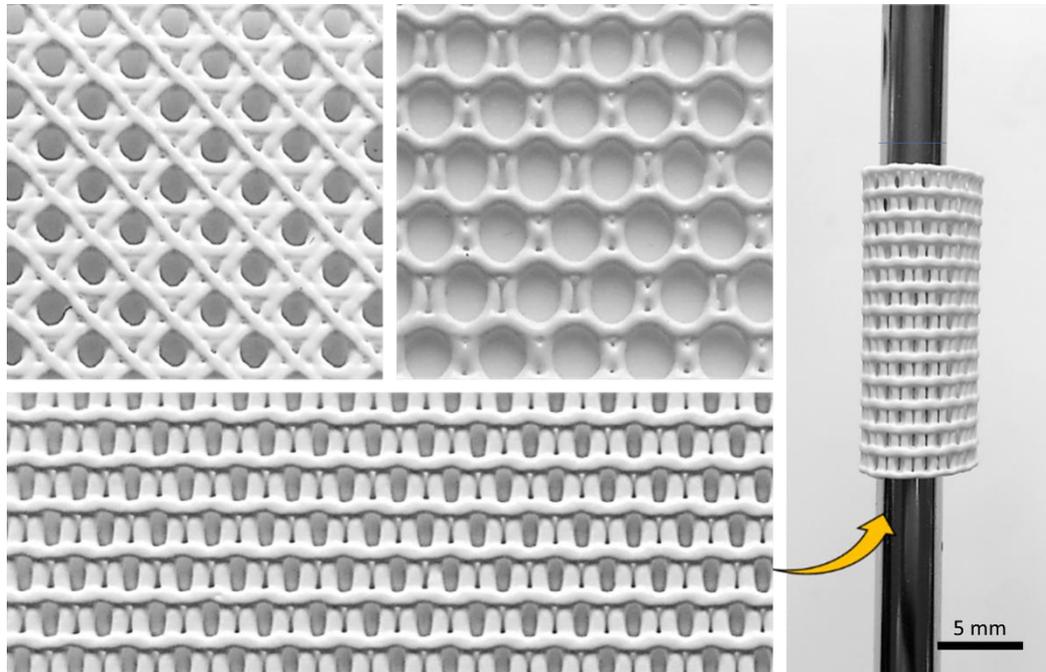
Fig. 5.23. Generated planar patterns (left) and rolling procedure (right) (filament diam. = 500 μm).

Figure 5.23 illustrates some of the patterns that were robocast using CNF/SA/β-TCP pastes with 40 and 50% w/w solid loading. The degree of shrinkage after the cross-linking step was estimated at 5.5% and 2.75% respectively. To minimise warping, they were wrapped in paper and left to dry slowly overnight (see Fig. 5.24). The dimensional change caused by sintering was influenced by the solid content of each group. The specimens with 40% solids exhibited smaller shrinkage (9.5% *vs* 16%) and shape distortion at the expense, however, of densification. This observation was confirmed by their poor mechanical strength, as they shattered with minimal handling (see Fig. 5.25). More work is required towards establishing the optimal sintering program and solid loading of the ink. Nevertheless, these experiments

demonstrated a simple and cost-effective method for manufacturing synthetic bone substitutes with fine features and increased geometric complexity.

40% solids   50% solids
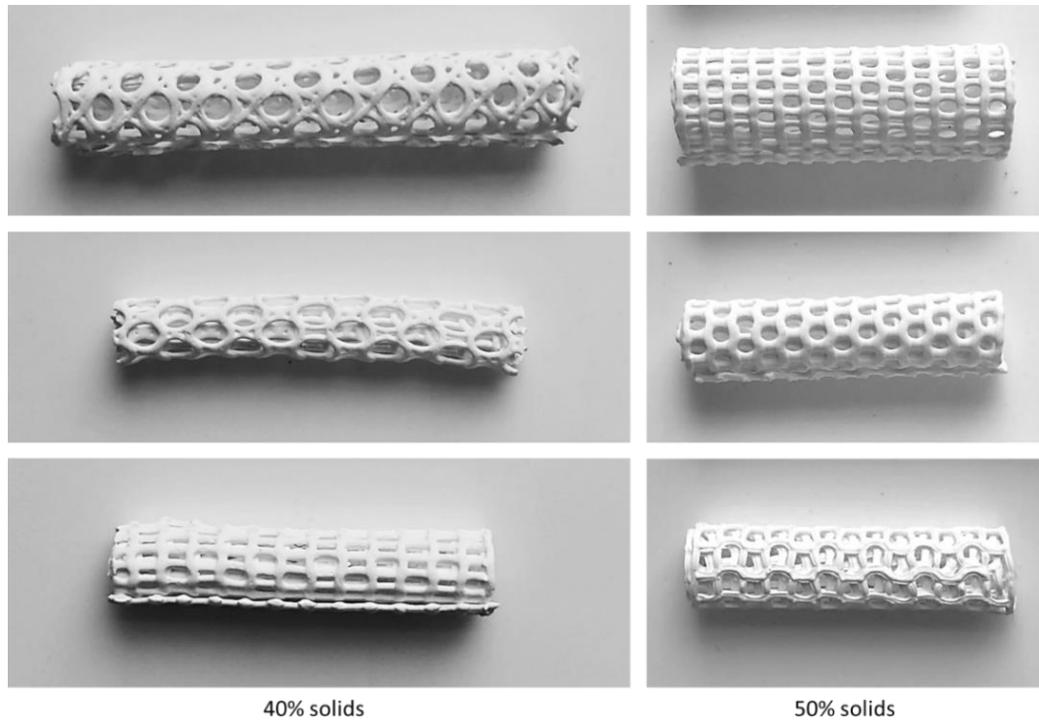
Fig. 5.24. Dry cross-linked specimens.
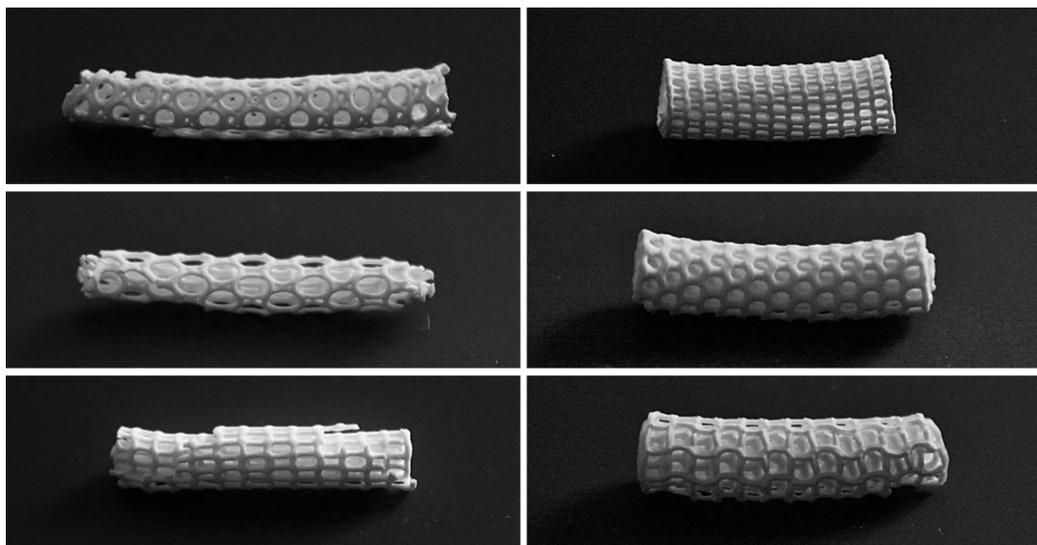
Fig. 5.25. Specimens after the sintering stage.

Chapter 6
Conclusions and recommendations for future work

6.1. Summary

In summary, chapter 1 set out the rationale for incorporating self-assembly into additive manufacturing techniques in the field of tissue engineering. An overview of materials currently used for bone tissue substitution was conducted, highlighting polymer/ceramic composites as ideal candidates, owing to their enhanced mechanical and biological properties. This exercise also emphasised the multiple and often conflicting requirements that have so far impeded their application in large load-bearing defects. The impact of porosity, which is a crucial biological requirement, on the mechanical performance of these synthetic materials remains a major challenge. The research identified a need for a deeper understanding of how biological materials are structured in nature, as a source of inspiration for design strategies capable of addressing some of these issues. A particular focus was placed upon methods for structuring bioceramic materials at different orders of magnitude - termed structural hierarchy. In bones, this constitutes the main mechanism contributing to their remarkable strength and fracture resistance. Additive manufacturing was proposed as the most appropriate technique for

patient and site-specific hierarchical scaffolds, as it offers precise control over their composition, microstructure and overall geometry. Generating, however, micron and submicron scale features would entail long lead times and high costs. This introduced the concept of combining AM with physical processes that cause the material to self-assemble into various configurations during or following its deposition.

Chapter 2 presented an argument for selecting filament-based techniques in this combinational approach to AM. To this end, the main types of AM processes for ceramic biomaterials were compared in terms of: versatility, ability to build multi-material structures, operating conditions, speed and cost. A number of examples were provided, in which a filament-based process was successfully combined with a conventional scaffold fabrication technique. The future role of parametric design software was also highlighted as a form-finding system that integrates design computation with tool-path generation for extrusion-based AM. Subsequently, a number of studies in the subject of ice-templating were presented, so as to demonstrate the potential of directional freezing in assembling ceramic suspensions into highly ordered microstructures. Their outstanding mechanical performance is due to toughening mechanisms often encountered in biological materials. These studies also made evident the ability to control particle assembly through altering a set of material and processing parameters. Although the process of robocasting in sub-zero ambient temperatures has been reported in literature, there is currently little evidence about the microstructural features that emerge when ceramic suspensions are frozen in an additive manner. Questions also arise

regarding the extent of each parameter's contribution to the microstructural outcome of this hybrid manufacturing technique.

Chapters 3, 4 and 5 constitute the experimental section of this thesis. Their contribution is identifiable in the following three key areas:

- Dispensing systems for Low-Temperature Deposition Modelling

- Printable bioceramic paste formulations

- Manufacturing processes for hierarchical hard tissue substitutes.

These are analysed separately in the sections that follow, together with recommendations for future work.

6.2. Dispensing system for LDM

It was established that auger valves offer the highest precision in micro-dispensing thixotropic ceramic pastes over a wide viscosity range. Other types of positive displacement pumps could also be employed, such as progressive cavity pumps. Based on these observations, a highly versatile and economical print-head was developed that can be operated at ambient temperatures down to -20°C. This was achieved by encasing the print-head in heated, thermally insulated compartments (i.e. heating sleeve and chamber), preventing the material from freezing and thus maintaining a consistent flow rate. In the future, this first functional prototype could benefit from monitoring the actual temperature of the fluid inside the pressurised reservoir and the feed passage as opposed to the heating elements themselves. This would enable the use of fluids whose viscosity is highly dependent on temperature. A more accurate control of the process would also require

compensation for possible discrepancies between the set temperature of the nozzle and that of the fluid as it is being extruded at varying flow rates and chamber temperatures. Moreover, the installation of an additional extruder would allow for building support structures or even altering, through the use of an inline mixer, the water content of the paste during the printing process. The latter would offer the ability to specify the pore morphology (lamellar or cellular) in different areas of the same part.

6.3. Printable bioceramic paste formulations

6.3.a. SA/XG/β-TCP

A novel β-TCP paste formulation of high water content (more than 80% v/v) was developed that takes advantage of the synergy that exists between Sodium Alginate and Xanthan Gum. The effect of these two gelling agents on paste rheology was initially investigated in isolation. It was observed that the addition of XG imparts a more shear thinning behaviour than SA for a given solid-to-water ratio. Increasing-decreasing stress ramp tests suggested a time-independent behaviour for SA-based slurries that is sensitive to variations in solid loading. On the other hand, XG-based slurries exhibited high thixotropy, with a slow recovery of viscosity however after agitation. The formulation containing both types of polymers behaved in a radically different way when subjected to shear. Dynamic tests revealed a time-dependent shear thinning behaviour with a rapid recovery of viscosity after shear, a feature that makes it ideal for robocasting. This bi-phasic polymer blend can also be used with other types of bio-ceramic materials. A certain

disadvantage is its high solubility in water, which means that a sintering stage is necessary in order to densify the ceramic matrix. Future research could potentially explore ways of addressing this particular issue.

6.3.b. SA/CNF/β-TCP

The addition of cellulose nano-fibrils in a SA-based β-TCP slurry resulted in a shear thinning formulation with good shape retention after deposition. Of particular interest were its following unique characteristics, which formed the basis of a novel method for fabricating hierarchical composite scaffolds:

- When heated rapidly, the paste forms hollow-shell structures.
- It can be cross-linked in a Ca^{2+}-rich solution, producing flexible yet strong particle-reinforced gels with minimal shrinkage.

6.4. Manufacturing processes for hard tissue substitutes

6.4.a. Low-Temperature Deposition Modelling

This research exemplified the use of Grasshopper® in the construction of parametric toolpaths. In the future, this approach will allow for introducing functional gradients through varying parameters such as composition, speed and nozzle temperature during the course of a deposition modelling process.

Moreover, it was determined that the overall quality of an object at a given ambient temperature, is reliant upon the speed and nozzle temperature at which it is printed. The higher the ambient temperature, the narrower the range of speeds

that can be attained. For an extrusion diameter of 0.5 mm, printing at 400 mm/min while maintaining nozzle temperature at its lowest possible value delivered the best outcome across the whole range of chamber temperatures. Also, prolonging the pause between dispensing cycles at higher chamber temperatures ensured that each layer had solidified before the addition of a new layer.

The findings suggest that LDM is capable of tailoring the microstructure of bio-ceramic scaffolds. It offers, more specifically, the ability to control not only the size and shape of the ice-crystals that grow as the suspension freezes, but also the direction of growth. The weighted average area of the pores produced by this process at a printing speed of 400 mm/min, as determined by confocal microscopy, was 170 μm^2 for specimens printed at -20°C and 400 μm^2 for those printed at -5°. These results correlated with data obtained from MIP tests, revealing considerable differences in their pore distribution. The former group predominantly contained pore openings that were 5 μm in diameter, as opposed to 13 μm in the latter. Micro-CT scans further confirmed these observations, evidencing the formation of cellular pores in the 30-100 μm range at -20°C and lamellar pores between 50-300 μm long at -5°C. These lamellar morphologies with a high degree of local alignment were the result of a slow solidification rate, which was experimentally estimated to be nearly four times slower than that corresponding to -20°C. The weighted average pore size for samples fabricated at -15 and -10°C was 355 and 310 μm^2 respectively. Their pore distribution, as determined by MIP tests, was nearly identical. Also, both samples displayed a higher percentage of pores in the 6-12 μm range compared to those obtained at -20°C. The paradoxical reduction in average

pore size that was observed at -10°C was attributed to a longer time interval between dispensing cycles.

Printing at low speeds (below 200 mm/min) and/or high set nozzle temperatures (SNT) caused the formation of localised clusters of comparatively large pores, which greatly impacted micro-structural uniformity. MIP tests also showed that increasing the SNT from 10 to 20°C for specimens fabricated at -15°C, widened the pore distribution and shifted it towards larger diameter values in the 7.5-15 μm range. Similarly, raising the speed from 400 to 800 mm/min at -20°C nearly doubled the average pore area. This time, however, a smooth transition between pore sizes was observed in the form of extensive gradients.

Altering the solid loading of the paste had the most remarkable effect on its freezing kinetics. More specifically, a 5% w/w increase in water content greatly reduced its solidification rate at -10°C, yielding a wider pore distribution that peaked at approximately 12 μm. The shape of the MIP curve also suggested the presence of lamellar morphologies.

The μ-CT scans also revealed that the direction of ice-crystal growth in each layer was dictated not only by temperature gradients, but also by the underlying ice structure. Another remarkable phenomenon, which was more pronounced at -5°C, was the presence of virtually identical particle assemblies in symmetrical structures. This led to the conclusion that the formation of patterns during freezing can be guided by the dispensing toolpath's geometry. Furthermore, LDM was able

to replicate at the micro-scale arch-like arrangements similar to those found in trabecular bone. This particular feature could be key to improving the toughness of bioceramic scaffolds in the future.

There is a multitude of possible avenues that this research could explore in the future. In the short term, it could focus on the effect of other processing parameters, such as the extrusion's diameter or forced convection, on the microstructural outcome of LDM. There is also a number of material parameters that remain to be investigated, the most important being the size of particles and the presence of additives that depress the paste's freezing point. This knowledge could then be put into practice through fabricating parts with functional gradients or localised variations in micromorphology. Further experiments would necessitate a more accurate control of the process itself. This would entail using an environmental chamber as opposed of an industrial freezer, which fluctuates less around the set temperature and allows for regulating humidity levels and pressure. Most importantly though, an emphasis should be placed upon controlling the direction of ice-crystal growth in the first layer, so that it is perpendicular to the deposition plane. For this purpose, an ice-templated slurry or a patterned surface could be used as substrates. This could offer the opportunity to study the effect of various toolpath geometries on pore orientation, since the ice structure that grows with each successive layer would have a common starting point across the entire part. Fig. 6.1 illustrates an idealised representation of a 3D lattice's cross-section, based on current findings. In the long term, the research should seek to establish appropriate sintering programs for consolidating the ceramic particles without

distorting the ice-templated structure. A method, also, for infiltrating the ceramic matrix with a polymer while maintaining its macro-porosity needs to be developed. This should be followed by mechanical and biological testing to evaluate the scaffold's performance in vitro.
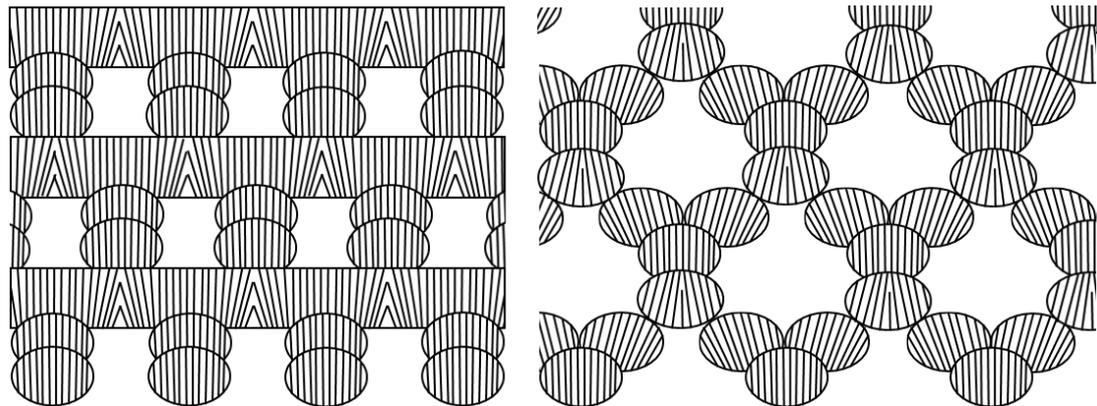
Fig. 6.1. Idealised representation of pore orientation in two different lattice geometries.

6.4.b. Robocasting of flexible hollow-tube lattices

The research also successfully demonstrated the combination of robocasting with a heating process to produce hollow-shell structures that can be manipulated into various configurations. Again, a number of material and processing parameters were investigated through experimenting with single beads. Optimal results were achieved at 3 and 4% w/w alginate content, where the paste's loss tangent reaches its maximum value. Lowering the concentration of cellulose nano-fibrils in the mixture had a detrimental effect on shell rigidity, causing it to partially collapse during heat treatment. Other factors that influenced the formation of hollow tubes was the heating temperature and the thickness of the extruded filament. For example, convection heating at 250°C, resulted in consistently higher void ratios than those obtained at 150°C, especially amongst filaments of large diameter. This

is due to the fact that high evaporation rates shorten the amount of time required for a rigid shell to form. In submillimetre filaments, however, the air-water interface ceases sooner, yielding smaller void ratios. The experiments also showed that it is possible to control the thickness of the shell by altering the paste's solid loading. Three major improvements were made to the manufacturing process:

- The first involved replacing the glass slide used in the original experiments with a fine aluminium mesh, which produced circular as opposed to bell-shaped cross-sections.

- The second was to employ infrared lamps instead of a convection oven to achieve a precise control over the rate and duration of heating, thus preventing the thermal degradation of the polymer matrix.

- Finally, a cross-linking step was introduced before heat treatment, which increased the shell's stiffness and facilitated the formation of hollow tubes.

The non-uniform heat distribution in planar lattices caused shape distortions and variations in shell thickness. In the future, this could be addressed by mounting the infrared lamps on a motor driven system that scans the lattice at defined speeds. A temperature feedback loop could also be incorporated, in order to experiment with different heat treatment profiles. In this initial study, the majority of crossings appeared to be hollow, suggesting a continuous network of interconnected channels within the lattice. However, a non-destructive 3D imaging technique, such as μ-CT, is required in order to quantify their degree of connectivity and exact size of the openings. Although this hybrid technique is limited to planar patterns, these can be folded or rolled into required three-dimensional configurations. This was

demonstrated with a number of lattices comprising both solid and hollow-tube struts. Another area that could be investigated is the hydraulic connectivity in different network geometries, which could be achieved by visualising fluid penetration through their channels. This expertise could then be used to design and fabricate small microfluidic devices, such as heat exchangers, artificial arteries etc. The determination of sintering parameters for the particular paste formulation is perhaps not of primary importance, since it can be cross-linked in Ca^{2+}-rich solutions. It is necessary however to study its swelling behaviour and solubility in water or simulated body fluid (SBF). Finally, its mechanical and biological performance needs to be evaluated in vitro to establish its suitability as a bone substitute material.

The processes explored in this research project successfully demonstrate the feasibility of incorporating self-assembly into Robocasting. This opens up new opportunities in controlling the micro-porosity and bio-resorption of synthetic bone substitutes. Additionally, the digital nature of these fabrication techniques offers a high degree of customisation for different bone defects. Most importantly, this study provides a method for replicating features often observed in biological materials. Mimicking design principles that exist in Nature, such as structural hierarchy and self-assembly, could be a promising route for stronger hard tissue substitutes.

Other sectors that could benefit from these findings include, but are not limited to, composite materials for the automotive/aerospace industry, filtration systems and catalyst supports used in chemical processes.

×2

A2

A2   A3   A4

Ø26   Ø15   Ø12.40

B1   Ø22   5.20   Ø3   42.20   42.20

B2   Ø15

B3   Ø5.20

B4

B5   Ø3.04
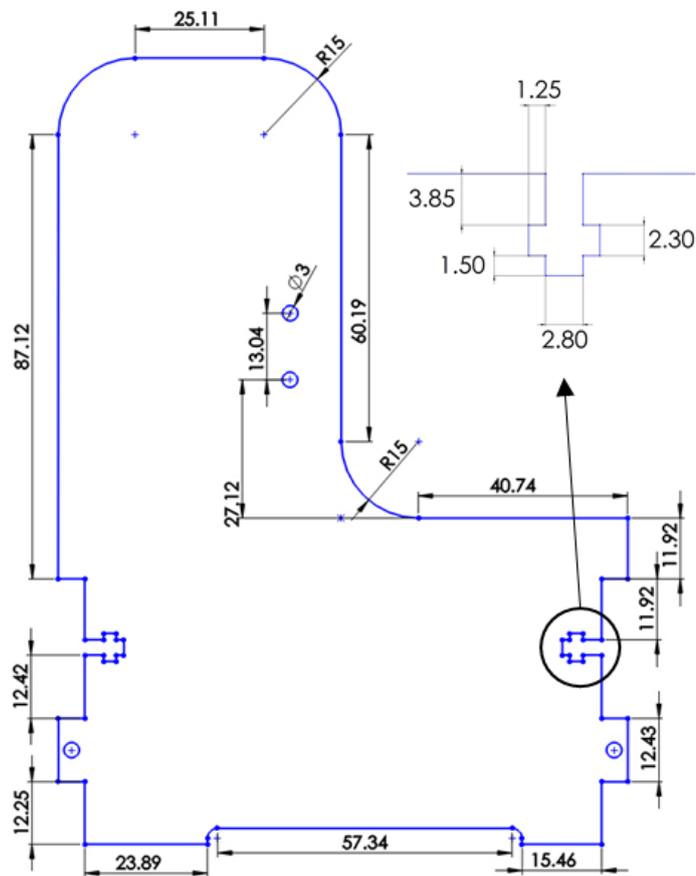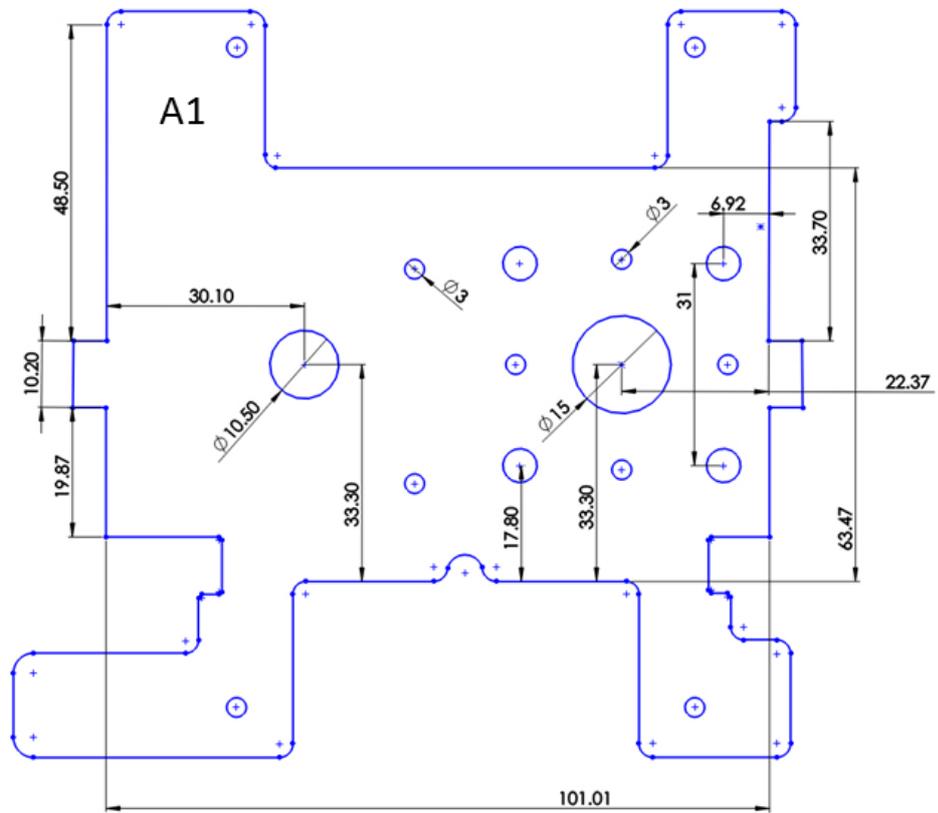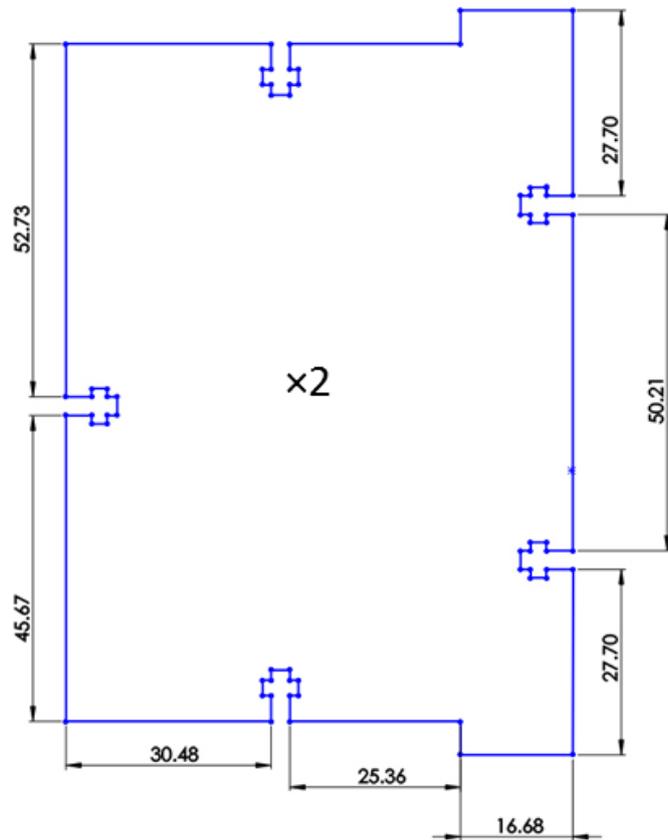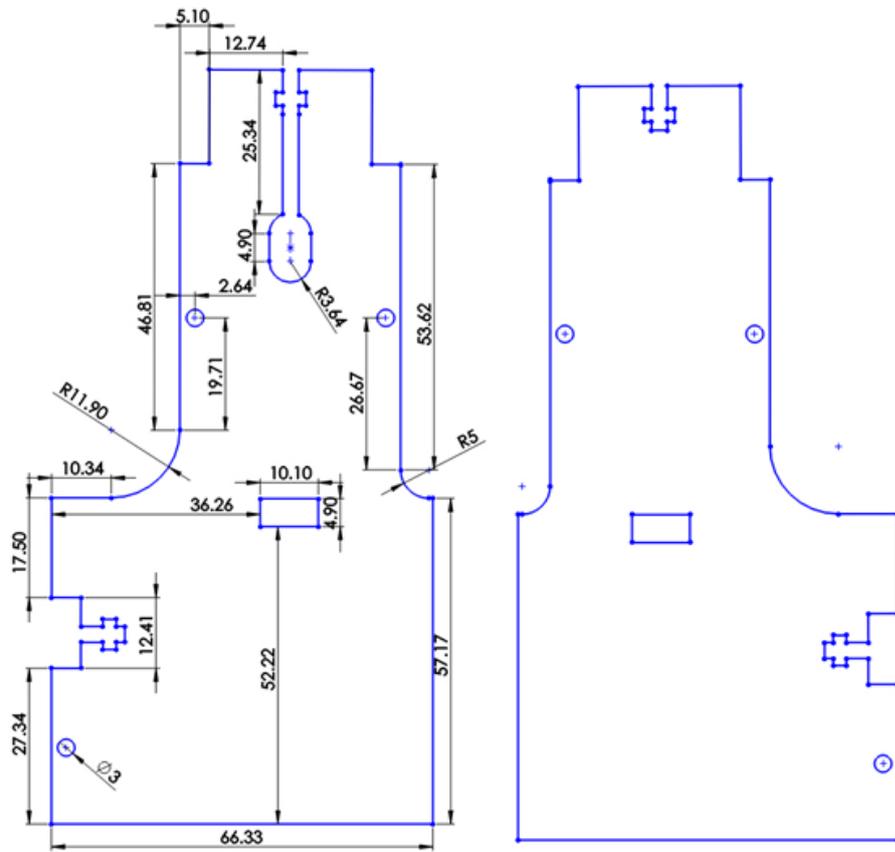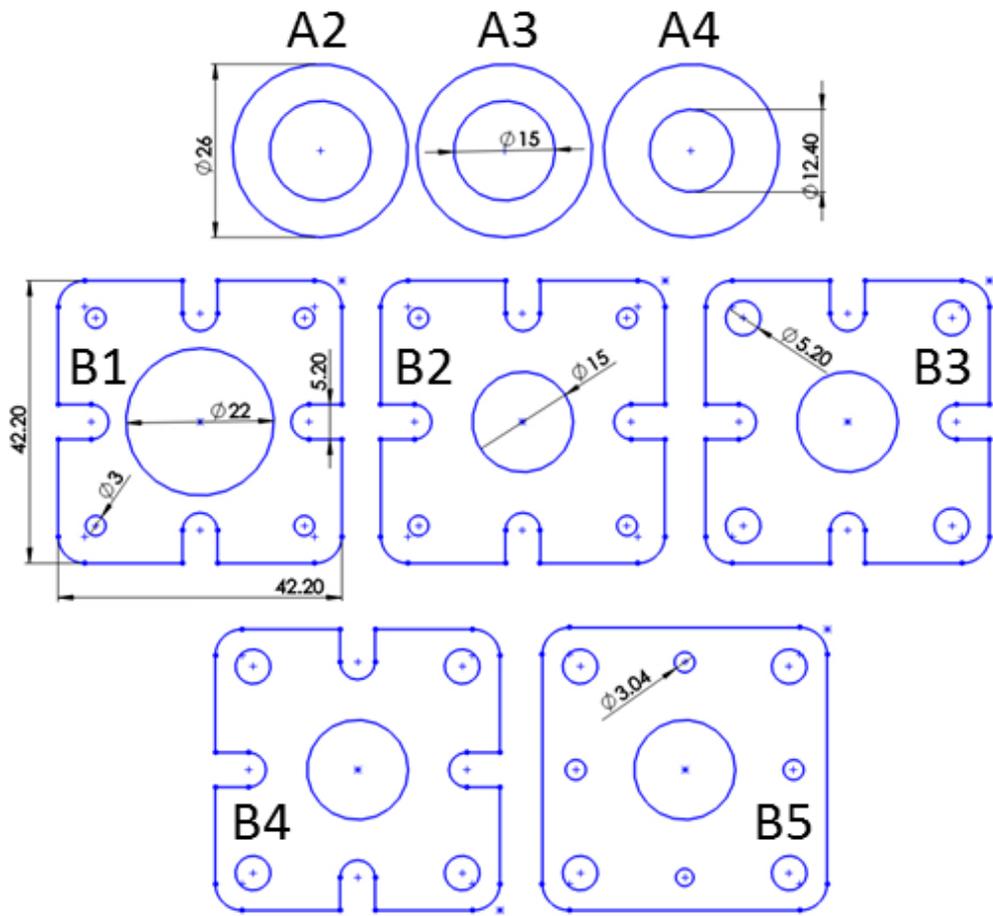
BIBLIOGRAPHY

Abdelaal, O.A.M., Darwish, S.M.H. (2013). Review of Rapid Prototyping Techniques for Tissue Engineering Scaffolds Fabrication, *Advanced Structured Materials*. pp. 33–54. doi:10.1007/978-3-642-31470-4_3

Aguilera, J.M., Lillford, P.J. (2008). The Crystalline State, *Food Materials Science : Principles and Practice*. Springer-Verlag, New York, pp. 45–65. doi:10.1007/978-0-387-71947

Ahn, B.Y., Duoss, E.B., Motala, M.J., Guo, X., Park, S.-I., Xiong, Y., Yoon, J., Nuzzo, R.G., Rogers, J.A., Lewis, J.A. (2009). Omnidirectional printing of flexible, stretchable, and spanning silver microelectrodes. *Science,* 323, pp. 1590–1593. doi:10.1126/science.1168375

Arafat, M.T., Gibson, I., Li, X. (2013). State of the art and future direction of additive manufactured scaffolds-based bone tissue engineering. *Rapid Prototyp. J.,* 20, pp. 13–26. doi:10.1108/RPJ-03-2012-0023

Arenson, L.U., Sego, D.C. (2006). The effect of salinity on the freezing of coarse-grained sands. *Can. Geotech. J.,* 43, pp. 325–337. doi:10.1139/T06-006

Avrami, M. (1940). Kinetics of Phase Change. II - Transformation-Time Relations for Random Distribution of Nuclei. *J. Chem. Phys.,* 8, pp. 212–224. doi:10.1063/1.1750631

Barnes, A. (1997). Thixotropy - A Review. *J. Non-Newtonian Fluid Mech,* 70, pp. 1–33.

Bartolo, P., Kruth, J.-P., Silva, J., Levy, G., Malshe, A., Rajurkar, K., Mitsuishi, M., Ciurana, J., Leu, M. (2012). Biomedical production of implants by additive electro-chemical and physical processes. *CIRP Ann. - Manuf. Technol.,* 61, pp. 635–655. doi:10.1016/j.cirp.2012.05.005

Bergstrom, L. (2001). Colloidal Processing of Ceramics, *The Handbook of Applied Surface and Colloid Chemistry - Part One*. Wiley, pp. 201–218.

Berk, Z. (2009). Freeze Drying (lyophilization) and Freeze Concentration, *Food Process Engineering and Technology*. Elsevier Inc., pp. 511–523. doi:10.1016/B978-0-12-415923-5.00023-X

Bertrand, P., Bayle, F., Combe, C., Goeuriot, P., Smurov, I. (2007). Ceramic components manufacturing by selective laser sintering. *Appl. Surf. Sci.,* 254, pp. 989–992. doi:10.1016/j.apsusc.2007.08.085

Bian, W., Li, D., Lian, Q., Li, X., Zhang, W., Wang, K., Jin, Z. (2012). Fabrication of a bio-inspired beta-Tricalcium phosphate/collagen scaffold based on ceramic stereolithography and gel casting for osteochondral tissue engineering. *Rapid Prototyp. J.,* 18, pp. 68–80. doi:10.1108/13552541211193511

Billiet, T., Vandenhaute, M., Schelfhout, J., Van Vlierberghe, S., Dubruel, P. (2012). A review of trends and limitations in hydrogel-rapid prototyping for tissue engineering. *Biomaterials,* 33, pp. 6020–6041. doi:10.1016/j.biomaterials.2012.04.050

Boccaccini, A.R., Chatzistavrou, X., Yunos, D.M., Califano, V. (2009). Biodegradable polymer-bioceramic composite scaffolds for bone tissue engineering. *Proc. 17th Int. Conf. Compos. Mater*.

Boher, M., Dobelin, N., Baroud, G. (2006). Theoretical and experimental approach to test the cohesion of calcium phosphatepastes. *Eur. Cell. Mater.,* 12, pp. 26–35.

Bohner, M. (2010a). Resorbable biomaterials as bone graft substitutes. *Mater. Today,* 13, pp. 24–30. doi:10.1016/S1369-7021(10)70014-6

Bohner, M. (2010b). Design of Ceramic-Based Cements and Putties for Bone Graft Substitution. *Eur. Cells Mater.,* 20, pp. 1–12.

Bohner, M., Baroud, G. (2005). Injectability of calcium phosphate pastes. *Biomaterials,* 26, pp. 1553–1563. doi:10.1016/j.biomaterials.2004.05.010

Bohner, M., Galea, L., Doebelin, N. (2012). Calcium phosphate bone graft substitutes: Failures and hopes. *J. Eur. Ceram. Soc.,* 32, pp. 2663–2671. doi:10.1016/j.jeurceramsoc.2012.02.028

Bohner, M., Loosli, Y., Baroud, G., Lacroix, D. (2011). Acta Biomaterialia Commentary : Deciphering the link between architecture and biological response of a bone graft substitute. *Acta Biomater.,* 7, pp. 478–484. doi:10.1016/j.actbio.2010.08.008

Bose, S., Roy, M., Bandyopadhyay, A. (2012). Recent advances in bone tissue engineering scaffolds. *Trends Biotechnol.,* 30, pp. 546–54. doi:10.1016/j.tibtech.2012.07.005

Bose, S., Vahabzadeh, S., Bandyopadhyay, A. (2013). Bone tissue engineering using 3D printing. *Biochem. Pharmacol.,* 16, pp. 496–504. doi:10.1016/j.mattod.2013.11.017

Bouxsein, M.L. (2013). Overview of Bone Structure and Strength. *Genet. bone Biol. Skelet. Dis.,* 25, pp. 25–34.

Brown, J.L., Kumbar, S.G., Laurencin, C.T. (2009). Bone Tissue Engineering, *Biomaterials Science: An Introduction to Materials in Medicine*. Elsevier, pp. 1194–1214. doi:10.1016/B978-0-08-087780-8.00113-3

Butscher, A., Bohner, M., Hofmann, S., Gauckler, L., Müller, R. (2011). Structural and material approaches to bone tissue engineering in powder-based three-dimensional printing. *Acta Biomater.,* 7, pp. 907–920. doi:10.1016/j.actbio.2010.09.039

Butscher, A., Bohner, M., Roth, C., Ernstberger, A., Heuberger, R., Doebelin, N., Rudolf, P., Rohr, V., Müller, R. (2012). Printability of calcium phosphate powders for three-dimensional printing of tissue engineering scaffolds. *Acta Biomater.,* 8, pp. 373–385. doi:10.1016/j.actbio.2011.08.027

Calori, G.M., Mazza, E., Colombo, M., Ripamonti, C. (2011). The use of bone-graft substitutes in large bone defects : Any specific needs ? *Injury,* 42, pp. S56–S63. doi:10.1016/j.injury.2011.06.011

Campbell, I., Bourell, D., Gibson, I. (2012). Additive manufacturing: rapid prototyping comes of age. *Rapid Prototyp. J.,* 18, pp. 255–258. doi:10.1108/13552541211231563

Carrodeguas, R.G., Aza, S. De. (2011). a -Tricalcium phosphate : Synthesis , properties and biomedical applications. *Acta Biomater.,* 7, pp. 3536–3546. doi:10.1016/j.actbio.2011.06.019

Castilho, M., Dias, M., Gbureck, U., Fernandes, P., Gouveia, B., Rodrigues, J. (2013). Fabrication of computationally designed scaffolds by low temperature 3D printing. *Biofrabrication,* 66(3), pp. 911-917 doi:10.1088/1758-5082/5/3/035012

Chan, B.P., Leong, K.W. (2008). Scaffolding in tissue engineering: general approaches and tissue-specific considerations. *Eur. spine J.,* 17, pp. 467–479. doi:10.1007/s00586-008-0745-3

Chen, Q., Zhu, C., Thouas, G. A. (2012). Progress and challenges in biomaterials used for bone tissue engineering: bioactive glasses and elastomeric composites. *Prog. Biomater.,* 1, pp. 1–22. doi:10.1186/2194-0517-1-2

Chevalier, J., Gremillard, L. (2009). Ceramics for medical applications : A picture for the next 20 years. *J. Eur. Ceram. Soc.,* 29, pp. 1245–1255. doi:10.1016/j.jeurceramsoc.2008.08.025

Chia, H.N., Wu, B.M. (2015). Recent advances in 3D printing of biomaterials. *J. Biol. Eng.,* 9(1), pp. 1-4. doi:10.1186/s13036-015-0001-4

Choi, J.-W., Kim, H.-C., Wicker, R. (2011). Multi-material stereolithography. *J. Mater. Process. Technol.,* 211, pp. 318–328. doi:10.1016/j.jmatprotec.2010.10.003

Chow, L. (2009). Next generation calcium phosphate-based biomaterials. *Dent. Mater.,* 28, pp. 1–10.

Clerck, N. De, Postnov, A. (2007). High resolution X-ray microtomography: Applications in biomedical research, *Textbook of in Vivo Imaging in Vertebrates.* John Wiley & Sons Ltd, pp. 57–77. doi:10.1002/9780470029596.ch2

Conrad, J.C., Ferreira, S.R., Yoshikawa, J., Shepherd, R.F., Ahn, B.Y., Lewis, J.A. (2011). Designing colloidal suspensions for directed materials assembly. *Curr. Opin. Colloid Interface Sci.,* 16, pp. 71–79. doi:10.1016/j.cocis.2010.11.002

Cook, K.L.K., Hartel, R.W. (2010). Mechanisms of ice crystallization in ice cream production. *Compr. Rev. Food Sci. Food Saf.,* 9, pp. 213–222. doi:10.1111/j.1541-4337.2009.00101.x

Correlo, V.M., Oliveira, J.M., Mano, J.F., Neves, N.M., Reis, R.L. (2011). Natural Origin Materials for Bone Tissue Engineering- Properties , Processing and Performance, *Principles of Regenerative Medicine*. Elsevier Inc., pp. 557–586. doi:10.1016/B978-0-12-381422-7.10032-X

Costa-Pinto, A.R., Reis, R.L., Neves, N.M. (2011). Scaffolds based bone tissue engineering: the role of chitosan. *Tissue Eng. Part B.* Rev., 17, pp. 331–47. doi:10.1089/ten.teb.2010.0704

Coussot, P. (2005). Experimental Procedures and Problems in Paste Viscometry, in: *Rheometry of Pastes, Suspensions, and Granular Materials: Applications in Industry and Environment.* Wiley, pp. 81–152.

Cox, S.C., Thornby, J.A., Gibbons, G.J., Williams, M.A., Mallick, K.K. (2015). 3D printing of porous hydroxyapatite scaffolds intended for use in bone tissue engineering applications. *Mater. Sci. Eng. C,* 47, pp. 237–247. doi:10.1016/j.msec.2014.11.024

Cui, F.-Z., Li, Y., Ge, J. (2007). Self-assembly of mineralized collagen composites. *Mater. Sci. Eng. R Reports,* 57, pp. 1–27. doi:10.1016/j.mser.2007.04.001

Davison, K.S., Siminoski, K., Adachi, J.D., Hanley, D. A, Goltzman, D., Hodsman, A. B., Josse, R., Kaiser, S., Olszynski, W.P., Papaioannou, A., Ste-Marie, L.G., Kendler, D.L., Tenenhouse, A., Brown, J.P. (2006). Bone strength: the whole is greater than the sum of its parts. *Semin. Arthritis Rheum.,* 36, pp. 22–31. doi:10.1016/j.semarthrit.2006.04.002

Deepa, B., Abraham, E., Pothan, L.A., Cordeiro, N., Faria, M., Thomas, S. (2016). Biodegradable nanocomposite films based on sodium alginate and cellulose nanofibrils. *Materials (Basel)*, 9, pp. 1–11. doi:10.3390/ma9010050

Deville, S. (2013). Ice templating , freeze casting : Beyond materials processing. *J. Mater. Res.*, pp. 1–18. doi:10.1557/jmr.2013.105

Deville, S. (2010). Freeze-Casting of Porous Biomaterials: Structure, Properties and Opportunities. *Materials (Basel)*, 3, pp. 1913–1927. doi:10.3390/ma3031913

Deville, S. (2008). Freeze-casting of porous ceramics: A review of current achievements and issues. *Adv. Eng. Mater.,* 10, pp. 155–169. doi:10.1002/adem.200700270

Deville, S., Meille, S., Seuba, J. (2015). A meta-analysis of the mechanical properties of ice-templated ceramics and metals. *Sci. Technol. Adv. Mater.,* 16, pp. 1-31. doi:10.1088/1468-6996/16/4/043501

Deville, S., Saiz, E., Nalla, R.K.., Tomsia, A.P. (2013). Freezing as a Path to Build Complex Composites. *Science,* 311, pp. 515–518.

Deville, S., Saiz, E., Tomsia, A.P. (2007). Ice-templated porous alumina structures. *Acta Biomater.,* 55, pp. 1965–1974. doi:10.1016/j.actamat.2006.11.003

Deville, S., Saiz, E., Tomsia, A.P. (2006). Freeze casting of hydroxyapatite scaffolds for bone tissue engineering. *Biomaterials,* 27, pp. 5480–5489. doi:10.1016/j.biomaterials.2006.06.028

Dorj, B., Park, J.H., Kim, H.W. (2012). Robocasting chitosan/nanobioactive glass dual-pore structured scaffolds for bone engineering. *Mater. Lett.,* 73, pp. 119–122. doi:10.1016/j.matlet.2011.12.107

Dorozhkin, S. V. (2013). Calcium Orthophosphate-Based Bioceramics. *Materials,* 9, 6, pp. 3840–3942. doi:10.3390/ma6093840

Dorozhkin, S. V (2010). Bioceramics of calcium orthophosphates. *Biomaterials,* 31, pp.1465–1485. doi:10.1016/j.biomaterials.2009.11.050

Dunlop, J.W.C., Weinkamer, R., Fratzl, P. (2011). Artful interfaces within biological materials. *Mater. Today,* 14, pp. 70–78. doi:10.1016/S1369-7021(11)70056-6

Eqtesadi, S., Motealleh, A., Miranda, P., Pajares, A., Lemos, A., Ferreira, J.M.F. (2014). Robocasting of 45S5 bioactive glass scaffolds for bone tissue engineering. *J. Eur. Ceram. Soc.,* 34, pp. 107–118. doi:10.1016/j.jeurceramsoc.2013.08.003

Fennema, O.R. (1996). Food Chemistry, *Food Chemistry*, Marcel Dekker, 1ˢᵗ Ed., New York.

Ferreira, A.M., Gentile, P., Chiono, V., Ciardelli, G. (2012). Collagen for bone tissue regeneration. *Acta Biomater.,* 8, pp. 3191–3200. doi:10.1016/j.actbio.2012.06.014

Fielding, G.A., Bandyopadhyay, A., Bose, S. (2011). Effects of silica and zinc oxide doping on mechanical and biological properties of 3D printed tricalcium phosphate tissue engineering scaffolds. *Dent. Mater.,* 28, pp. 113–122. doi:10.1016/j.dental.2011.09.010

Flemming, R.G., Murphy, C.J., Abrams, G.A., Goodman, S.L., Nealey, P.F. (1999). Effects of synthetic micro- and nano-structured surfaces on cell behavior. *Biomaterials,* 20, pp. 573–588.

Franco, J., Hunger, P., Launey, M.E., Tomsia, A.P., Saiz, E. (2010). Direct write assembly of calcium phosphate scaffolds using a water-based hydrogel. *Acta Biomater.,* 6, pp. 218–228. doi:10.1016/j.actbio.2009.06.031

Franks, F., Auffret, T. (2007). The Process Sequence in Summary, *Freeze-drying of Pharmaceuticals and Biopharmaceuticals : Principles and Practice*. Royal Society of Chemistry, Cambridge, pp. 13-53 doi:10.1039/9781847557704

Franks, F., Auffret, T. (2007). Secondary drying: The removal of unfrozen water, *Freeze-drying of Pharmaceuticals and Biopharmaceuticals : Principles and Practice*. Royal Society of Chemistry, Cambridge, pp. 121-129 doi:10.1039/9781847557704

Fratzl, P., Weinkamer, R. (2007). Nature's hierarchical materials. *Prog. Mater. Sci.,* 52, pp. 1263–1334. doi:10.1016/j.pmatsci.2007.06.001

Fu, Q., Saiz, E., Rahaman, M.N., Tomsia, A.P. (2013). Toward strong and tough glass and ceramic scaffolds for bone repair. *Adv. Funct. Mater.,* 23, pp. 5461–5476. doi:10.1002/adfm.201301121

Fu, Q., Saiz, E., Rahaman, M.N., Tomsia, A.P. (2011a). Bioactive glass scaffolds for bone tissue engineering: state of the art and future perspectives. *Mater. Sci. Eng. C. Mater. Biol. Appl.,* 31, pp. 1245–1256. doi:10.1016/j.msec.2011.04.022

Fu, Q., Saiz, E., Tomsia, A.P. (2011b). Direct ink writing of highly porous and strong glass scaffolds for load-bearing bone defects repair and regeneration. *Acta Biomater.,* 7, pp. 3547–3554. doi:10.1016/j.actbio.2011.06.030

Garcia-Ochoa, F., Santos, V.E., Casas, J.A., Gomez, E. (2000). Xanthan gum : production , recovery , and properties. *Biotechnol. Adv.,* 18, pp. 549–579.

Gerhardt, L.-C., Boccaccini, A.R. (2010). Bioactive Glass and Glass-Ceramic Scaffolds for Bone Tissue Engineering. *Materials (Basel).,* 3, pp. 3867–3910. doi:10.3390/ma3073867

Giannitelli, S.M., Mozetic, P., Trombetta, M., Rainer, A. (2015). Combined additive manufacturing approaches in tissue engineering. *Acta Biomater.,* 24, pp. 1–11. doi:10.1016/j.actbio.2015.06.032

Giesche, H. (2006). Mercury porosimetry: A general (practical) overview. *Particle and Particle Syst. Charact.,* 23, pp. 9–19. doi:10.1002/ppsc.200601009

Giesen, E.B.W., Ding, M., Dalstra, M., Eijden, T.M.G.J. Van. (2001). Mechanical properties of cancellous bone in the human mandibular condyle are anisotropic. *Journal of Biomechanics,* 34, pp. 799–803.

Ginebra, M.P., Espanol, M., Montufar, E.B., Perez, R. a, Mestres, G. (2010). New processing approaches in calcium phosphate cements and their applications in regenerative medicine. *Acta Biomater.,* 6, pp. 2863–73. doi:10.1016/j.actbio.2010.01.036

Gmeiner, R., Mitteramskogler, G., Stampfl, J., Boccaccini, A.R. (2015). Stereolithographic ceramic manufacturing of high strength bioactive glass. *Int. J. Appl. Ceram. Technol.,* 12, pp. 38–45. doi:10.1111/ijac.12325

Goycoolea, F.M., Richardson, R.K., Morris, E.R., Gidley, M.J. (1995). Stoichiometry and Conformation of Xanthan in Synergistic Gelation with Locust Bean Gum or Konjac Glucomannan: Evidence for Heterotypic Binding. *Macromolecules,* 28, pp. 8308–8320. doi:10.1021/ma00128a047

Green, D., Walsh, D., Mann, S., Oreffo, R.O.C. (2002). The potential of biomimesis in bone tissue engineering: lessons from the design and synthesis of invertebrate skeletons. *Bone,* 30, pp. 810–5.

Guo, N., Leu, M.C. (2013). Additive manufacturing: Technology, applications and research needs. *Front. Mech. Eng.,* 8, pp. 215–243. doi:10.1007/s11465-013-0248-8

Gutiérrez, M.C., Ferrer, M.L., Monte, F. (2008). Ice-Templated Materials : Sophisticated Structures Exhibiting Enhanced Functionalities Obtained after Unidirectional Freezing and Ice-Segregation-Induced Self-Assembly. *Chemistry of Materials,* 20, pp. 634–648.

Handscomb, C.S., Kraft, M., Bayly, A.E. (2009). A new model for the drying of droplets containing suspended solids after shell formation. *Chem. Eng. Sci.,* 64, pp. 228–246. doi:10.1016/j.ces.2008.10.019

Hannink, G., Arts, J.J.C. (2011). Bioresorbability, porosity and mechanical strength of bone substitutes: what is optimal for bone regeneration? *Injury,* 42, pp. S22–25. doi:10.1016/j.injury.2011.06.008

Henriksen, S.S., Ding, M., Juhl, M.V., Theilgaard, N., Overgaard, S. (2011). Mechanical strength of ceramic scaffolds reinforced with biopolymers is comparable to that of human bone. *J. Mater. Sci. Mater. Med.,* 22, pp. 1111–1118. doi:10.1007/s10856-011-4290-y

Holzwarth, J.M., Ma, P.X. (2011). Biomimetic nanofibrous scaffolds for bone tissue engineering. *Biomaterials,* 32, pp. 9622–9629. doi:10.1016/j.biomaterials.2011.09.009

Huang, T., Mason, M.S., Hilmas, G.E., Leu, M.C. (2006). Freeze-form extrusion fabrication of ceramic parts. *Virtual Phys. Prototyp.,* 1, pp. 93–100. doi:10.1080/17452750600649609

Huang, T., Mason, M.S., Zhao, X., Hilmas, G.E., Leu, M.C. (2009). Aqueous-based freeze-form extrusion fabrication of alumina components. *Rapid Prototyp. J.,* 15, pp. 88–95. doi:10.1108/13552540910943388

Huq, T., Salmieri, S., Khan, A., Khan, R. a, Le Tien, C., Riedl, B., Fraschini, C., Bouchard, J., Uribe-Calderon, J., Kamal, M.R., Lacroix, M. (2012). Nanocrystalline cellulose (NCC) reinforced alginate based biodegradable nanocomposite film. *Carbohydr. Polym.,* 90, pp. 1757–1763. doi:10.1016/j.carbpol.2012.07.065

Inzana, J.A., Olvera, D., Fuller, S.M., Kelly, J.P., Graeve, O.A., Schwarz, E.M., Kates, S.L., Awad, H.A. (2014). 3D printing of composite calcium phosphate and collagen scaffolds for bone regeneration. *Biomaterials,* 35, pp. 4026–4034. doi:10.1016/j.biomaterials.2014.01.064

Janicki, P., Schmidmaier, G. (2011). What should be the characteristics of the ideal bone graft substitute? Combining scaffolds with growth factors and/or stem cells. *Injury,* 42, pp. S77–S81. doi:10.1016/j.injury.2011.06.014

Kalia, S., Dufresne, A., Cherian, B.M., Kaith, B.S., Avérous, L., Njuguna, J., Nassiopoulos, E. (2011). Cellulose-Based Bio- and Nanocomposites: A Review. *Int. J. Polym. Sci.,* pp. 1–35. doi:10.1155/2011/837875

Kalyon, D.M., Yu, X., Wang, H., Valdevit, A., Ritter, A. (2013). Twin Screw Extrusion Based Technologies Offer Novelty , Versatility , Reproducibility and Industrial Scalability for Fabrication of Tissue Engineering Scaffolds. *J Tissue Sci Eng,* 4, pp. 2–3. doi:10.4172/2157-7552.1000e126

Karam, G.N., Gibson, L.J. (1995). Elastic buckling of cylindrical shells with elastic cores—I. Analysis. *Int. J. Solids Struct.,* 32, pp. 1259–1283. doi:10.1016/0020-7683(94)00147-O

Koch, J. C. (1917). The laws of bone architecture. *Am. J. Anat.,* 21, pp. 117-208.

Kolk, A., Handschel, J., Drescher, W., Rothamel, D., Kloss, F., Blessmann, M., Heiland, M., Wolff, K.-D., Smeets, R. (2012). Current trends and future perspectives of bone substitute materials - from space holders to innovative biomaterials. *J. Craniomaxillofac. Surg.,* 40, pp. 706–718. doi:10.1016/j.jcms.2012.01.002

Krokida, M.K., Karathanos, V.T., Maroulis, Z.B. (1998). Effect of Freeze-drying Conditions on Shrinkage and Porosity of Dehydrated Agricultural Products. *J. Food Eng.,* 35, pp. 369–380. doi:10.1016/S0260-8774(98)00031-4

Krüger, R., Groll, J. (2012). Fiber reinforced calcium phosphate cements -- on the way to degradable load bearing bone substitutes? *Biomaterials,* 33, pp. 5887–5900. doi:10.1016/j.biomaterials.2012.04.053

Kruth, J.P., Levy, G., Klocke, F., Childs, T.H.C. (2007). Consolidation phenomena in laser and powder-bed based layered manufacturing. *CIRP Ann. - Manuf. Technol.,* 56, pp. 730–759. doi:10.1016/j.cirp.2007.10.004

Lakes, R. (1993). Materials with structure hierarchy. *Nature,* 361, pp. 511–515. doi:10.1038/361511a0

Lan Levengood, S.K., Polak, S.J., Wheeler, M.B., Maki, A.J., Clark, S.G., Jamison, R.D., Wagoner, A.J. (2010). Multiscale osteointegration as a new paradigm for the design of calcium phosphate scaffolds for bone regeneration. *Biomaterials*, 31, pp. 3552–3563. doi:10.1016/j.biomaterials.2010.01.052

Launey, M.E., Buehler, M.J., Ritchie, R.O. (2010). On the Mechanistic Origins of Toughness in Bone. *Annu. Rev. Mater. Res.,* 40, pp. 25–53. doi:10.1146/annurev-matsci-070909-104427

Launey, M.E., Munch, E., Alsem, D.H., Saiz, E., Tomsia, A.P., Ritchie, R.O. (2009). A novel biomimetic approach to the design of high-performance ceramic – metal composites. *J. R. Soc. Interface,* 7, pp. 741-753 doi:10.1098/rsif.2009.0331

Lee, K.Y., Mooney, D.J. (2012). Alginate: Properties and biomedical applications. *Prog. Polym. Sci.,* 37, pp. 106–126. doi:10.1016/j.progpolymsci.2011.06.003

Leu, M.C., Deuser, B.K., Tang, L., Landers, R.G., Hilmas, G.E., Watts, J.L. (2012). Freeze-form extrusion fabrication of functionally graded materials. *CIRP Ann. - Manuf. Technol.,* 61, pp. 223–226. doi:10.1016/j.cirp.2012.03.050

Leu, M.C., Tang, L., Deuser, B., Landers, R.G., Hilmas, G.E., Zhang, S., Watts, J. (2011). Freeze-Form Extrusion Fabrication of Composite Structures, *Solid Freeform Fabrication Symposium,* pp. 111–124.

Leu, M.C., Zhang, W., Sui, G. (2000). An Experimental and Analytical Study of Ice Part Fabrication with Rapid Freeze Prototyping. *CIRP Ann. - Manuf. Technol.,* 49, pp. 147–150. doi:10.1016/S0007-8506(07)62916-3

Lewis, J. A. (2006). Direct Ink Writing of 3D Functional Materials. *Adv. Funct. Mater.,* 16, pp. 2193–2204. doi:10.1002/adfm.200600434

Lewis, J.A., Gratson, G.M. (2004). Direct writing in three dimensions. *Mater. Today,* 7, pp. 32–39. doi:10.1016/S1369-7021(04)00344-X

Li, J.P., de Wijn, J.R., Van Blitterswijk, C. A., de Groot, K. (2006). Porous Ti6Al4V scaffold directly fabricating by rapid prototyping: preparation and in vitro experiment. *Biomaterials,* 27, pp. 1223–35. doi:10.1016/j.biomaterials.2005.08.033

Li, W., Ghazanfari, A., Leu, M.C., Landers, R.G. (2015). Methods of Extrusion on Demand for High Solids Loading Ceramic Paste in Freeform Extrusion Fabrication. *Int. Solid Free. Fabr. Symp.,* pp. 332–345.

Lichte, P., Pape, H.C., Pufe, T., Kobbe, P., Fischer, H. (2011). Scaffolds for bone healing : Concepts , materials and evidence. *Injury,* 42, pp. 569–573. doi:10.1016/j.injury.2011.03.033

Lim, T.C., Bang, C.P., Chian, K.S., Leong, K.F. (2008). Development of cryogenic prototyping for tissue engineering. *Virtual Phys. Prototyp.,* 3, pp. 25–31. doi:10.1080/17452750701799303

Lin, N., Bruzzese, C., Dufresne, A. (2012). TEMPO-oxidized nanocellulose participating as crosslinking aid for alginate-based sponges. ACS Appl. Mater. Interfaces, 4, pp. 4948–59. doi:10.1021/am301325r

Liu, P.S., Chen, G.F. (2014). Fabricating Porous Ceramics, *Porous Materials*. Elsevier Inc., pp. 221–302. doi:10.1016/B978-0-12-407788-1.00005-8

Lu, L., Zhang, Q., Wootton, D., Lelkes, P.I., Zhou, J. (2010). A novel sucrose porogen-based solid freeform fabrication system for bone scaffold manufacturing. *Rapid Prototyp. J.,* 16, pp. 365–376. doi:10.1108/13552541011065768

Lu, X., Lee, Y., Yang, S., Hao, Y., Evans, J.R.G., Parini, C.G. (2010). Solvent-based paste extrusion solid freeforming. *J. Eur. Ceram. Soc.,* 30, pp. 1–10. doi:10.1016/j.jeurceramsoc.2009.07.019

Luo, Y., Lode, A., Gelinsky, M. (2013). Direct plotting of three-dimensional hollow fiber scaffolds based on concentrated alginate pastes for tissue engineering. *Adv. Healthc. Mater.,* 2, pp. 777–783. doi:10.1002/adhm.201200303

Luo, Y., Zhai, D., Huan, Z., Zhu, H., Xia, L., Chang, J., Wu, C. (2015). Three-Dimensional Printing of Hollow-Struts-Packed Bioceramic Scaffolds for Bone Regeneration. *ACS Appl. Mater. Interfaces,* 7, pp. 24377–24383. doi:10.1021/acsami.5b08911

Ma, P.X. (2008). Biomimetic materials for tissue engineering. *Adv. Drug Deliv. Rev.,* 60, pp. 184–198. doi:10.1016/j.addr.2007.08.041

Maazouz, Y., Montufar, E.B., Guillem-Marti, J., Fleps, I., Ohman, C., Persson, C., Ginebra, M.P. (2014). Robocasting of biomimetic hydroxyapatite scaffolds using self-setting inks. *J. Mater. Chem.* B, pp. 5378–5386. doi:10.1039/C4TB00438H

Malinauskas, M., Rekstyte, S., Lukosevicius, L., Butkus, S., Balciunas, E., Peciukaityte, M., Baltriukiene, D., Bukelskiene, V., Butkevicius, A., Kucevicius, P., Rutkunas, V., Juodkazis, S. (2014). 3D microporous scaffolds manufactured via combination of fused filament fabrication and direct laser writing ablation. *Micromachines,* 5, pp. 839–858. doi:10.3390/mi5040839

Martínez-vázquez, F.J., Perera, F.H., Miranda, P., Pajares, A., Guiberteau, F. (2010). Improving the compressive strength of bioceramic robocast scaffolds by polymer infiltration. *Acta Biomater.,* 6, pp. 4361–4368. doi:10.1016/j.actbio.2010.05.024

Mastrogiacomo, M., Scaglione, S., Martinetti, R., Dolcini, L., Beltrame, F., Cancedda, R., Quarto, R. (2006). Role of scaffold internal structure on in vivo bone formation in macroporous calcium phosphate bioceramics. *Biomaterials,* 27, pp. 3230–3237. doi:10.1016/j.biomaterials.2006.01.031

Melchels, F.P.W., Domingos, M. A. N., Klein, T.J., Malda, J., Bartolo, P.J., Hutmacher, D.W. (2012). Additive manufacturing of tissues and organs. *Prog. Polym. Sci.,* 37, pp. 1079–1104. doi:10.1016/j.progpolymsci.2011.11.007

Melchels, F.P.W., Feijen, J., Grijpma, D.W. (2010). A review on stereolithography and its applications in biomedical engineering. *Biomaterials,,* 31, pp. 6121–6130. doi:10.1016/j.biomaterials.2010.04.050

Mewis, J., Wagner, N.J. (2011). Rheometry of suspensions, *Colloidal Suspension Rheology*, Cambridge Univ Press, pp. 291–324. doi:http://dx.doi.org/10.1017/CBO9780511977978

Mewis, J., Wagner, N.J. (2011). Thixotropy, *Colloidal Suspension Rheology*, Cambridge University Press, Cambridge, pp. 530–531. doi:10.1017/CBO9780511977978

Miao, X., Sun, D. (2009). Graded/Gradient Porous Biomaterials. *Materials (Basel),* 3, pp. 26–47. doi:10.3390/ma3010026

Miller, S.E., Mink, H., Goering, H.L., Himes, R.C. (1959). Zone Freezing in Demineralizing Saline Waters. *Ind. Eng. Chem.,* 51, pp. 1345–1348.

Miller, Z., Fuchs, M.B. (2005). Effect of trabecular curvature on the stiffness of trabecular bone. *J. Biomechanics,* 38, pp. 1855–1864. doi:10.1016/j.jbiomech.2004.08.018

Mohamad Y.D., Bretcanu, O., Boccaccini, A.R. (2008). Polymer-bioceramic composites for tissue engineering scaffolds. *J. Mater. Sci.,* 43, pp. 4433–4442. doi:10.1007/s10853-008-2552-y

Mookerjee, A., Cohen, D.L., Peng, D.H., Bonassar, L.J., Lipson, H. (2009). A Study of Variable Stiffness Alginate Printing for Medical Applications, *Solid Freeform Fabrication Symposium*. pp. 584–594.

Moon, Y.W., Choi, I.J., Koh, Y.H., Kim, H.E. (2015). Macroporous alumina scaffolds consisting of highly microporous hollow filaments using three-dimensional ceramic/camphene-based co-extrusion. *J. Eur. Ceram. Soc.,* 35, pp. 4623–4627. doi:10.1016/j.jeurceramsoc.2015.08.017

Moroni, L., Schotel, R., Sohier, J., de Wijn, J.R., van Blitterswijk, C.A. (2006). Polymer hollow fiber three-dimensional matrices with controllable cavity and shell thickness, *Biomaterials,* 27, pp. 5918–5926. doi:10.1016/j.biomaterials.2006.08.015

Mostafavi, S., Bier, H. (2016). Materially Informed Design to Robotic Production: A Robotic 3D Printing System for Informed Material Deposition, *Robotic Fabrication in Architecture, Art and Design*, Springer International Publishing, pp. 338–349. doi:10.1007/978-3-319-26378-6_27

Mota, C., Puppi, D., Chiellini, F., Chiellini, E. (2012). Additive manufacturing techniques for the production of tissue engineering constructs. *J. Tissue Eng. Regen. Med.,* 9, pp. 174–190. doi:10.1002/term.1635

Munch, E., Launey, M.E., Alsem, D.H., Saiz, E., Tomsia, A.P., Ritchie, R.O. (2008). Tough, bio-inspired hybrid materials. *Science,* 322, pp. 1516–1520. doi:10.1126/science.1164865

Munch, E., Saiz, E., Tomsia, A.P., Deville, S. (2009). Architectural Control of Freeze-Cast Ceramics Through Additives and Templating. *J. Am. Ceram. Soc.,* 92, pp. 1534–1539. doi:10.1111/j.1551-2916.2009.03087.x

Murphy, D.B., Davidson, M.W. (2012). Confocal Laser Scanning Microscopy, *Fundamentals of Light Microscopy and Electronic Imaging*, John Wiley & Sons Inc., pp. 265–305. doi:10.1002/9781118382905

Nandakumar, A., Barradas, A., de Boer, J., Moroni, L., van Blitterswijk, C., Habibovic, P. (2013). Combining technologies to create bioactive hybrid scaffolds for bone tissue engineering. *Biomatter,* 3, pp. 1–13.

Nandi, S.K., Roy, S., Mukherjee, P., Kundu, B., Basu, D. (2010). Orthopaedic applications of bone graft & graft substitutes : a review. *Indian J. Med. Res.,* 132, pp. 15–30.

Narayan, R. (2010). Two Photon Polymerisation: An Emerging Method for Rapid Prototyping of Ceramic-Polymer Hybrid Materials for Medical Applications. *Am. Ceram. Soc. Bull.*, 88, pp. 20–25.

Olmsted, P.D. (2008). Perspectives on shear banding in complex fluids. *Rheol. Acta,* 47, pp. 283–300. doi:10.1007/s00397-008-0260-9

Oxman, N. (2010). Structuring Materiality: Design Fabrication of Heterogeneous Materials. *Archit. Des.,* 80, pp. 78–85. doi:10.1002/ad.1110

Peña, J., Román, J., Cabañas, M.V., Vallet-regí, M. (2010). An alternative technique to shape scaffolds with hierarchical porosity at physiological temperature. *Acta Biomater.,* 6, pp. 1288–1296. doi:10.1016/j.actbio.2009.10.049

Perera, F.H., Martínez-Vázquez, F.J., Miranda, P., Ortiz, A.L., Pajares, A. (2010). Clarifying the effect of sintering conditions on the microstructure and mechanical properties of β-tricalcium phosphate. *Ceram. Int.,* 36, pp. 1929–1935. doi:10.1016/j.ceramint.2010.03.015

Perez, R.A., Kim, H., Ginebra, M. (2012). Polymeric additives to enhance the functional properties of calcium phosphate cements. *J. Tissue Eng.,* pp. 1–20. doi:10.1177/2041731412439555

Pham, C.B., Leong, K.F., Lim, T.C., Chian, K.S. (2008). Rapid freeze prototyping technique in bio-plotters for tissue scaffold fabrication. *Rapid Prototyp. J.,* 14, pp. 246–253. doi:10.1108/13552540810896193

Porter, M.M., McKittrick, J., Meyers, M.A. (2013). Biomimetic Materials by Freeze Casting, *JOM,* 65, pp. 720–727. doi:10.1007/s11837-013-0606-3

Puppi, D., Chiellini, F., Piras, A.M., Chiellini, E. (2010). Polymeric materials for bone and cartilage repair. *Prog. Polym. Sci.*, 35, pp. 403–440. doi:10.1016/j.progpolymsci.2010.01.006

Qian, B., Shen, Z. (2013). Laser sintering of ceramics. *J. Asian Ceram. Soc.,* 1, pp. 315–321. doi:10.1016/j.jascer.2013.08.004

Qiu, X., Hu, S. (2013). "Smart" Materials Based on Cellulose: A Review of the Preparations, Properties, and Applications. *Materials (Basel),* 6, pp. 738–781. doi:10.3390/ma6030738

Rahaman, M.N., Day, D.E., Bal, B.S., Fu, Q., Jung, S.B., Bonewald, L.F., Tomsia, A.P. (2011). Bioactive glass in tissue engineering. *Acta Biomater.,* 7, pp. 2355–2373. doi:10.1016/j.actbio.2011.03.016

Rezwan, K., Chen, Q.Z., Blaker, J.J., Roberto, A. (2006). Biodegradable and bioactive porous polymer / inorganic composite scaffolds for bone tissue engineering. *Biomaterials,* 27, pp. 3413–3431. doi:10.1016/j.biomaterials.2006.01.039

Rho, J. (1998). Mechanical properties and the hierarchical structure of bone. *Med. Eng. Phys.,* 20, pp. 92–102.

Ritchie, R.O., Buehler, M.J., Hansma, P. (2009). Plasticity and toughness in bone. *Phys. Today,* 62, pp. 41-47.

Rudman, K.E., Aspden, R.M., Meakin, J.R. (2006). Compression or tension? The stress distribution in the proximal femur. *Biomed. Eng. Online,* 5, pp. 12. doi:10.1186/1475-925X-5-12

Ruff, C., Holt, B., Trinkaus, E. (2006). Who's Afraid of the Big Bad Wolff ?: "Wolff's Law" and Bone Functional Adaptation. *Am. J. Phys. Anthropol.,* 129, pp. 484–498. doi:10.1002/ajpa

Schlordt, T., Schwanke, S., Keppner, F., Fey, T., Travitzky, N., Greil, P. (2013). Robocasting of alumina hollow filament lattice structures. *J. Eur. Ceram. Soc.,* 33, pp. 3243–3248. doi:10.1016/j.jeurceramsoc.2013.06.001

Scholz, M.-S., Blanchfield, J.P., Bloom, L.D., Coburn, B.H., Elkington, M., Fuller, J.D., Gilbert, M.E., Muflahi, S.A., Pernice, M.F., Rae, S.I., Trevarthen, J.A., White, S.C., Weaver, P.M., Bond, I.P. (2011). The use of composite materials in modern orthopaedic medicine and prosthetic devices: A review. *Compos. Sci. Technol.,* 71, pp. 1791–1803. doi:10.1016/j.compscitech.2011.08.017

Schramm, G. (1994). *A Practical Approach to Rheology and Rheometry*, 2nd ed, Gebrueder HAAKE GmbH, Karlsruhe.

Singh, M., Kasper, F.K., Mikos, A.G. (2008). Tissue Engineering Scaffolds, *Biomaterials Science: An Introduction to Materials in Medicine*. Elsevier, pp. 1138–1159. doi:10.1016/B978-0-08-087780-8.00110-8

Smay, J.E., Lewis, J.A., Stuecker, J., Cesarano, J. (2006). Direct Ink Writing of Three-Dimensional Ceramic Structures, *Journal of the American Ceramic Society,* 89, pp. 3599–3609. doi:10.1111/j.1551-2916.2006.01382.x

Song, K.W., Kuk, H.Y., Chang, G.S. (2006). Rheology of concentrated xanthan gum solutions: Oscillatory shear flow behavior. *Korea Aust. Rheol. J.,* 18, pp. 67–81. doi:10.1007/BF02908257

Sun, F., Zhou, H., Lee, J. (2011). Various preparation methods of highly porous hydroxyapatite/polymer nanoscale biocomposites for bone regeneration. *Acta Biomater.,* 7, pp. 3813–3828. doi:10.1016/j.actbio.2011.07.002

Suwanprateeb, J. (2012). Influence of printing parameters on the transformation efficiency of 3D-printed plaster of paris to hydroxyapatite and its properties. *Rapid Prototyp. J.,* 18, pp. 490–499. doi:10.1108/13552541211272036

Taboas, J.M., Maddox, R.D., Krebsbach, P.H., Hollister, S.J. (2003). Indirect solid free form fabrication of local and global porous, biomimetic and composite 3D polymer-ceramic scaffolds. *Biomaterials,* 24, pp. 181–94.

Tampieri, A., Sprio, S., Sandri, M., Valentini, F. (2011). Mimicking natural bio-mineralization processes: a new tool for osteochondral scaffold development. *Trends Biotechnol.,* 29, pp. 526–35. doi:10.1016/j.tibtech.2011.04.011

Thavornyutikarn, B., Chantarapanich, N., Sitthiseripratip, K., Thouas, G. A., Chen, Q. (2014). Bone tissue engineering scaffolding: computer-aided scaffolding techniques. *Prog. Biomater.,* 3, pp. 61–102. doi:10.1007/s40204-014-0026-7

Thompson, D.W. (1945). *On growth and form*. Cambridge University Press, Cambridge -The Macmillan Company, New York

Travitzky, N., Bonet, A., Dermeik, B., Fey, T., Filbert-Demut, I., Schlier, L., Schlordt, T., Greil, P. (2014). Additive manufacturing of ceramic-based materials. *Adv. Eng. Mater.,* 16, pp. 729–754. doi:10.1002/adem.201400097

Tsapis, N., Dufresne, E.R., Sinha, S.S., Riera, C.S., Hutchinson, J.W., Mahadevan, L., Weitz, D.A. (2005). Onset of buckling in drying droplets of colloidal suspensions. *Phys. Rev. Lett.,* 94, pp. 1–4. doi:10.1103/PhysRevLett.94.018302

Vallet-Regí, M., Colilla, M., González, B. (2011). Medical applications of organic-inorganic hybrid materials within the field of silica-based bioceramics. *Chem. Soc. Rev.,* 40, pp. 596–607. doi:10.1039/c0cs00025f

Van Der Linden, J.C., Birkenhäger-Frenkel, D.H., Verhaar, J.A, Weinans, H. (2001). Trabecular bone's mechanical properties are affected by its non-uniform mineral distribution. *J. Biomech.,* 34, pp. 1573–1580.

Vilbrandt, T., Malone, E., Lipson, H., Pasko, A. (2008). Universal Desktop Fabrication, *Heterogeneous Objects Modelling and Applications, Lecture Notes in Computer Science.* Springer Berlin Heidelberg, Berlin, Heidelberg, pp. 259–284. doi:10.1007/978-3-540-68443-5

Wang, L., Liu, B., Yang, Q., Lu, D. (2014). Rheological studies of mixed printing pastes from sodium alginate and modified xanthan and their application in the reactive printing of cotton. *Color. Technol.,* 130, pp. 273–279. doi:10.1111/cote.12089

Wang, L., Zhu, F., Lu, D. (2013). Rheological properties of sodium alginate and xanthan pastes on cotton with reactive dye in screen printing. *Text. Res. J.,* 83, pp. 1873–1884. doi:10.1177/0040517513481873

Wegst, U.G.K., Bai, H., Saiz, E., Tomsia, A.P., Ritchie, R.O., Ortiz, C., Boyce, M., Wegst, U.G.K., Bai, H., Saiz, E., Tomsia, A.P., Ritchie, R.O. (2014). Bioinspired structural materials. *Nat. Mater.,* 14, pp. 23–36. doi:10.1038/nmat4089

Wegst, U.G.K., Schecter, M., Donius, A.E., Hunger, P.M. (2010). Biomaterials by freeze casting. *Philos. Trans. A. Math. Phys. Eng. Sci.,* 368, pp. 2099–2121. doi:10.1098/rsta.2010.0014

Wei, G., Jin, Q., Giannobile, W. V., Ma, P.X. (2007). The enhancement of osteogenesis by nano-fibrous scaffolds incorporating rhBMP-7 nanospheres. *Biomaterials*, 28, pp. 2087–2096. doi:10.1016/j.biomaterials.2006.12.028

Weiner, S., Traub, W. (1992). Bone Structure: From Angstroms to microns. *FASEB J.,* 6, pp. 879–885.

Willie, B.M., Petersen, A., Schmidt-Bleek, K., Cipitria, A., Mehta, M., Strube, P., Lienau, J., Wildemann, B., Fratzl, P., Duda, G. (2010). Designing biomimetic scaffolds for bone regeneration: why aim for a copy of mature tissue properties if nature uses a different approach? *Soft Matter,* 6, pp. 4976–4987. doi:10.1039/c0sm00262c

Woodruff, M.A., Hutmacher, D.W. (2010). The return of a forgotten polymer— Polycaprolactone in the 21st century. *Prog. Polym. Sci.,* 35, pp. 1217–1256. doi:10.1016/j.progpolymsci.2010.04.002

Wu, C., Luo, Y., Cuniberti, G., Xiao, Y., Gelinsky, M. (2011). Three-dimensional printing of hierarchical and tough mesoporous bioactive glass scaffolds with a controllable pore architecture , excellent mechanical strength and mineralization ability. *Acta Biomater.,* 7, pp. 2644–2650. doi:10.1016/j.actbio.2011.03.009

Xiong, Z., Yan, Y., Wang, S., Zhang, R., Zhang, C. (2002). Fabrication of porous scaffolds for bone tissue engineering via low-temperature deposition. *Scr. Mater.,* 46, pp. 771–776. doi:10.1016/S1359-6462(02)00071-4

Yeatts, A.B., Fisher, J.P. (2011). Bone tissue engineering bioreactors: dynamic culture and the influence of shear stress. *Bone,* 48, pp. 171–81. doi:10.1016/j.bone.2010.09.138

Yu, X., Xu, M., Xu, S., Su, Q. (2013). Clinical outcomes of giant cell tumor of bone treated with bone cement filling and internal fixation, and oral bisphosphonates. *Oncol. Lett.,* 5, pp. 447–451. doi:10.3892/ol.2012.1036

Zhang, X., Jiang, X.N., Sun, C. (1999). Micro-stereolithography of polymeric and ceramic microstructures. *Sensors Actuators*, 77, pp. 149–156. doi:10.1016/S0924-4247(99)00189-2

Zhang, Y., Zhou, K., Bao, Y., Zhang, D. (2013). Effects of rheological properties on ice-templated porous hydroxyapatite ceramics. *Mater. Sci. Eng. C*, 33, pp. 340–346. doi:10.1016/j.msec.2012.08.048

Zheng, X.Y., Lee, H., Weisgraber, T.H., Shusteff, M., DeOtte, J., Duoss, E.B., Kuntz, J.D., Biener, M.M., Ge, Q., Jackson, J.A., Kucheyev, S.O., Fang, N.X., Spadaccini, C.M. (2014). Ultralight, Ultrastiff Mechanical Metamaterials. *Science,* 344, pp. 1373–1377. doi:10.1126/science.1252291

Zhu, C., Smay, J.E. (2010). Rheology and Flow Behavior of Concentrated Colloidal Gels for Direct-Write Assembly of 3D Mesoscale Structures, *International Solid Freeform Fabrication Symposium*. University of Texas, Austin, pp. 634 – 645.